IMPROVED SITE-SPECIFIC MILLIMETER-WAVE CHANNEL MODELING AND SIMULATION FOR SUBURBAN AND RURAL ENVIRONMENTS

by

Yaguang Zhang

A Dissertation

Submitted to the Faculty of Purdue University

In Partial Fulfillment of the Requirements for the degree of

Doctor of Philosophy

School of Electrical and Computer Engineering

West Lafayette, Indiana

August 2021

THE PURDUE UNIVERSITY GRADUATE SCHOOL
STATEMENT OF COMMITTEE APPROVAL

Dr. James V. Krogmeier, Chair

School of Electrical and Computer Engineering, Purdue University

Dr. Christopher R. Anderson

Department of Electrical Engineering, United States Naval Academy

Dr. Nicolò Michelusi

School of Electrical and Computer Engineering, Purdue University

Dr. David J. Love

School of Electrical and Computer Engineering, Purdue University

Dr. Dennis R. Buckmaster

Department of Agricultural and Biological Engineering, Purdue University

Approved by:

Dr. Dimitrios Peroulis

This dissertation is dedicated to my parents.

I would never have gone this far

without their endless love, support, and encouragement.

ACKNOWLEDGMENTS

This journey has turned out to be a quite long one, but I am extremely grateful that both my family and my academic committee are willing to indulge me to take this slow pace. Thanks to their full support throughout the whole journey, my "Ph.D. grind" feels way less grinding and more like a mix of package tours and self-guided ones: there are milestones required to be accomplished in limited time, but more often than not, enough leisure is kindly granted to me for fully appreciating the views along the road. Particularly, I am not able to find the words that are strong enough to express my gratitude to my parents for their unconditional love and support. The years they have to spend without the company of their only son highlights yet another debt I owe to them which can never be repaid—one that I may not be able to fully comprehend until I become a parent myself.

I would like to express my deepest appreciation to my mentor Professor James Krogmeier. Without his kind support and patient guidance, I would not have been able to gain experience in different projects covering telecommunications, intelligent transportation systems, and digital agriculture, to explore all the fields I am interested in. Besides, I am especially grateful to my mentor Professor Christopher Anderson from the United States Naval Academy. His insights and continuous guidance built the foundation of this thesis.

It is fortunate for me to have a hard-working, open-minded, and responsive academic committee with advisors from different backgrounds, especially because I am striving to become a professor and mentor myself. Professor Krogmeier and Professor Anderson are always willing to think in their mentees' shoes and patiently assist with the students' growth. Professor Nicolò Michelusi and Professor David Love, by contrast, excel at motivating their students in an outcome-oriented approach. And Professor Dennis Buckmaster is a master at creating a positive mentoring environment that is welcoming and supportive to his students. Purdue also provides me with abundant resources and numerous opportunities to cooperate with other brilliant researchers out of my committee. Professor Darcy Bullock from Civil Engineering and Senior Researcher Aaron Ault from the Open Agricultural Technology and Systems Center have impressed and influenced me with their endless energy in pushing ideas into reality. And Professor Mark Bell's passionate teaching style and big smile are still what

I would love to master in the future. The great examples these researchers set have helped me clarify the path I would like to take and I am sincerely thankful for that.

Also, many thanks to my friends and colleagues at Purdue—especially to Alex Layton, Peng Cheng, Dr. Qinfeng Li, Dr. Xun Zhao, Dr. Dayi Lai, Dr. Tomohiro Arakawa, Yang Wang, Dr. Damola Oluwatimi, Sneha Jha, Fabio Andres Castiblanco Rubio, Samuel Noel, Matthew Rogers, Andrew Balmos, Dr. Joon Young Kim, Vinayak Suresh, Dr. Servio Ernesto Palacios Interiano, and Dr. Ngango Yvon Rugema—you are among the main reasons why my Ph.D. journey has been an enjoyable one. And special thanks to my amazing host family, the Wilsons, and generous Mr. and Ms. Ransom, for helping me settle down in the beautiful town of West Lafayette at the start of the journey.

Last but not least, I acknowledge the National Science Foundation (NSF) and the Foundation for Food and Agricultural Research (FFAR) for their financial support during this research[1].

[1] ↑The work in this dissertation was supported in part by the Foundation for Food and Agriculture Research under Award 534662 and by the National Science Foundation under Grants EEC1941529, CNS1642982, CNS1731658, and CCF1816013.

TABLE OF CONTENTS

LIST OF TABLES

LIST OF FIGURES

ABBREVIATIONS

2D	two-dimensional
3D	three-dimensional
ABG	alpha-beta-gamma
AF	attenuation factor
CDF	cumulative distribution function
CI	close-in
DC	direct current
eHata	extended Hata
FSPL	free-space propagation loss
G2A	ground-to-air
HPBW	half-power beamwidth
IF	intermediate frequency
ITU	International Telecommunication Union
KED	knife-edge diffraction
LOS	line-of-sight
LO	local oscillator
LPF	low pass filter
LTE	Long-Term Evolution
M2M	machine-to-machine
Mcps	megachips per second
MIMO	multiple-input and multiple-output
mmWave	millimeter wave
NIST	National Institute of Standards and Technology
NLOS	non-line-of-sight
NTIA	National Telecommunications and Information Administration
PDP	power delay profile
PN	pseudo-random noise
PSD	power spectrum density

RF	radio frequency
RMSE	root mean square error
RX	receiver
SIMO	single-input and multiple-output
SNR	signal-to-noise ratio
TX	transmitter
UAV	unmanned aerial vehicle
USGS	United States Geographic Survey
USNA	United States Naval Academy
USRP	Universal Software Radio Peripheral
UTM	Universal Transverse Mercator
V2V	vehicle-to-vehicle
WHIN	Wabash Heartland Innovation Network
WLAN	wireless local area network

ABSTRACT

Millimeter-wave (mmWave) bands have become the most promising candidate for enlarging the usable radio spectrum in future wireless networks such as 5G. Since frequent and location-specific blockages are expected for mmWaves, the challenge is understanding the propagation characteristics of mmWave signals and accordingly predicting the channel state information. This research direction has garnered great attention worldwide from industry, academia, and government. However, the majority of current research on mmWave communications has focused on urban areas with high population densities, with very few measurement campaigns in suburban and rural environments. These environments are extremely important for future wireless applications in areas including residential welfare, digital agriculture, and transportation. To fill in this research gap, we developed broadband mmWave channel sounding systems and carried out intensive measurement campaigns at 28 GHz, covering clear line-of-sight as well as non-line-of-sight scenarios over buildings and foliage clutters, to fully characterize the mmWave propagation in suburban and rural environments.

Moreover, the accuracy provided by traditional statistical models is insufficient for next-generation wireless networks with higher-frequency carriers, because they are unable to predict abrupt channel changes caused by site-specific blockages. To overcome this issue, we explored the possibility of utilizing site-specific geographic features such as buildings and trees in improving mmWave propagation models. A new channel modeling methodology highlighting site-specific parameter evaluation based on easily obtainable data sources (e.g., LiDAR) was proposed for accurate, fast, and automated channel state predictions. Accordingly, an overall root mean square error (RMSE) improvement of 11.79 dB was achieved in a one-building blockage scenario and a regional RMSE improvement of over 20 dB was observed in a coniferous forest. This approach also enables channel simulations for large-scale system performance evaluation, demonstrating a powerful and promising approach for planning and tuning future wide-area wireless networks. The simulation results showed that network densification alone is not enough for closing the digital gap, especially with mmWaves because of the impractical number of required towers. They also backed up supplementary solutions including private data relays, e.g., via drones and portable towers.

1. INTRODUCTION

Some materials presented in this chapter on the digital gap are from: Y. Zhang, D. J. Love, J. V. Krogmeier, *et al.*, "Challenges and opportunities of future rural wireless communications," *IEEE Communications Magazine*, Dec. 2021, to be published. © 2021 IEEE.

1.1 Motivation

Wireless communications have completely revolutionized society during the past few decades. Considering cellular communications as an example, from analog voice calls in 1G, messaging in 2G, limited data in 3G, and broadband access in 4G, our society's functions have fundamentally changed repeatedly due to new generations of mobile communication technologies. The ever-improving mobile services experienced by the users are fueling a rocketing future demand on broader connections with higher data rates. By 2022, mobile devices will account for 20% of total IP traffic: a seven-fold increase of the global mobile data traffic and over a three-fold increase of the mobile network connection speeds are expected between 2017 and 2022 [2]. Previously available radio resources are insufficient to realize this aggressive expansion.

Millimeter-wave (mmWave) bands have become the most promising candidate for enlarging the usable spectrum in future wireless networks such as 5G [3]–[5] . Once fully exploited, a large amount of underutilized mmWave resources could dramatically increase the communication speed and the network capacity [6]–[8]. This promise has motivated a series of research efforts in channel measurement and modeling for mmWave during the past decade [3], [4], [9]. However, future mmWave systems will mainly benefit urban regions, especially during the initial implementation, due to the high user density, small cell radii (typically 100–200 m), and lower mobility [4]. As a result, the majority of current mmWave channel measurement and modeling research is focusing on urban regions with high population densities [10]–[24], with very limited measurement campaigns carried out for suburban and rural environments [25], [26].

This unbalanced research effort also follows the unbalanced telecommunication resource allocation between urban and rural regions. Even though broadband access today is key to ensuring robust economic development and improving quality of life, the communication infrastructure deployed in rural areas throughout the world lags behind its urban counterparts due to low population density and economic concerns. For the vast majority of broadband users living in urban environments, it can be difficult to understand this imbalance, because network operators prioritize urban tower density over ubiquitous geographic coverage.

Considering the network of a U.S. cellular carrier as an example (Figure 1.1), large cities typically have a high cell tower density, e.g., over $30\,/\,(1000\,\mathrm{km}^2)$ in and around Indianapolis and over $80\,/\,(1000\,\mathrm{km}^2)$ near Chicago. Some urban areas even have tower densities far exceeding these numbers. Approximately 20 km away from downtown Chicago, suburban users enjoy as many as $165\,/\,(1000\,\mathrm{km}^2)$ towers per thousand km^2. In sharp contrast, 44.5% of Indiana's land has less than $5\,/\,(1000\,\mathrm{km}^2)$, while 70.5% has less than 10. It is worth noting that the geographic cell tower density in Figure 1.1b was evaluated within a 50-km radius. Decreasing this radius would yield a map showing a larger digital gap.

These disparities are unnoticed by most urban and suburban users. Figure 1.1a shows that cell towers cluster not only in cities and towns but also along highways. Therefore, even when traveling, most users lack an accurate understanding of broadband inequality. The National Association of Counties tested the Internet speeds of 3069 U.S. counties and found that over 65 percent were experiencing Internet speeds below the Federal Communications Commission (FCC) broadband definition (25 Mbps download, 3 Mbps upload) [28].

The 1G and 2G cellular eras had the simple objective of providing voice connectivity. Consequently, infrastructure construction based on population density (with large macrocells in rural areas) was an efficient, cost-effective approach. In the U.S., rural regions account for 97% of the land area but only 19.3% of the population [29]. Achieving broadband connectivity over such a large geographic area requires a high initial investment, as more towers are needed for broadband versus voice service. For instance, the average cost for constructing one conventional cellular site is estimated to be \$200,000–\$250,000, which is

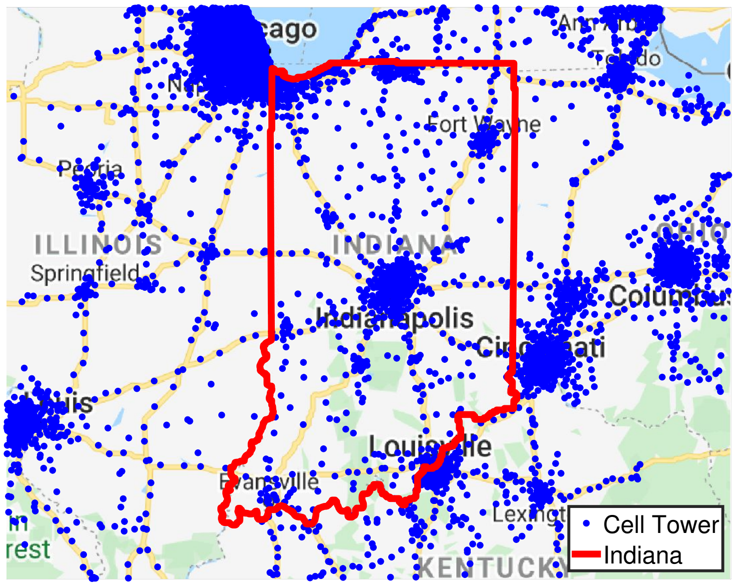

(a) Cell tower locations

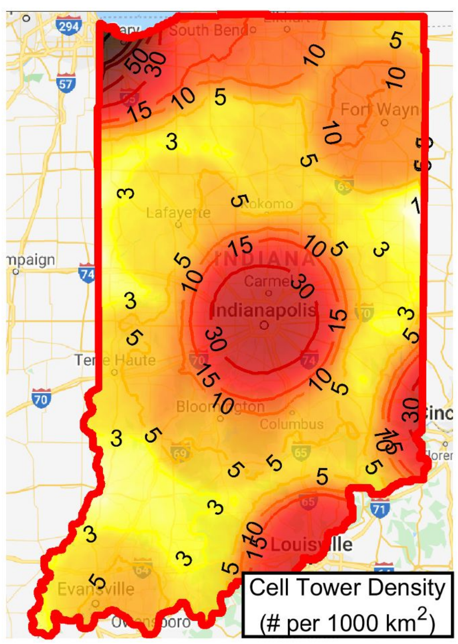

(b) Indiana cell tower density

Figure 1.1. Tower distribution of a national cellular carrier according to a randomized real network laydown from the National Telecommunications and Information Administration [27]. Map data © 2021 Google.

hard to recover from a low density of potential rural users [30]. This fundamental revenue problem is arguably the primary culprit for the digital divide.

In 5G and future standard deployments, there will be an increasing demand for the connection of physical objects [2], [31]. Cisco is anticipating 29.3 billion devices connected to IP networks (more than three times the global population) by the year 2023, which boasts a 50% increase compared with what we had in 2018 [32]. Furthermore, around half of these connections will be machine-to-machine (M2M) [32]. With the shift from connecting people to connecting things, new applications in a variety of areas will require rural broadband to sustain the economy. According to the U.S. Department of Agriculture, digital agriculture could drive an annual additional gross benefit of US$47–65 billion, corresponding to nearly 18% of annual agricultural production in 2017, and rural broadband connectivity could contribute over one-third of this value (i.e., US$18–23 billion) [33]. The U.S. Department of Transportation [34] has pointed out that: 49% of U.S. car crash fatalities in 2015 occurred in rural regions, despite the low population; wireless connectivity could reduce these fatalities by 80%. The digital divide prevents such visions from being realized. Furthermore, broadband access has become a necessity instead of a luxury, especially during and after the COVID-19 pandemic. The digital divide is causing inequality in multiple dimensions, which could economically and socially cripple rural communities [35].

Future mmWave communications will play a key role in bridging the digital gap by providing cost-effective high-throughput wireless backhaul solutions [36]–[39]. Traditionally, optical fiber is the technology of choice for most Internet service providers and wireless communications carriers. It supports secure long-distance communication with high speed and low latency, but the deployment remains relatively expensive. The abundant spectrum resource available in the mmWave range opens the possibility of supporting backhaul traffic with point-to-point/point-to-multipoint multi-hop fixed wireless technologies. What is more, the promises of future wireless networks, such as extremely high throughput and ultra-low latency, depend heavily on mmWave and the features enabled by it, including small antenna form factor, massive multiple-input multiple-output beamforming, and spatial multiplexing [40]–[42]. More attention is needed on the characterization and application of mmWave signal propagation in suburban and rural environments. Otherwise, mmWaves will benefit mainly the urban users and the digital gap will be further widened.

Accurately modeling mmWave channels is very important for future network planning and deployment in suburban and rural environments, especially because the higher attenuation suffered by mmWave signals already significantly hinders their coverage ability [43]. Signals at mmWave bands are prone to destructive effects caused by obstacles such as buildings and trees, which is not well captured in traditional channel models for lower-frequency bands [44]–[46]. The successful utilization of mmWave bands in wireless wide-area networks remains challenging. In urban regions, cellular network densification has been proposed to compensate for the propagation issues [36], [47], [48]. This is backed by the high user density and considerable profit. In rural areas, though, densification is not an economically viable solution anymore in the foreseeable future. Channel models for mmWave signal propagation will need to consider local blockages to increase their accuracy for cost-efficient network deployment.

1.2 Structure Overview of the Dissertation

mmWave has now become a game-changer for wireless communications. However, based on our research, the digital divide between urban and rural regions is more severe than expected. Without proper intervention, it will grow bigger because of the broader application of mmWaves. To facilitate the use of mmWaves in suburban and rural regions, we conducted two intensive measurement campaigns. Chapter 2 introduces the measurement system and our first measurement campaign in typical suburban environments at the United States Naval Academy (USNA). mmWave's extremely high sensitivity to local blockages was observed and accordingly, a one-building blockage channel model considering the geometry of building walls for better accuracy is proposed in Chapter 3. Then, our second measurement campaign at the National Institute of Standards and Technology (NIST) for a more complicated case, a coniferous forest with hundreds of trees, will be introduced in Chapter 4. The site-specific channel modeling idea was also applied there to achieve better performance than traditional statistical channel models.

The site-specific models perform better than traditional ones thanks to the site-specific features. They are easy to implement and fully automatable. And the computational cost is very low due to their simple structures. Furthermore, these features fit the requirements of large-scale channel simulations. Chapter 5 applies the techniques of site-specific channel modeling into large-scale channel simulation. Simulations for ten counties in Indiana were carried out to quantitatively analyze the coverage improvement for rural users via data relay drones. In Chapter 6, the simulator will be extended to cover a majority area of the State of Indiana for simulations at a wide range of different carrier frequencies. It was observed that network densification alone is not a good enough solution to bridging the digital divide. Without more research efforts on cost-effective rural coverage, the digital gap would probably be widened by the popularization of mmWaves. The simulator with improved scalability will also help in providing deeper insights into the system-level performance of real-life wireless networks. Finally, Chapter 7 recaps our findings and contributions.

1.3 mmWave's High Sensitivity to Site-Specific Blockages

One of the initial steps in employing new carrier frequency bands is to measure and characterize the corresponding signal propagation through the environments of interest. Then, the measurement results are inspected and developed into easy-to-use closed-form models to predict the signal propagation in locations with no/few measurement references. Good channel models should generalize well beyond the measurement data sets from which they are originated. Consistent high accuracy essentially marks a good understanding of how the signal will behave, which is the foundation for successfully utilizing the new bands. This practice applies to mmWave, too. To promote the application of mmWave in suburban and rural areas, (i) measurements need to be conducted for these environments, (ii) new characteristics of the propagation, if any, need to be identified, and (iii) channel models need to incorporate these new characteristics for more accurate results.

Most of the curses and benefits of mmWave come from its unique signal propagation characteristics. For example, traditional carrier bands in mobile communications are below 6 GHz, while mmWave bands have way higher frequencies than that. On the one hand, the higher frequency range results in a significantly greater attenuation. To counteract this negative influence, narrow-beam directional antennas are typically required for better gains towards the receiver's direction [49]–[51]. On the other hand, the higher frequency enables the design of miniature antennas and the deployment of antenna arrays in a single device [40], [51], [52]. Built on the possibility of fitting several (or even tens of) antennas in a base station or a mobile device, advanced signal processing techniques including beamforming, beam alignment, and (massive) multiple-input and multiple-output (MIMO) could play a vital role in the successful commercial deployment of mmWave communication systems [4], [5], [53]. Furthermore, with the controllable narrow beams from this suite of technologies, spatial multiplexing becomes very appealing in further boosting the capacity of mmWave networks in the future [42], [54], [55]. The benefits from these technologies, are yet to succeed in lowering the risk of the digital divided being enlarged by the popularization of mmWaves, though. The features and requirements of urban environments [4] better fit what these technologies can provide, so early adoptions of mmWave, as well as the aforementioned technologies, are expected to be for urban regions.

Another major propagation disadvantage of mmWave is its high sensitivity to site-specific blockages, as we will learn in Chapters 2 to 4. This topic has been well studied for urban environments [56]–[58] and it has recently received great attention in vehicle-to-vehicle [59]–[61] and ground-to-air [62]–[64] communication systems. Thanks to our custom-designed positioning system, we were able to quantitatively demonstrate mmWave's extremely high sensitivity to site-specific blockages in suburban and rural environments. We will go into more detail on this later in Chapters 2 and 3, but now is a good time for us to examine some results to obtain a better understanding of the disadvantage of ignoring site-specific features in mmWave channel modeling.

As shown by the photos in Figure 1.2, our positioning system can move the RX antenna left and right along the x-axis and up and down along the z-axis. During the measurement campaign, we positioned the RX antenna following a small "+" pattern to investigate how the signal interacts with the site-specific features present between the transmitter and the RX. Figure 1.3 illustrates the corresponding measurement data collected behind a bleacher. It is worth noting that the RX antenna was confined in a very small square area, which has

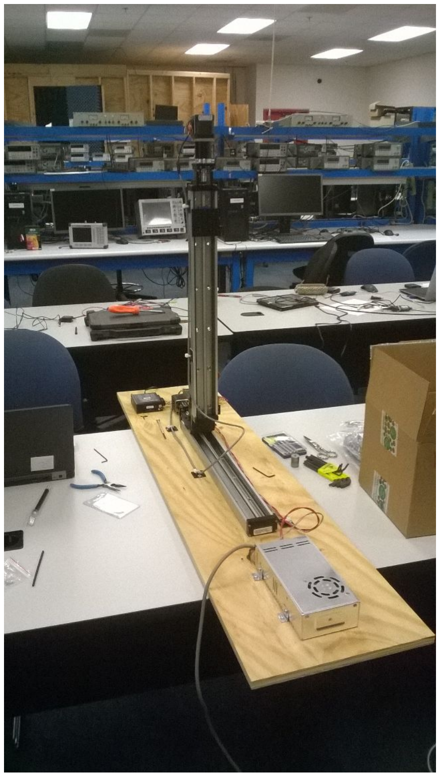

(a) Side view

(b) Back view

Figure 1.2. The custom-designed x-z positioning system at the RX side.

(a) Environment

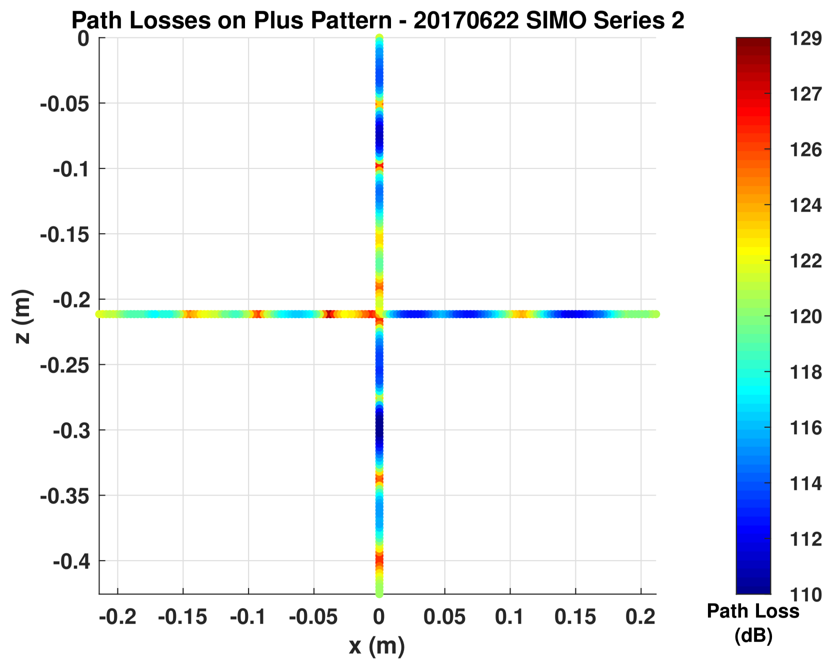

(b) Path loss measurements

Figure 1.3. Illustration of blockage behind a bleacher.

(a) Environment

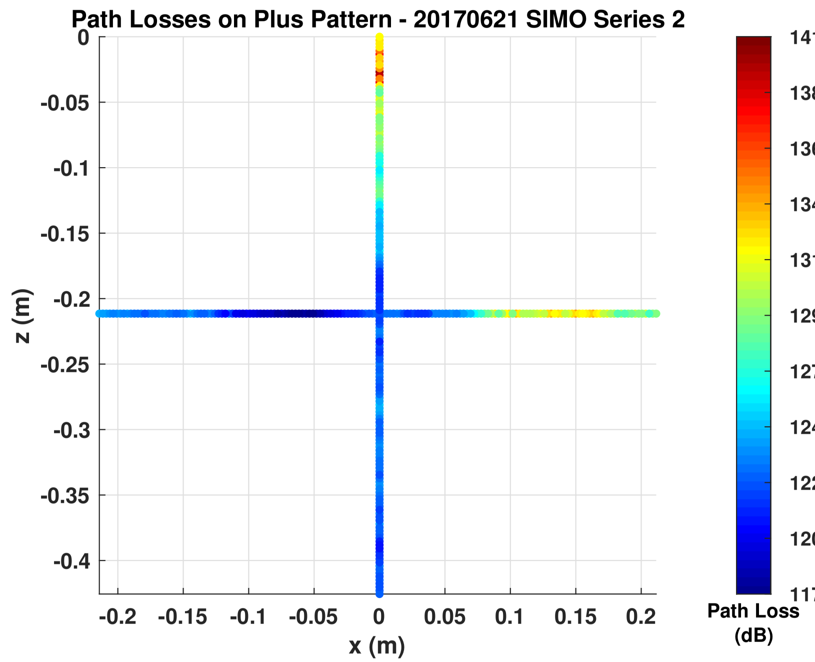

(b) Path loss measurements

Figure 1.4. Illustration of blockage behind a tree.

a side length of less than 0.5 m. However, the path loss difference could be as significant as 19 dB. We can even clearly see the blockage pattern caused by the frames and rails. Of course, this is an extreme case, but similar effects were observed near common obstacles such as buildings and trees, too. For example, path loss results collected behind a tree are shown in Figure 1.4. Again, the RX antenna was limited in a very small area. In this case, when the RX moved too high, or too to the right side, the communication link would be blocked by the tree captured in Figure 1.4a, causing an extra path loss up to 24 dB. Without considering the site-specific geographic information, mmWave models will not be able to predict abrupt centimeter-level changes as demonstrated in the two examples here.

Because of the severer propagation attenuation and the higher sensitivity to local blockages experienced by mmWaves, coverage will be the biggest research challenge in applying mmWave communications in suburban and rural regions. This challenge is as difficult as, if not more demanding than, mmWave network deployments in urban environments. Our contributions to this challenge include (i) two intensive campaigns to better characterize mmWave propagation in suburban and rural areas, (ii) improved accuracy of traditional mmWave channel models with site-specific geographic information, and (iii) increased scalability of mmWave channel simulations for large-scale network performance evaluation. The improved channel models can facilitate the deployment of mmWaves, while the improved channel simulations can give us a deeper understanding of the system-level performance of real-life wireless networks.

1.4 Improving mmWave Channel Models with Site-Specific Features

In this dissertation, site-specific geographic features will be included in mmWave channel modeling to improve model performance. Measurement campaigns at 28 GHz were conducted for both suburban resident and rural forest environments to support the investigation. Broadband sliding correlator sounding systems [65] were used during these campaigns. The extra attention caused by obstacles was carefully analyzed and eventually reflected in our site-specific channel models.

A detailed introduction is given for the channel measurement system in Chapter 2. Measurement results collected on the campus of the United States Naval Academy, which is a typical suburban environment, were inspected. Performance evaluations on the path loss prediction are provided for popular traditional channel models, including the close-in free space reference distance path loss model, the alpha-beta-gamma model [18], and the International Telecommunication Union (ITU) site-general/site-specific model for propagation over rooftops [66]. These traditional models typically take a condensed, statistical approach, which works well so far for carrier frequencies lower than mmWaves. This approach is simple to understand and easy to use. It is also accurate to a reasonable degree, with a typical root mean square error (RMSE) of around 10 dB for the suburban environment and a typical RMSE of around 20 dB for rural forest environment based on our measurement data sets. However, as shown in our measurement results, mmWave is very sensitive to blockages [67]. The consideration of site-special geographic features, e.g., buildings and trees, becomes necessary to ensure a good performance of future mmWave channel models. Otherwise, local obstacles and the corresponding signal destruction can not be fully captured in these models, causing channel condition predictions too off to be useful in real-life scenarios.

Following this idea, new research on mmWaves has been conducted for high-accuracy predictions on channel characteristics via simulations, especially by the means of high-fidelity ray tracing [68]–[72]. A two-dimensional (2D) or full three-dimensional (3D) environment reconstruction is required for each area of interest, typically manually [68], [69], [72] or with the help of high-resolution LiDAR [71]. This approach yields very promising accurate results, but it is difficult to be applied in large-area analyses needed in real-life network constructions. The complexity, especially the intense labor work involved in the environment reconstruction and the high computational expense required by the simulation, has been the main obstacle in a broader application. Currently, the application is mainly limited to small-scale environments, especially indoor [68], [70] and dense urban ones [68], [71].

To harvest the benefits of both worlds, we developed fully automatable low-complexity channel models which make predictions based on easy-to-obtain site-specific geographic information. A good example for this would be our one-building-blockage model introduced in Chapter 3 for suburban residential environments. Based on a simple geometry representation of the building of interest, the model can compute an adjustment term evaluated through the knife-edge diffraction model [73]. Adding this term to the baseline ITU site-general model for propagation over rooftops [66] yielded a significant RMSE improvement.

Chapter 4 extends our investigation to a complicated rural coniferous forest environment. In that work, a variety of traditional models were inspected, including the partition-dependent attenuation factor model [74], the ITU-R obstruction by woodland model [75], and Weissberger's model [76]. Site-specific features, e.g., the foliage depth and the foliage area, were computed from Public LiDAR and ground elevation data from United States Geographic Survey (USGS). Two new site-specific models were developed accordingly to further improve the performance available from the traditional models.

1.5 Large-Scale Coverage Analyses via Site-Specific Channel Modeling

So far, we have been blurring the boundary between channel modeling and simulation to better describe mmWave's sensitivity to blockages in future channel models. On the other hand, the simplicity inherited from the traditional channel modeling philosophy makes it possible for us to apply the site-specific channel modeling concepts into large-scale channel simulation. We will explore this idea in the site-specific cellular coverage analyses presented in Chapters 5 and 6. Chapter 5 will quantitatively evaluate the coverage performance of drone data relays at different heights in an LTE system, while Chapter 6 will conduct state-wide simulations for Indiana with a wide range of carrier frequencies to assess the validity of network densification for rural regions. These analyses are important in quantifying the coverage and locating poorly covered spots in real-life wireless wide-area networks. They also provide us with a deeper understanding of the digital divide in terms of service coverage: network diversification alone is probably not a good enough solution for bridging the digital gap; more research efforts are needed in developing cost-effective supplementary solutions, e.g, private data relay via drones or portable towers.

2. 28-GHZ CHANNEL MEASUREMENTS AND MODELING FOR SUBURBAN ENVIRONMENTS

Reprinted, with permissions, from: Y. Zhang, D. J. Love, N. Michelusi, *et al.*, "28-GHz channel measurements and modeling for suburban environments," Department of Electrical and Computer Engineering, Purdue University, West Lafayette, Indiana, Tech. Rep. TR-ECE-17-07, Nov. 2017. [Online]. Available: https://docs.lib.purdue.edu/ecetr/483/. A majority of the materials were also presented in: Y. Zhang, S. Jyoti, C. R. Anderson, *et al.*, "28-GHz channel measurements and modeling for suburban environments," in *2018 IEEE International Conference on Communications (ICC)*, IEEE, May 2018, pp. 1–6. DOI: 10.1109/icc.2018.8422820.

2.1 Introduction

The increasing demand of mobile device users for higher data rates has been the driving factor for the rapid development of mobile telecommunications during the past decade [3]. The number of worldwide mobile subscriptions, which reached a record height of 7.5 billion in 2016, has continued to increase, and the total mobile data traffic is expected to rise at a compound annual growth rate of 42% between the end of 2016 and 2022 [77]. This increasing usage of wireless technology is prompting mobile service providers to take advantage of higher frequency bands in the foreseeable future, starting with millimeter waves (mmWaves), to overcome the expected global bandwidth shortage [78].

With recent advances in radio frequency (RF) technology [79]–[81], hardware operating at mmWave frequencies is becoming commercially available [4], [82], [83]. This has made mmWave frequencies the most promising higher frequency bands for a larger usable radio spectrum. To fully understand the propagation characteristics of mmWave signals, the amount of research on mmWave channel measurement and modeling has increased dramatically in the past five years [3], [84]–[86]. However, the majority of current research on mmWave communications has focused on urban areas with high population densities, with very few measurement campaigns in suburban and rural environments, which are also important for future mobile networking technologies. Moreover, statistical models for point-to-point links have received significant attention, but the channel information provided by these approaches is insufficient for next-generation wireless networks such as 5G. These networks must address mobility requirements because frequent and location-specific blockages are expected at mmWaves, which require a much richer set of channel state information beyond LoS path loss (such as multipath scattering).

In this paper, we explore this gap in the research by focusing on suburban environments and constructing physically motivated and practical models that can be used for mmWave networks in these environments. An intensive measurement campaign has been carried out at the United States Naval Academy (USNA) in Annapolis, Maryland. Measurements were taken around the campus at 28 GHz to characterize the propagation in a suburban-type environment. The resulting path losses are compared with several standard 5G channel models. Our results indicate that a holistic, network-wide approach beyond traditional point-to-point links may be needed to deal with the high dependence of mmWaves on site-specific environment geometry.

The paper is organized as follows: In Section 2.2, we present our propagation measurements in suburban environments; In Section 2.3, we present the procedure for calculating basic transmission losses, followed by our analysis in Section 2.4; Finally, in Section 2.5, we conclude the paper.

2.2 Mm-Wave Propagation Measurements for Suburban Environments

An outdoor propagation measurement campaign was conducted on the USNA campus to emulate a typical 5G deployment in a suburban environment. Compared with urban environments, the USNA campus has shorter buildings with more flexible shapes and locations, wider streets, and lighter traffic. During the campaign, the transmitter (TX) was temporarily installed on the Mahan Hall clock tower. The receiver (RX) was moved around the campus to obtain path loss measurements for individual sites and continuous paths.

2.2.1 Measurement Equipment

A custom-designed broadband sliding correlator channel sounder [87] was used to record propagation data. Figure 2.1 presents block diagrams for the channel sounder. At both the TX and the RX sides, horn antennas with a nominal +22 dBi gain and 15° half-power beamwidth (HPBW) were employed, and pseudo-random noise (PN) generators produced the same PN sequences with a chip sequence length of 2047 [3].

At the TX, the PN probing signal was generated with a chip rate of 400 megachips per second (Mcps). To make the implementation cost-effective, the signal was first modulated to a 2.5-GHz intermediate frequency (IF) and then converted to RF of 28 GHz by mixing it with a 25.5-GHz local oscillator (LO) at the upconverter. At the RX, the received signal was first downconverted from 28 GHz to 2.5 GHz and then cross-correlated with the identical PN sequence generated with a slightly slower clock rate of 399.94 MHz, similar to the setup in [3]. A Universal Software Radio Peripheral (USRP) B200 was utilized to record the resulting in-phase (I) and quadrature (Q) signal components. It also regularly sampled the RX's location with the help of an onboard GPS disciplined oscillator (TCXO version). The implementation of the TX and RX systems is shown in Figure 2.2. The components are fixed on shelves for portability and the TX is furthermore enclosed into a rack case for extra protection during the deployment.

Table 2.1 summarizes the key parameters for the channel sounder. Note that the estimation for the maximum measurable path loss is based on the following. (1) The RX low-noise amplifier has a noise figure of 2.4 dB, so we assume a worst-case RX noise figure of 6 dB. (2) The RX detection bandwidth is 60 kHz. (3) The minimum signal-to-noise ratio (SNR) for a detectable signal is empirically estimated as 5 dB.

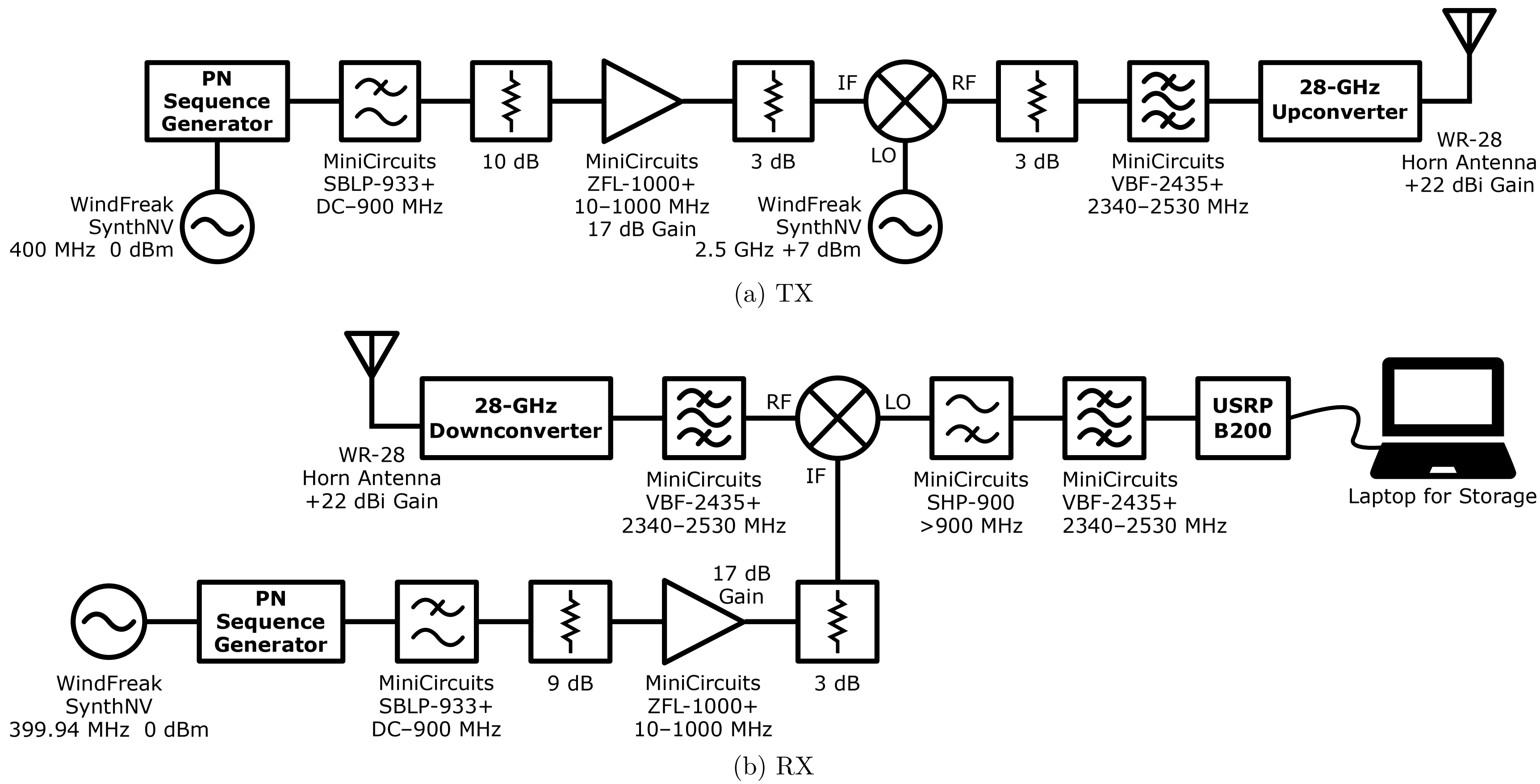

Figure 2.1. Block diagrams for the 28-GHz broadband sliding correlator channel sounder. Model numbers are labeled for some commercially available parts.

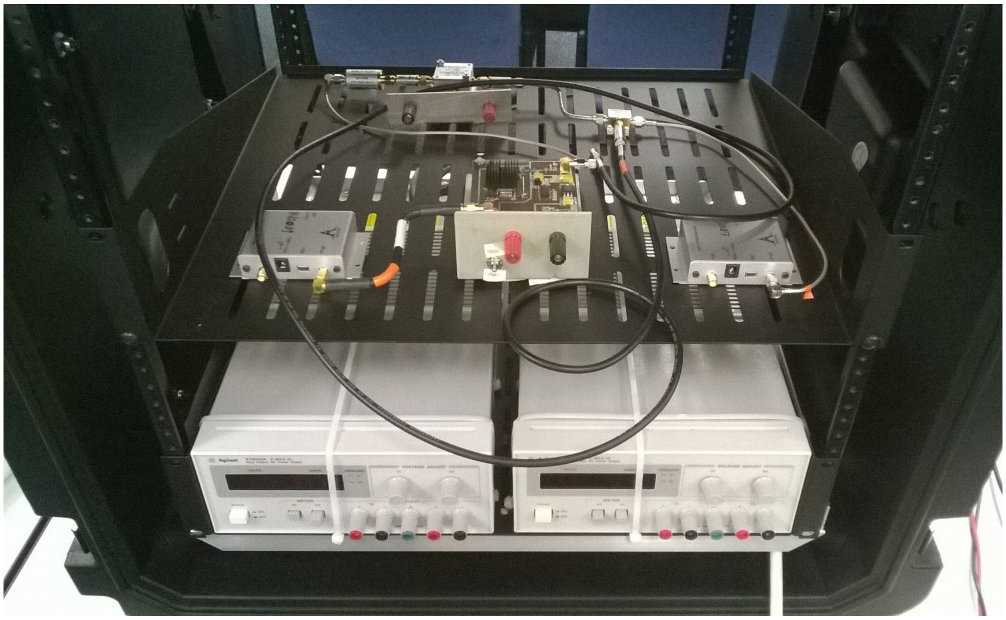

(a) TX

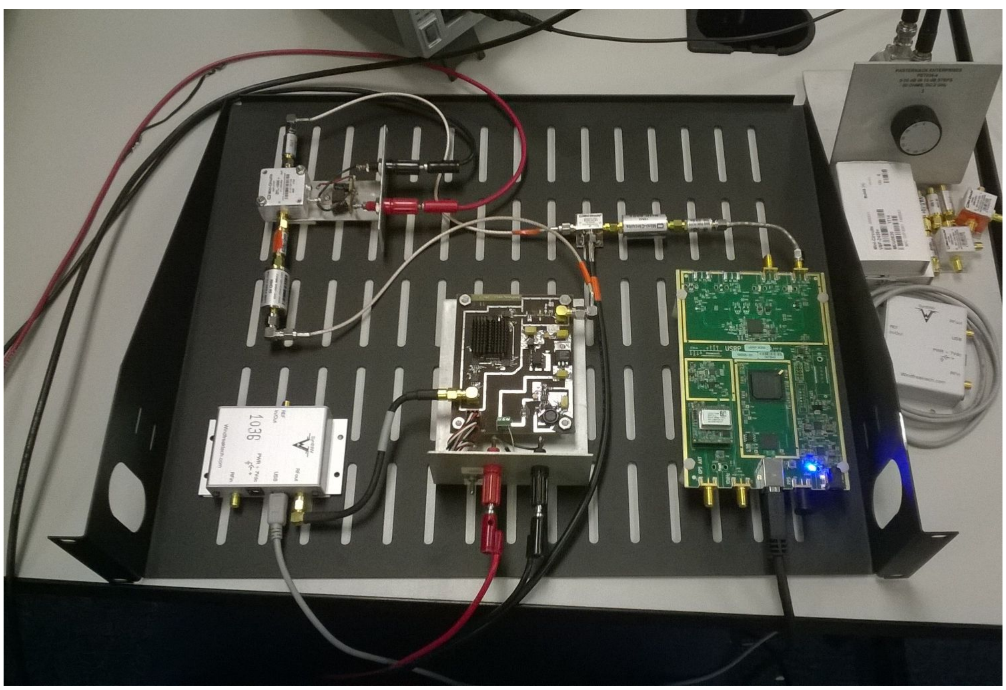

(b) RX

Figure 2.2. Photos of the custom-designed spread-spectrum channel sounder.

Table 2.1. Broadband Sliding Correlator Channel Sounder Specifications

Carrier Frequency	28 GHz
Chip Sequence Length	2047
RF Bandwidth (First Null)	800 MHz
TX Chip Rate	400 Mcps
Temporal Resolution	2.5 ns
RX Chip Rate	399.94 Mcps
TX Power	23 dBm
TX/RX Antenna Gain	22 dBi
Measured TX/RX Azimuth HPBW	10.1°
Measured TX/RX Elevation HPBW	11.5°
Maximum Measurable Path Loss	182 dB

2.2.2 Measurement Setup and Procedure

Three types of measurements have been performed for large-scale path loss, emulated single-input and multiple-output (SIMO), and continuous tracks. The TX was installed at a height of 90 feet (27.4 m) to emulate a microcell deployment. The RX was moved around campus by an electric car or a two-layer platform trolley to obtain the measurements, which is illustrated by the photographs in Figure 2.3. For both cases, the platform for the RX could be rotated horizontally and tilted with composite wood shims to align the beam.

We used compasses and digital levels to achieve beam alignment before the measurements at each RX location. Aside from the USRP output files and GPS samples, the azimuths and elevations of both the TX and RX antennas were recorded manually. This allowed us to reconstruct the geometry relationship of the antennas and extract precise antenna gains during post-processing for path loss computation and analysis. The USRP gain was manually adjusted to maximize the SNR at the RX.[1]

[1]↑The Python code for automatically carrying out the measurements at each location using GNU Radio, together with the MATLAB code for post-processing the collected data, are available at https://github.com/YaguangZhang/EarsMeasurementCampaignCode.git

(a) RX on an electric car

(b) RX on a trolley

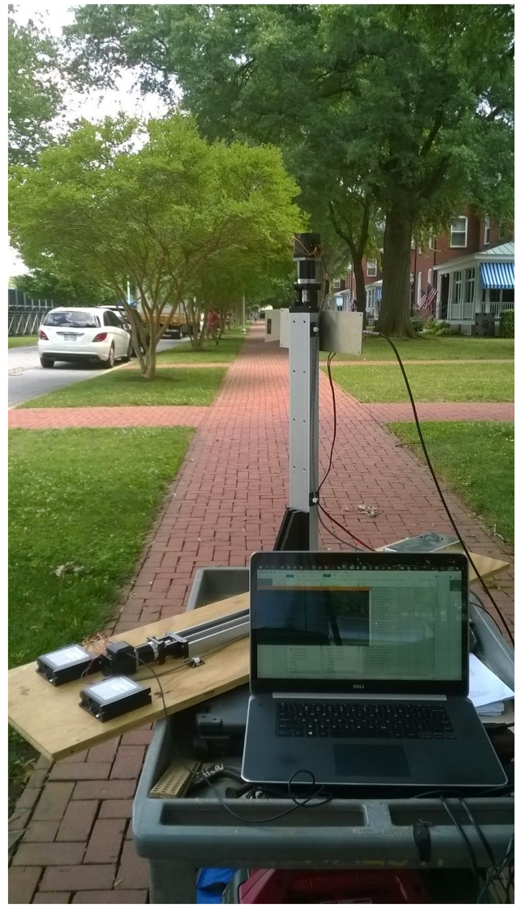

(c) Before a continuous signal recording for a pedestrian path

Figure 2.3. Photos of the measurement setup.

Large-Scale Path Loss Measurements

Forty measurement locations were chosen to investigate the large-scale path loss at various distances from the TX (between 100 m and 1000 m). For each site, the RX antenna was moved along X and Z axes by our positioning system to form a "+" pattern within a $20\lambda \times 20\lambda$ area, where $\lambda = 10.7$ mm was the wavelength corresponding to 28 GHz. For every λ interval on the "+" pattern, one 3-second signal recording and one GPS sampling were obtained, with 40 separate measurements in total. In Figures 2.3b and 2.3c, the custom-built X-Z positioning system is shown.

Emulated SIMO Measurements

Measurements that were used to emulate SIMO signals were similar to those for the large-scale path loss, but with a higher space sample density and a larger sample area for each site. The RX antenna was moved along the "+" pattern with the interval between adjacent measurements reduced to 0.25λ. The pattern covered an enlarged $40\lambda \times 40\lambda$ area, with 320 separate measurements in total for each site. Ten locations were chosen, where the distances between the TX and the RX varied from 50 m to 500 m. The data collected were or will be used to analyze small-scale propagation characteristics. However, in this paper, we focus only on large-scale path loss.

Measurements for Continuous Tracks

To investigate the shadowing effect on a moving user, two approximately 200-m-long straight tracks were chosen for continuous signal recordings. The TX antenna was pointed at the center of the track for each recording. The RX antenna was fixed on the positioning system and moved at walking speed along each track to record the signal, and the GPS location of the RX was sampled once per second. The RX antenna elevation was kept at 0°, and the platform was adjusted as necessary to maintain the azimuth concerning the fixed earth reference during the recording process (see Figure 2.3c) for the beam alignment.

2.3 Basic Transmission Loss Calculation

In this section, we present our procedure for computing the basic transmission loss of each signal recording. Received signal power calculation, RX calibration, antenna pattern generation, and antenna gain extraction were considered in determining antenna-independent path losses.

2.3.1 Received Signal Power Calculation

The traditional method of calculating received signal power for broadband measurements is carried out in the time domain by integrating the total area under a power delay profile (PDP), assuming that all the multipath signals add up in phase. Instead, we adopted a frequency-domain technique, as illustrated in Figure 2.4, to preserve the phase relationships and yield a more accurate estimate of received power. For each measurement, the noise amplitude characteristics were first estimated for the filtered signal to set a noise elimination threshold. Then, all samples weaker than the threshold were set to 0, as shown in Figure 2.4a. The received power energy was computed by integrating the PSD of the noise-eliminated signal below 20 kHz, ignoring the DC component, as shown in Figure 2.4b. This process is summarized below,

1. Run the recorded complex I/Q voltage waveform through a 60 kHz low pass filter (LPF) to remove noise in frequency.

2. Further eliminate noise in the time domain by (a) estimating the standard deviation σ and mean n_0 for the noise using 10%–20% of the samples between two adjacent signal pulses, as illustrated in the top plot of Figure 2.4a; (b) calculating the noise elimination threshold as $3.5\sigma + n_0$; and (c) Setting all samples with an amplitude below the threshold to 0, as illustrated by the plot at the bottom of Figure 2.4a.

3. Calculate the received power by integrating over the power spectrum density (PSD) of the noise-eliminated signal. We chose a tighter integration range (1 Hz–20 kHz) to ignore residual high-frequency noise and direct current (DC) components, as illustrated in Figure 2.4b.

The resulting values would have a linear relationship with the actually received power. Next, we needed the RX calibration to convert the calculated power to the received power.

2.3.2 RX Calibration

To calibrate the RX, the upconverter and downconverter, as well as the antennas, were removed from our system in Figure 2.1. Then, an adjustable attenuator for IF signals with a 5-dB step size was attached to the TX to simulate the channel. The RX together with a spectrum analyzer were used to record and measure the signal strength separately for a set of different attenuation values, with the results from the spectrum analyzer treated as the reference for signal strengths. We repeated the procedure with the RX gain (i.e., the

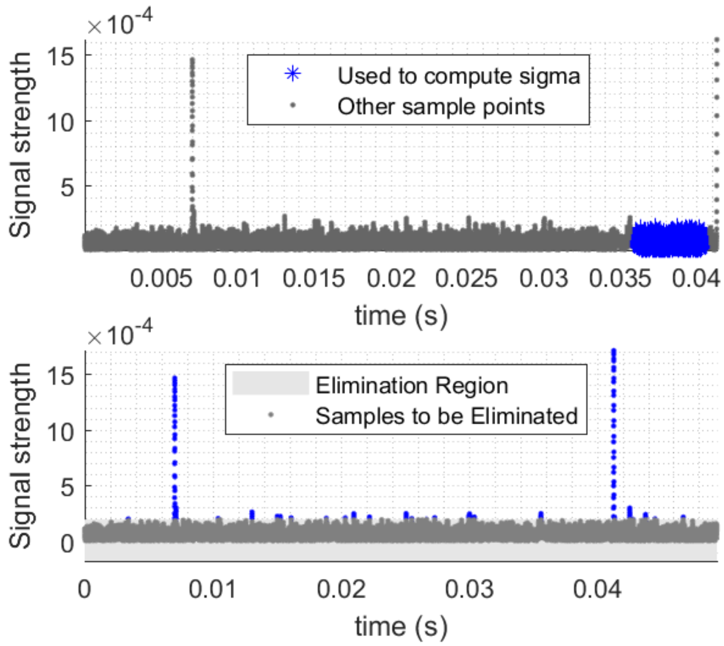

(a) Noise variance estimation and noise elimination

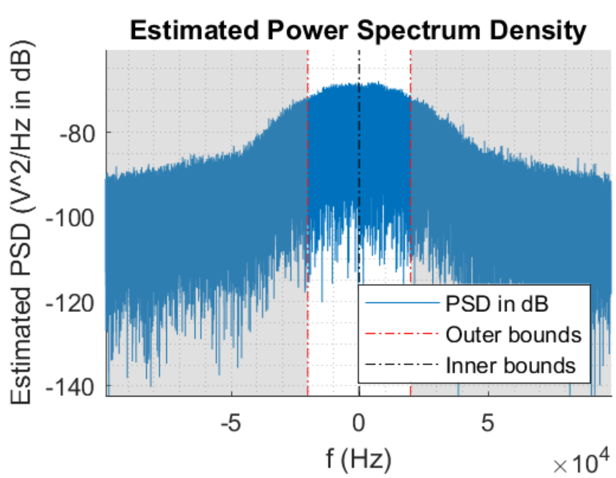

(b) Integral in frequency for the signal power

Figure 2.4. Illustration of the received signal power calculation in the frequency domain.

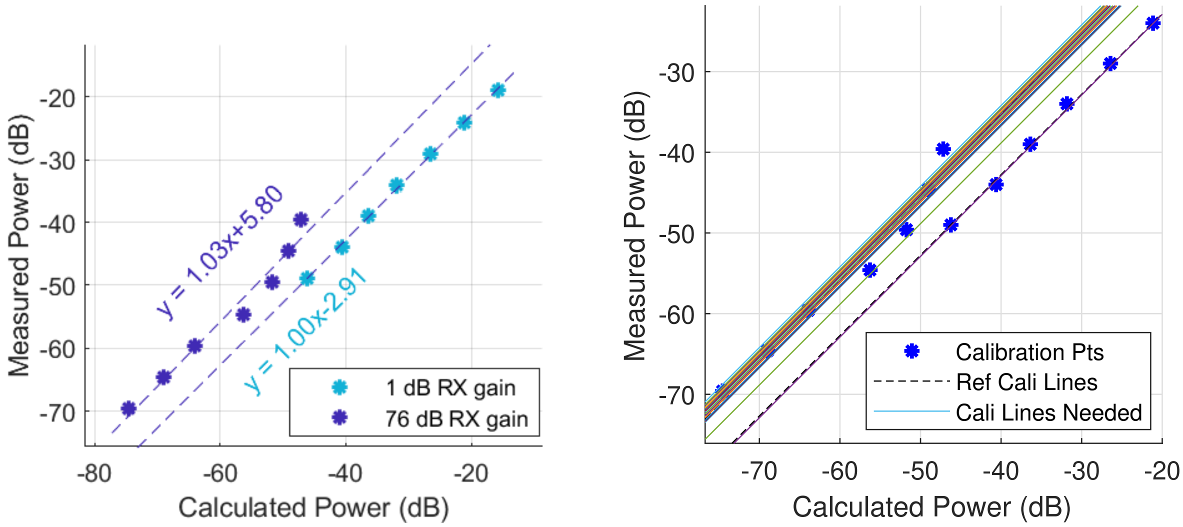

(a) Base calibration lines

(b) Linearly interpolated calibration lines

Figure 2.5. Linear fitting and interpolation for RX calibration lines.

adjustable USRP gain) set as its minimum (1 dB) and maximum (76 dB) values. From the obtained power value pairs, linear relationships were extracted for expected measured power vs. calculated power at the RX gain limits [88]. Figure 2.5 shows the resulting two base reference calibration lines obtained via orthogonal least squares, as well as all the calibration lines needed for our whole dataset gotten via a linear interpolation over the RX gain. By carrying out orthogonal least squares over the calibration data points, we constructed a linear relationship between the calculated power and the reference power measured by the spectrum analyzer, as can be seen in Figure 2.5a. Then, Figure 2.5b illustrates how to obtain new calibration lines for the RX gains used in the campaign. The calibration lines needed for the whole dataset, denoted by the cluster of colored lines in Figure 2.5b, were obtained via a linear interpolation over the RX gain with fixed unit slopes. From these results, received powers were computed accordingly.

2.3.3 Antenna Pattern Generation

Using calibrated measurements from the manufacturer as a reference, we were able to account for upconverter/downconverter and antenna gains.

Normalization for Antenna Plane Patterns

To construct the pattern for our antennas, two measurement sweeps were conducted in an anechoic chamber at USNA for the azimuth and elevation planes, respectively, using an Anritsu VectorStar MS4640 series Vector Network Analyzer and the Diamond Engineering DAMS Antenna Measurement System. The forward transmission coefficients $|S21|$ from each sweep were normalized to the nominal maximum gain of the antennas at 28 GHz, +22 dBi, and the resulting antenna patterns are plotted in Figure 2.6. The antenna beamwidths (10.1° azimuth HPBW and 11.5° elevation HPBW) were computed accordingly.

Full 3D Antenna Pattern Filling

From the azimuth and elevation antenna patterns, we constructed a full 3D pattern for the antenna via linear interpolation, as illustrated in Figure 2.7.

Antenna Gain Computation

With the detailed measurement records collected, we were able to reconstruct the geometry relationship of the TX and RX antennas for each measurement and extract their gains. The Universal Transverse Mercator (UTM) coordinate system (x, y), also known as $(easting, northing)$, was extended with $altitude$ z to form a three-dimensional (3D) reference system (x, y, z). Inside this system, a new 3D coordinate system (X, Y, Z) was constructed originating at the antenna of interest, which could be for either the TX or the RX, so that the azimuth and elevation angles for any destination point could be calculated. The corresponding gain was extracted by interpolating the antenna measurement data in 3D.

Figure 2.8 gives an illustration for computing the TX antenna gain for one measurement. In this example, $westing = -easting$ is used in the visualization. Within the extended UTM coordinate system, the azimuth and elevation angles for the destination, from the TX's point of view, were calculated. Then, the resulting gain for the antenna was extracted via 3D antenna pattern interpolation. For the case illustrated, the antenna of interest was the TX on the clock tower. From the TX antenna's point of view, i.e. in the tilted coordinate system (X, Y, Z) determined by the TX antenna's orientation, the destination has an azimuth

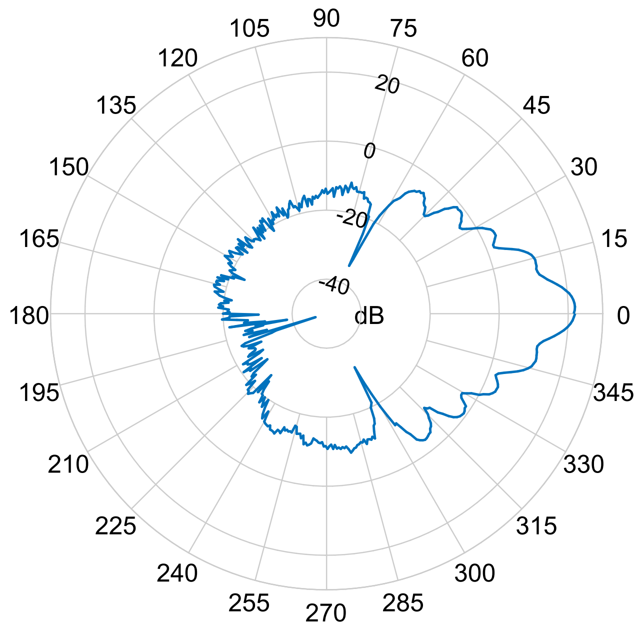

(a) Azimuth plane pattern

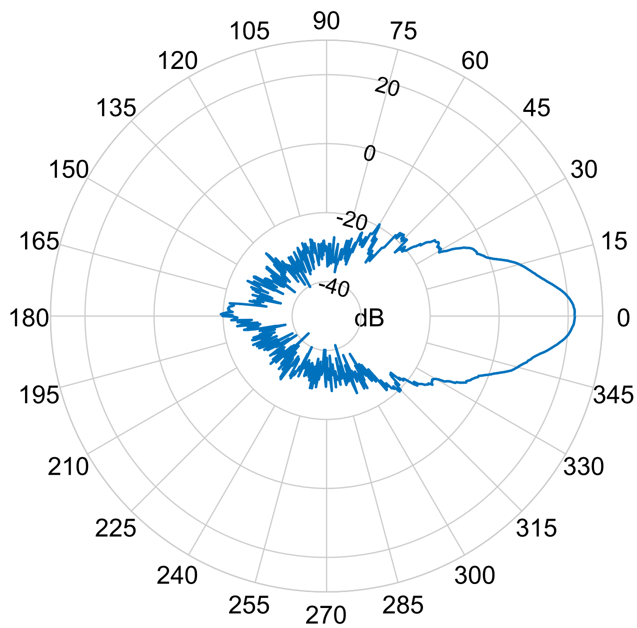

(b) Elevation plane pattern

Figure 2.6. Antenna pattern measurement results for the azimuth and elevation planes.

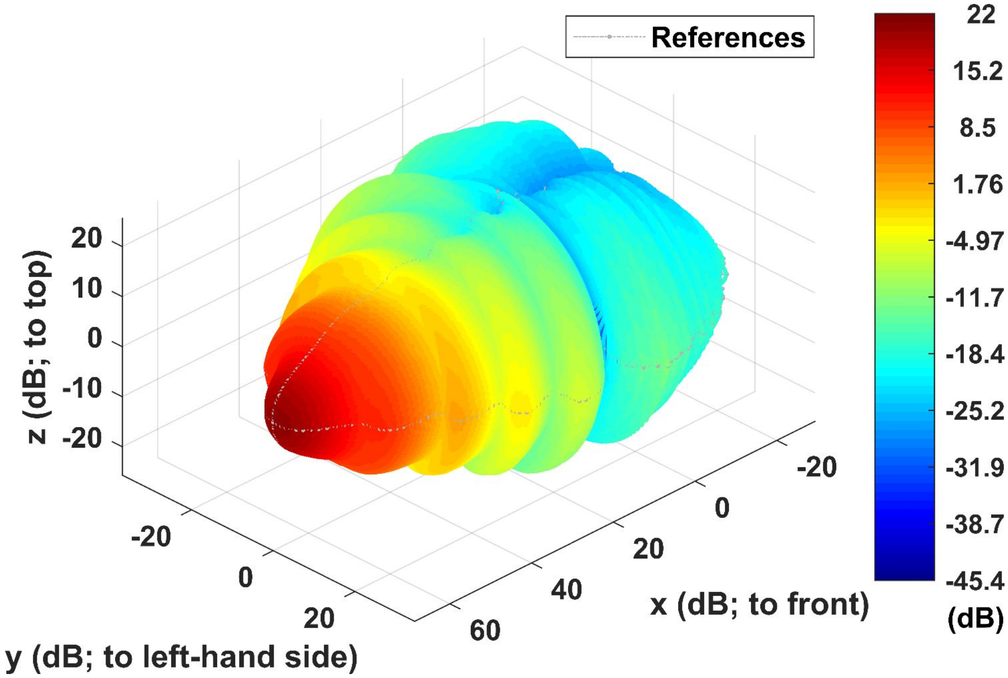

Figure 2.7. Full 3D antenna pattern filling.

of 15.2° and an elevation of -3.9°. The corresponding gain by the 3D interpolated antenna pattern was 11.05 dB.

2.4 Measurement Results and Analysis

In Figure 2.9, 49 of the 50 static sites are shown on a Google map of the USNA campus. One large-scale site was ignored in our analysis because the data collected there were influenced by rain.

2.4.1 Line-of-Sight (LoS) Sites

For LOS sites (24 in total), we compared the measurement results with the International Telecommunication Union (ITU) site-general model for propagation over rooftops [66]:

$$PL(d, f) = 10 \cdot \alpha \cdot \log_{10}(d) + \beta + 10 \cdot \gamma \cdot \log_{10}(f) \\ + N(0, \sigma), \tag{2.1}$$

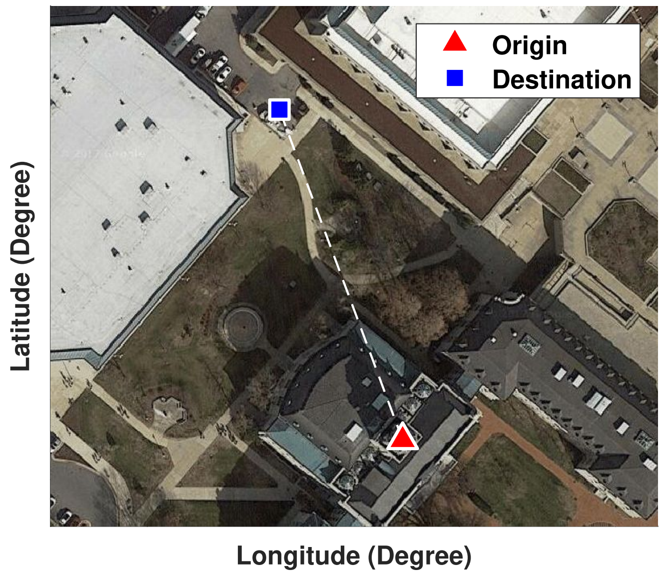

(a) TX and RX locations

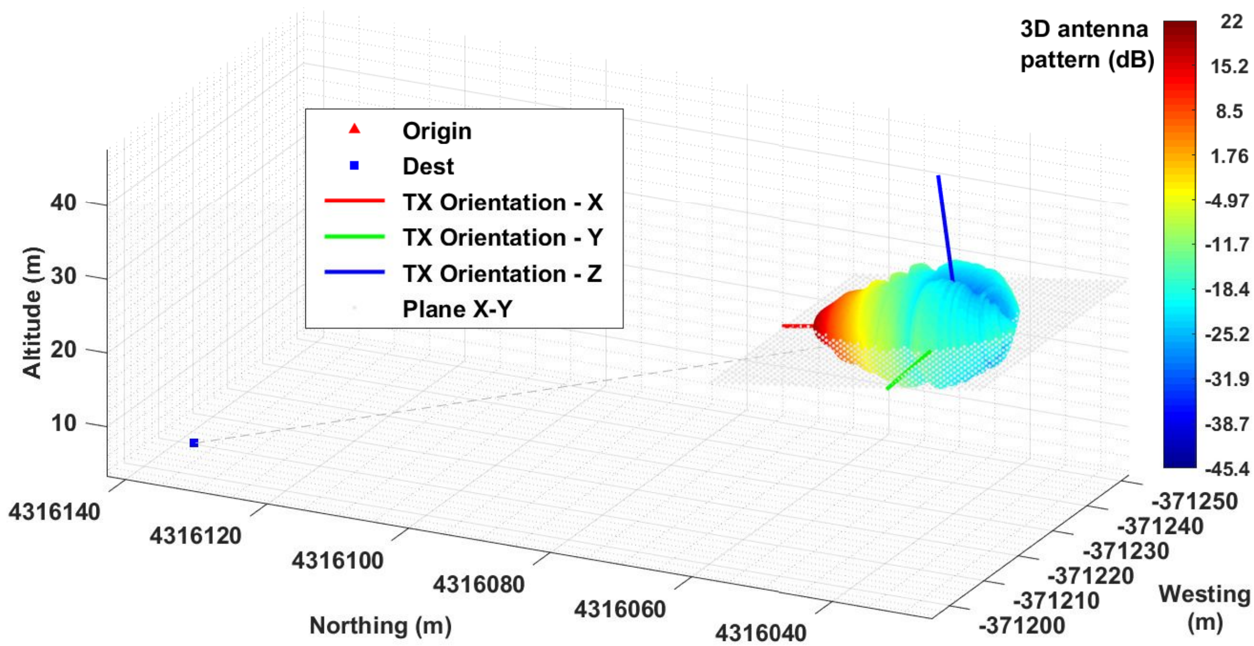

(b) TX antenna gain computation in 3D

Figure 2.8. Illustration of antenna gain evaluation.

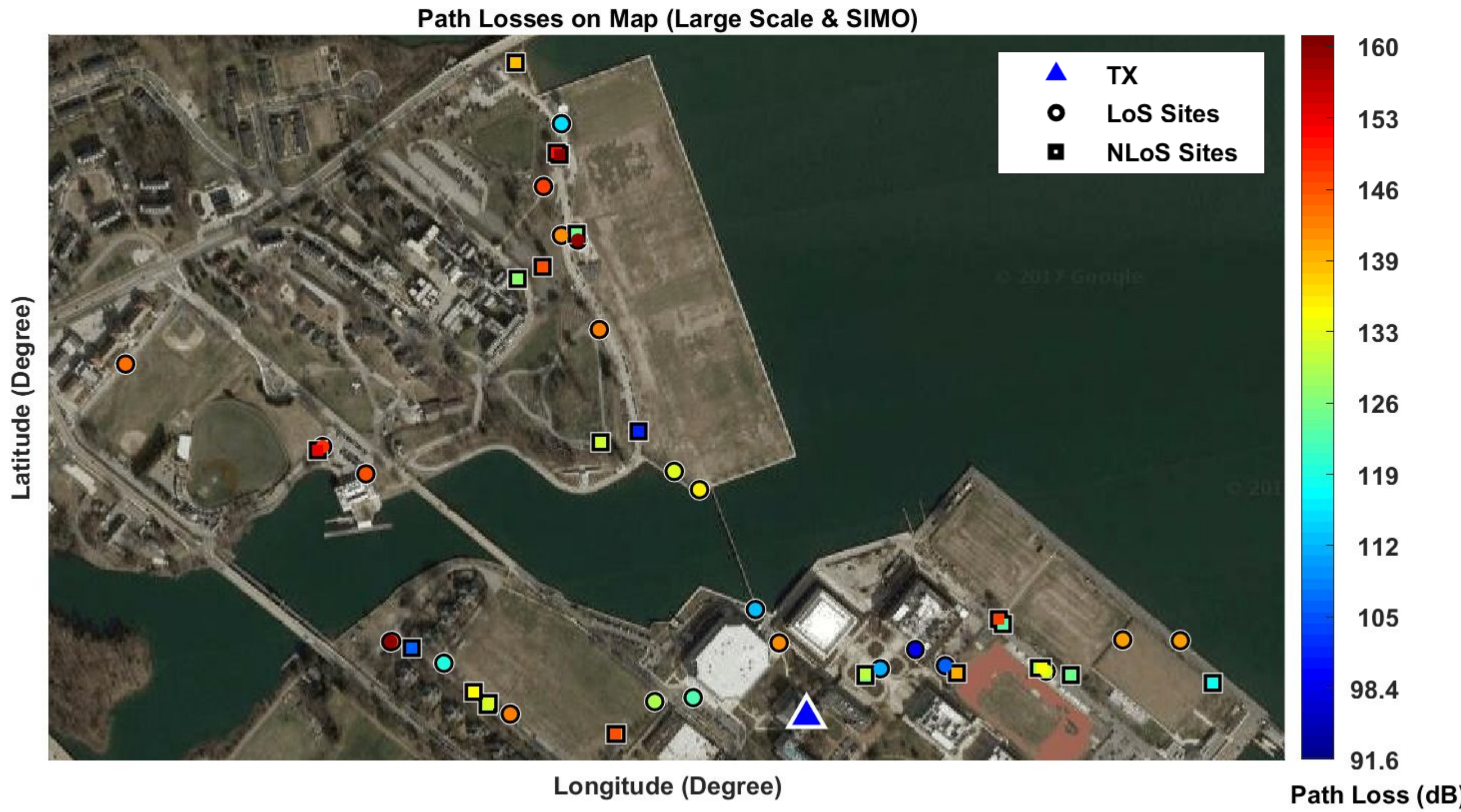

Figure 2.9. Overview for the basic transmission losses of the large-scale and SIMO measurements. The geographic locations for the measurement sites are shown on a Google map of the USNA campus, with their corresponding worst-case basic transmission losses illustrated by color labels.

where d is the 3D direct distance between the TX and RX in meters and f is the operating frequency in GHz. In our case, $f = 28$ GHz. The parameters α, β, γ, and σ are chosen for the LoS propagation in a suburban environment [66]:

$$\begin{cases} \alpha = 2.29 \\ \beta = 28.6 \\ \gamma = 1.96 \\ \sigma = 3.48\ . \end{cases} \tag{2.2}$$

These parameters are recommended for a distance range of 55 m to 1200 m at 2.2–73 GHz frequency.

For a better comparison, we also considered two other models as references. The first is the close-in (CI) free space reference distance path loss model:

$$PL(d) = PL_{FS}(d_0) + 10 \cdot n \cdot \log_{10}\left(\frac{d}{d_0}\right), \tag{2.3}$$

$$PL_{FS}(d_0) = 20 \cdot \log_{10}\left(\frac{4\pi d_0}{\lambda}\right), \tag{2.4}$$

where n is the path loss exponent, $PL_{FS}(d_0)$ is the free-space propagation loss at a distance of $d_0 = 1$ m with isotropic antennas, and λ is the carrier wavelength. The second is the alpha-beta-gamma (ABG) model on which the ITU site-general model is based:

$$PL(d) = 10 \cdot \alpha \cdot \log_{10}(d) + \beta + 10 \cdot \gamma \cdot \log_{10}(f). \tag{2.5}$$

Note that α here acts as the path loss exponent.

We have fit these two reference models to our LoS measurement results. To deal with GPS sample errors, the median values of latitude, longitude, and altitude measurements for each site were used as that site's geographic location to compute the site distance to the TX. And for the ABG model, we set $\gamma = 1.96$ as recommended by ITU, given that we had only one carrier frequency at 28 GHz.

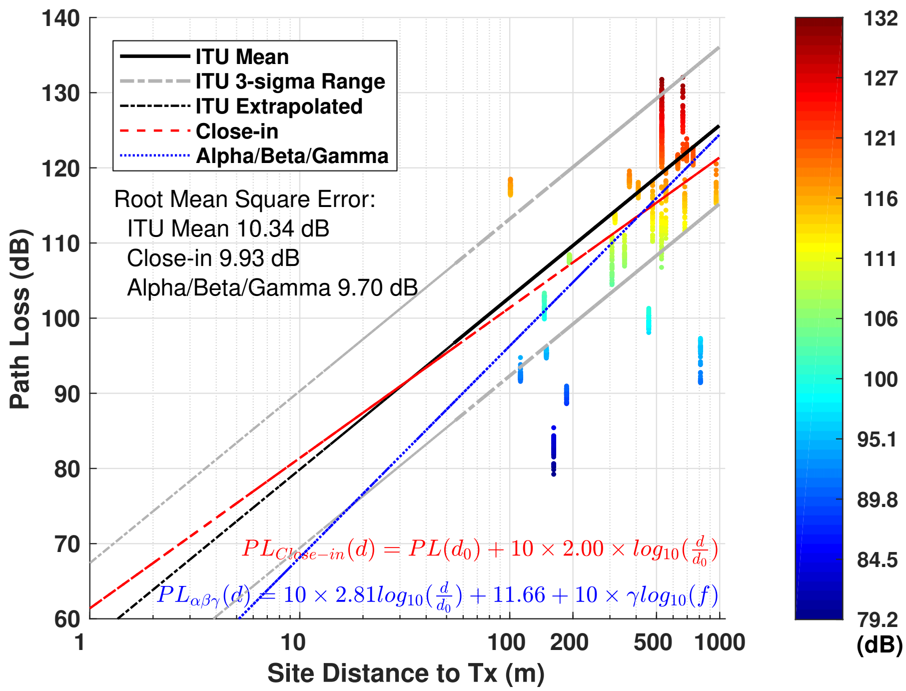

(a) For the LoS measurements

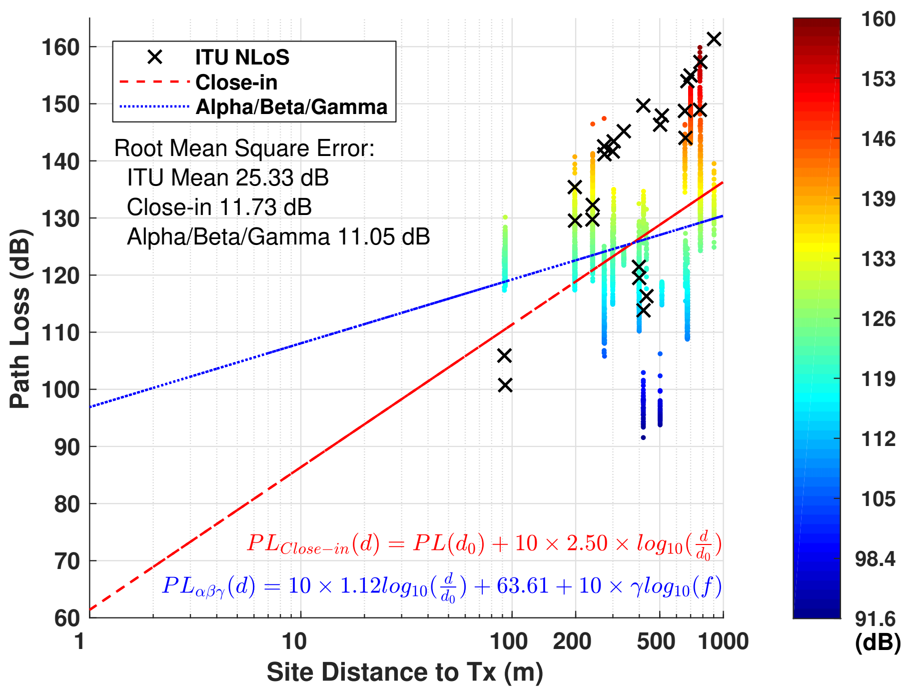

(b) For the NLoS measurements

Figure 2.10. Model comparison for LoS and NLoS measurements.

All three models, together with the measurement results, are presented in Figure 2.10a. The ITU model provides path loss predictions in the form of Gaussian variables, and their 3-sigma range covers the measured path losses reasonably well, even though if we extrapolate the ITU model to $d = d_0 = 1$ m, its mean path loss would be smaller than the corresponding free-space propagation loss (FSPL). This issue affects the ABG type of models in general. In our case, the ABG model has the lowest root mean square error (RMSE) at 9.70 dB, but its predicted path loss quickly descends below FSPL as the distance decreases. Hence, the ABG model does not generalize well outside the distance range for its measurement data.

The resulting path loss exponents for the CI and ABG reference models are 2.00 and 2.81, respectively. For the LoS dataset, these two models perform 0.41 dB and 0.64 dB better than the ITU model, respectively, in terms of RMSE. Basically, within the distance range of the LoS measurement dataset, these three models are equivalent, and the ITU model performs well.

The four sites with lower path losses than the ITU 3-sigma range were further investigated through their PDPs. As very strong multipath components were observed for all of these sites, it is still possible for even narrow mmWaves to have multipath components that dramatically enhance the signal. For the closer two sites, this was expected because they were surrounded by buildings. However, the two sites at farther distances were in open areas, and the most reasonable origins of the multipath were reflections from buildings close to the TX, as many of these buildings have sloped ceilings.

2.4.2 Non-Line-of-Sight (NLoS) Sites

For the 25 NLoS sites, the site-specific model for propagation over rooftops defined in ITU-R P.1411-9, Section 4.2.2.2 [66] was utilized to predict the path loss for each site. Similar to the LoS case, the CI and ABG models were compared with the ITU model as references. This time, γ was set to 2.30 for the ABG model, as recommended by ITU for NLoS above-rooftop propagation from 260 m to 1200 m at 2.2–66.5 GHz in an urban high-rise environment, which was the most suitable for our purposes.

Table 2.2. Key Parameters for Channel Models

Model	**LoS**					**NLoS**				
	n	$\boldsymbol{\alpha}$	$\boldsymbol{\beta}$	$\boldsymbol{\gamma}$	**RMSE (dB)**	**n**	$\boldsymbol{\alpha}$	$\boldsymbol{\beta}$	$\boldsymbol{\gamma}$	**RMSE (dB)**
ITU	N/A	2.29	28.6	1.96	10.34	N/A	N/A	N/A	N/A	25.33
Close-in	2.00	N/A	N/A	N/A	9.93	2.50	N/A	N/A	N/A	11.73
ABG	N/A	2.81	11.66	1.96	9.70	N/A	1.12	63.61	2.30	11.05

Figure 2.10b shows the ITU predictions together with the reference models and NLoS measurement results. For the NLoS data, the ITU model shows a trend of following the measured path loss, but it has over-estimated predictions for most of the sites. Only five of the NLoS sites had measured path losses that were clearly larger than the corresponding ITU predictions. Furthermore, the ABG model does not agree well with the close-in one, with resulting path loss exponents of 1.37 and 2.50, respectively. This may be caused by an over-fitting of the ABG model to our NLoS path losses. However, both of these reference models outperformed the ITU predictions by around 14 dB in RMSE. Table 2.2 summarizes the key parameters for the obtained channel models.

Several factors may have reduced the performance of the ITU site-specific model. First, the buildings on the USNA campus are not geometrically arranged exactly like those defined in the ITU suburban area propagation model. The over-rooftop propagations often span multiple building rows, which alters the blockage and reflection conditions. Also, for many of our sites, the ITU over-rooftop model with a limited number of buildings would be a better fit, which may ameliorate the path loss overestimation for propagations beyond the building area.

Second, the parameter ranges defined in the ITU model do not always agree with those for our NLoS sites. For example, the street width for most of our sites was over the defined limit. For these cases, we used the upper bound for the model, 25 m, in the calculation, so the model may have underestimated the path losses for sites relatively close to the TX by considering reflections from buildings that do not exist. For sites that were further away, more buildings are positioned between the TX and the RX, which may have caused an overestimation.

Third, at around 10 of the NLoS sites, the LoS propagation was directly blocked by vegetation, not buildings. A few other sites have foliage near their LoS paths. ITU-R P.1411-9 does not consider the propagation effects caused by vegetation due to the complexity.

2.4.3 Continuous Tracks

Two continuous signal recordings were conducted to investigate the shadowing effect for a simulated moving RX at walking speed. The basic transmission losses were calculated for each second of signal recording (see Figure 2.11). As can be observed, the path losses on Holloway road illustrate the shadowing effect of buildings and benches, while those on Upshur road illustrate the shadowing effect of trees. In Figure 2.11c, the starting part of the track is zoomed in, and trees are indicated by green rectangles.

For the track on Holloway road (Figure 2.11b), the most significant blockage was from Michelson Hall, which caused approximately 30 dB of additional path loss to half of the track. Rickover Hall partially blocked the track by around 20 dB. The dotted lines in Figure 2.11b show where these blockages started on the track. There were also metal stadium benches on the northeast side of Ingram Field adjacent to the measurement route, which caused around 20 dB of additional path loss. This is more clear on the part of the track with no building blockages, where a path loss peak shows up behind each one of the benches.

For the track on Upshur road (Figure 2.11c), the two benches next to the measurement route were farther away from the track and did not block the signal significantly. For this set of data, the effect of foliage shadowing is of interest. Trees were planted on the TX side adjacent to the pathway and a few path loss peaks shown in Figure 2.11c correspond well with the locations of these trees.

2.4.4 Discussion

We have focused on the large-scale path loss, comparing our measurements with predictions obtained by following ITU-R P.1411-9 [66] on propagation over rooftops. Our data show that a richer set of channel state information, including multipath scattering and location-specific building geometries, is necessary to produce more reliable coverage predictions. In the LoS situation, the measurements agree reasonably well with the ITU predictions, while for the NLoS situation, most of the predictions appear to have higher path losses than the corresponding measurement results. Limiting the building number, extending the model

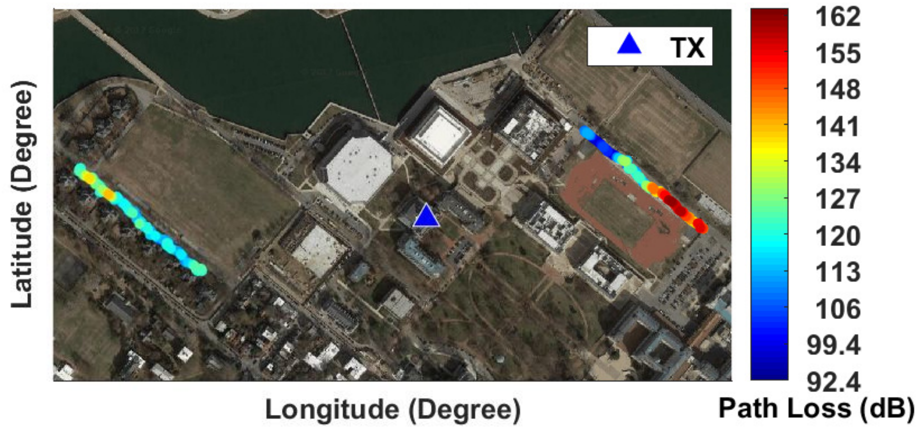

(a) Basic transmission losses for two continuous tracks

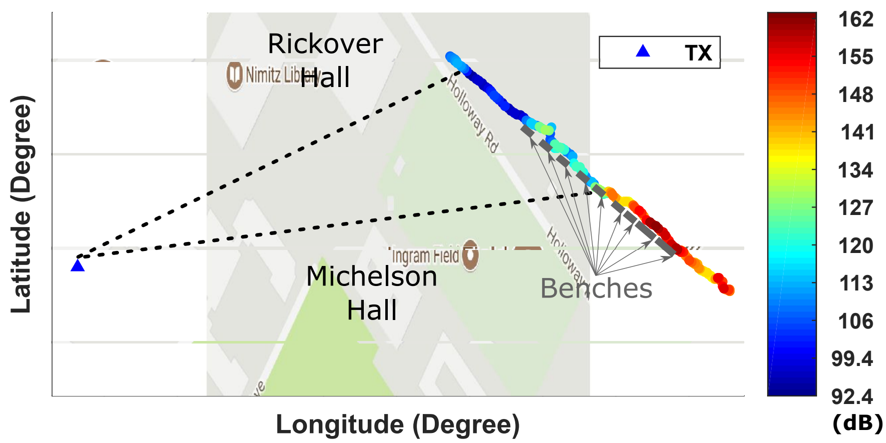

(b) Track on Holloway Road

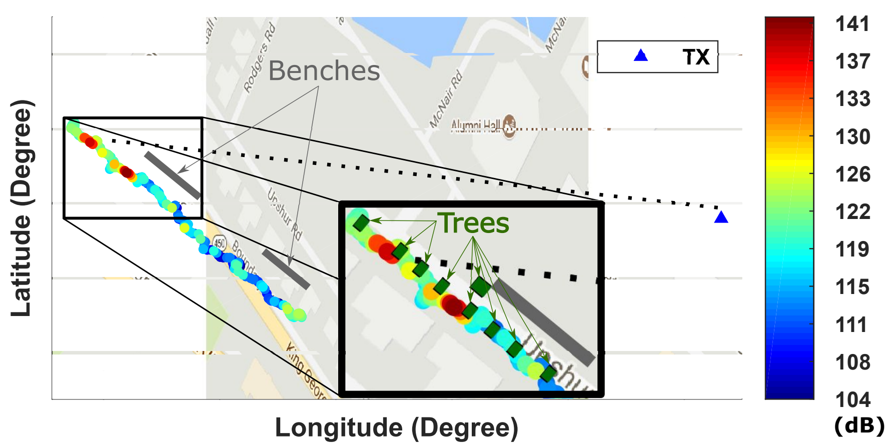

(c) Track on Upshur Road

Figure 2.11. Basic transmission losses for continuous tracks on Google Maps.

with sloped ceilings, and considering over-rooftop propagations spanning multiple building rows may help improve the ITU site-specific model for suburban environments.

According to our model comparison results, the CI and ABG models do a good job of predicting large-scale path loss in both LoS and NLoS cases. Furthermore, the ABG model, in general, can provide a better fit for a given set of data. However, it may give non-physical results beyond the distance range over which the data are collected. Because of this, care should be taken when using the ABG model out of its defined range.

The continuous recordings back up channel modeling attempts that consider environmental information, for example, through the radio environment map [89] and ray tracing [90] approaches. Moreover, the results indicate the possibility of increasing large-scale path loss prediction accuracy for statistical models with simple but site-specific environment geometry, which would balance computation complexity and model performance.

2.4.5 Future Works

In the future, we plan to: (1) Further investigate the ITU channel modeling recommendation for possible extensions or improvements, e.g. sloped ceilings, over roof-tops propagations spanning multiple rows, and limitation on the building number; (2) Explore the possibility of enhancing statistical channel model performance with side geometric information; (3) Examine the influence on large-scale path loss from the vegetation; (4) Look closer into the SIMO measurements for means to utilize the presented multipath effects.

2.5 Conclusion

In this paper, we discussed the implementation of a custom-designed broadband channel sounder and explained how we used it for a measurement campaign that focused on the propagation of mmWaves in suburban environments at 28 GHz. The resulting basic transmission losses for LoS and NLoS sites were separately compared with the corresponding propagation predictions based on the ITU-R P.1411-9 recommendation. The site-general LoS model for propagation over rooftops in suburban environments agreed with our measurements reasonably well, but the corresponding site-specific NLoS model overestimated the path loss for most of the NLoS sites. Two continuous measurement tracks were also constructed. The results illustrated that the knowledge of geometric features may increase the prediction performance for large-scale path losses, which backs up the radio environment map approach for channel modeling in future communication networks.

Acknowledgment

We would like to thank the faculty members from the Department of Electrical and Computer Engineering at the United States Naval Academy for their kind assistance during the measurement campaign.

3. IMPROVING MILLIMETER-WAVE CHANNEL MODELS FOR SUBURBAN ENVIRONMENTS WITH SITE-SPECIFIC GEOMETRIC FEATURES

Reprinted, with permissions, from: Y. Zhang, D. J. Love, N. Michelusi, *et al.*, "Improving millimeter-wave channel models for suburban environments with site-specific geometric features," in *2018 International Applied Computational Electromagnetics Society Symposium (ACES)*, IEEE, Mar. 2018, pp. 1–2. DOI: 10.23919/ropaces.2018.8364140. Editorial changes have been made to meet Purdue's requirements on the dissertation.

3.1 Introduction

Millimeter wave (mmWave) bands have become the most promising candidate for enlarging the usable radio spectrum in future wireless networks such as 5G [3]. Since frequent and location-specific blockages are expected at mmWaves, the challenge is understanding the propagation characteristics of mmWave signals and accordingly predicting the channel state information as needed, so that the high mobility requirements of these wireless networks can be addressed in real-time.

The majority of current research has focused on urban areas with high population densities [3], [73], [84]. Very few measurement campaigns have been performed in suburban and rural environments. Moreover, statistical models for point-to-point links have received significant attention, but this approach ignores all or most of the site-specific geometric features, which mmWaves are sensitive to due to blockages. In this paper, we explore this research gap by focusing on suburban environments and improving standard 5G channel models with site-specific geometric features.

3.2 Mm-Wave Propagation Measurements for Suburban Environments

An outdoor propagation measurement campaign was carried out at the United States Naval Academy (USNA) in Annapolis, Maryland. The transmitter (TX) was temporarily installed on the Mahan Hall clock tower to emulate a typical 5G suburban microcell deployment. A custom-designed broadband sliding correlator channel sounder was used as the receiver (RX) and moved around the campus to obtain path loss measurements. More details for the measurement setup can be found in [67].

3.3 Building Blockage Analysis

One approximately 200-m-long straight track was chosen for a continuous signal recording, to investigate the shadowing effect of buildings on a moving user. The resulting basic transmission losses are shown in Figure 3.1a. The numbers in the boxes are distances to the TX. The dotted lines illustrate the boundaries between the line-of-sight (LoS) area and the none-line-of-sight (NLoS) area due to blockages. As we can see, the path loss values clearly illustrate the shadowing effect caused by the buildings. The most significant blockage was from Michelson Hall, which obstructed the southern half of the track. Rickover Hall partially blocked the track at the north end.

To estimate the path loss caused by building blockages, the knife-edge diffraction (KED) model [73] was utilized. In our case, the Universal Transverse Mercator (UTM) coordinate system was extended with height to form a 3-dimensional (3D) space for computing the effective height of the obstructing screen, as well as the distances between the TX, the RX, and the screen. Note that the path obstruction may occur either on a horizontal roof edge or a vertical side edge of the building. Finally, the screen height was computed as the distance between the obstruction point and the direct Euclidean path between the TX and the RX. The resulting diffraction losses were used to shift the large-scale path loss predictions from the International Telecommunication Union (ITU) site-general model for propagations over rooftops [66]:

$$PL(d, f) = 10 \cdot \alpha \cdot \log_{10}(d) + \beta + 10 \cdot \gamma \cdot \log_{10}(f) + N(0, \sigma), \tag{3.1}$$

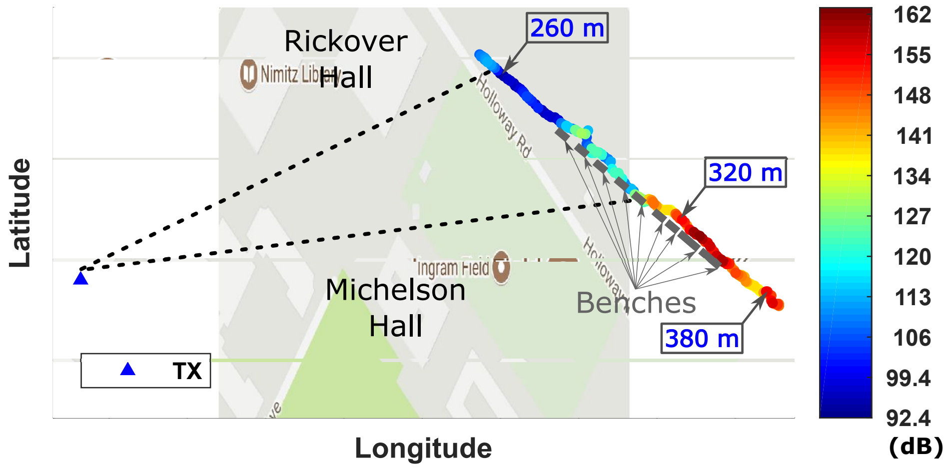

(a) Track with basic transmission losses along Holloway Road

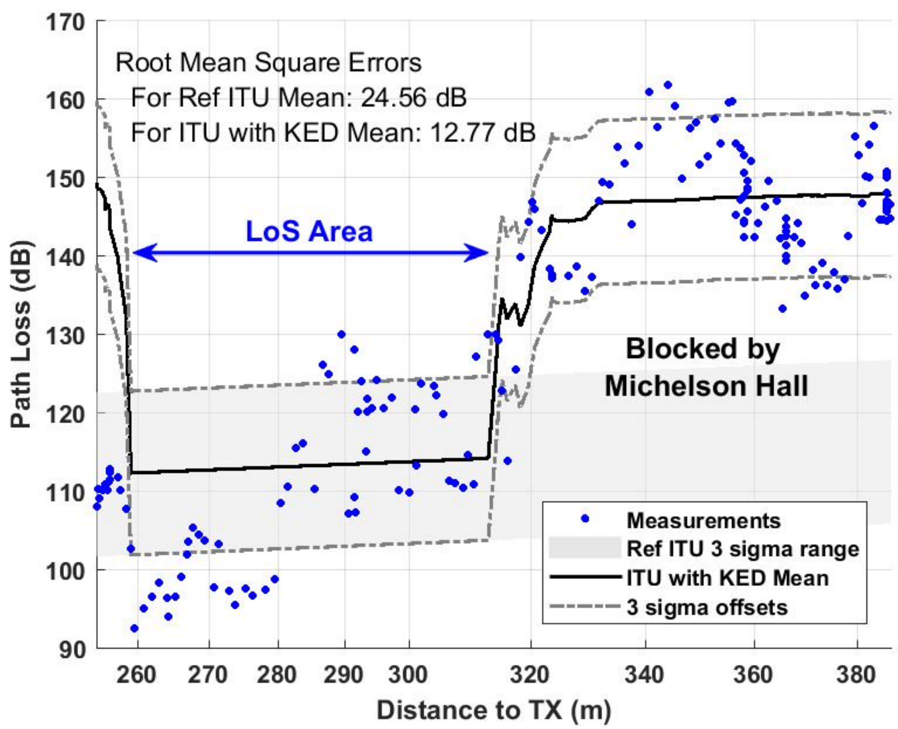

(b) Path loss for the modified ITU model

Figure 3.1. Considering building blockages to improve a statistical channel model.

where d is the 3D direct distance between the TX and the RX in meters and f is the operating frequency in GHz. In our case, $f = 28$ GHz. The parameter values $\alpha = 2.29$, $\beta = 8.6$, $\gamma = 1.96$, and $\sigma = 3.48$, were chosen for the LoS propagation in a suburban environment [66], which are recommended by ITU for distances from 55 m to 1200 m at 2.2–73 GHz frequency.

Figure 3.1b shows the final results. The ITU model provides path loss predictions in the form of Gaussian variables. Accordingly, 3-sigma ranges for both the original and shifted ITU models are shown and root mean square errors (RMSEs) are computed separately according to the mean of each model. Note that the mean of the ITU predictions is proportional to $log_{10}(d)$, the logarithmic value of the distance between the TX and the RX. To better reflect this trend, our visualization here created the x-axis on a logarithmic scale, even though the result is not much different than a linear-scale plot in the distance range of interest. As we can see, the modified ITU predictions follow the measurement data much better than the original ones, providing an RMSE improvement of 11.79 dB.

Another observation is that for distances below 280 m, the original ITU model overestimated the path loss by around 20 dB. This may be caused by some strong reflection path(s). Also, in the same distance range, the KED model overestimated the attenuation caused by Rickover Hall. This was probably because the blockage happened at the southern vertical edge of the building, which corresponds to a very short obstructing screen, whereas the KED model applies for a screen with infinite height. Still, the KED model helped identify the path loss peak below 260 m.

3.4 Foliage Analysis

The effect of foliage for modeling mmWave channel is a vital consideration for suburban environments as scattering and absorption at these frequencies can significantly attenuate the signal. In our measurement campaign, eleven sites had partial or total obstruction of the LoS signal from foliage, ranging from a single tree to a small grove of trees. Our measurement results were compared against four well-known empirical models [91] that are valid in this frequency range: COST235, Weissberger, ITU-R, and FITU-R models.

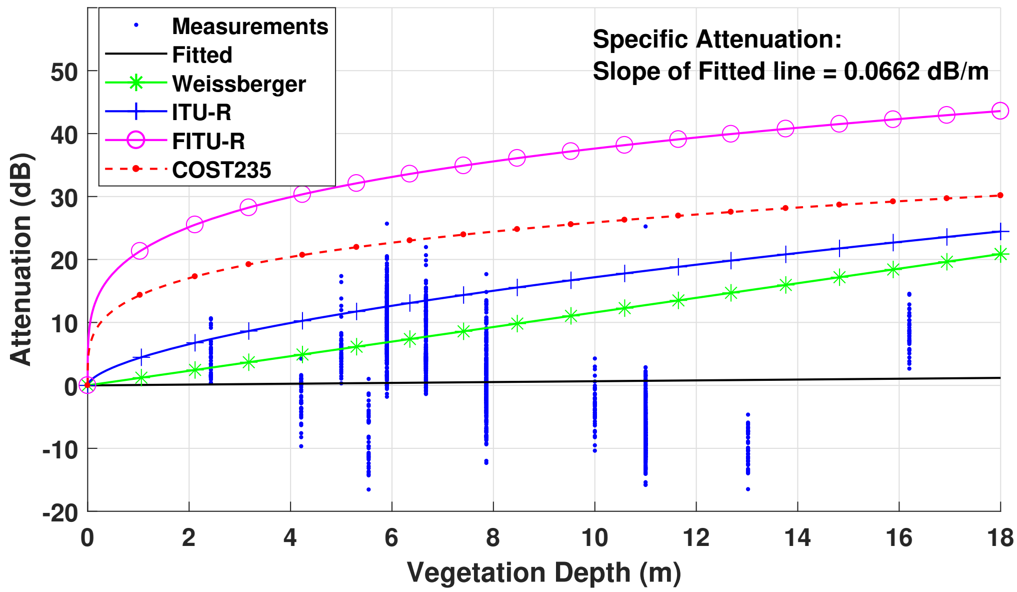

Figure 3.2. Comparison of computed and measured path loss at 28 GHz.

Figure 3.2 illustrates our measured *excess* vegetation attenuation versus vegetation depth as well as existing model predictions. From the figure, we can see that the ITU-R model and Weissberger's model both work well compared to our measurement results, especially when the vegetation depth is below 10 m. The other two models, FITU-R and COST235, overestimate the extra attenuation caused by the trees in our case. We can also observe that the mean measured value of foliage attenuation (0.07 dB/m) is significantly less than those of model-predicted values. In fact, our measurements demonstrate a significant amount of multipath energy arriving at the receiver, likely being scattered from other objects in the environment. As a result, we recorded a greater signal strength than what would be predicted by these simple single-path attenuation models.

3.5 Conclusion

In this paper, we illustrate two measurement- and geometry-based techniques for improving existing statistical mmWave channel models. Our approach is suitable for a holistic, network-level model that utilizes side information and the results could be updated in real-time. Our techniques demonstrate a modest, but significant, overall improvement in propagation modeling accuracy.

4. PROPAGATION MODELING THROUGH FOLIAGE IN A CONIFEROUS FOREST AT 28 GHZ

Reprinted, with permissions, from: Y. Zhang, C. R. Anderson, N. Michelusi, *et al.*, "Propagation modeling through foliage in a coniferous forest at 28 GHz," *IEEE Wireless Communications Letters*, vol. 8, no. 3, pp. 901–904, Jun. 2019. DOI: 10.1109/lwc.2019.2899299. © 2019 IEEE. Editorial changes have been made to meet Purdue's requirements on the dissertation.

4.1 Introduction

With the rapid standardization process of 5G communication networks [92], millimeter waves (mmWaves) have garnered great attention worldwide from industry, academia, and government. A major issue is to better understand the propagation characteristics of mmWave signals. Many mmWave channel measurement campaigns have recently been carried out in urban and suburban environments [3], [44], [45], [73]. However, very limited effort has been put into validating and improving currently available channel models in overcoming vegetation blockages. This is a key element of sensor data collection in forestry and agriculture [93] for preventing costs incurred by under/over-deployment of the sensors and improving their communication performance. In [94], a constant excess path loss of around 25 dB was observed at 28.8 GHz through a pecan orchard for paths with roughly 8 to 20 trees. More recent works [45], [95] reported low attenuation values per unit foliage depth of 0.07 dB/m at 28 GHz and of 0.4 dB/m with 3 dB deviation at 73 GHz, respectively. In [96], attenuation with a dual-slope structure was observed for out-of-leaf measurements at 15 GHz, 28 GHz, and 38 GHz in forest environments. Moreover, even though a variety of modeling approaches have been considered, most of them ignore site-specific geographic features [45]. A comprehensive analysis for attenuation in vegetation is required to validate those observations and make improvements to mmWave propagation modeling.

We explore this research gap by investigating the mmWave propagation at 28 GHz through vegetation. Using a portable custom-designed sliding correlator sounder, we carried out a measurement campaign in a coniferous forest near Boulder, Colorado, and obtained a total of 1415 basic transmission loss measurements. Relevant foliage regions were extracted from the United States Geological Survey (USGS) LiDAR and terrain elevation data. Tree locations were also manually labeled according to the LiDAR data and to high-resolution satellite images from Google Maps. These data enabled us to view channel modeling in a site-specific manner. A comprehensive model comparison is provided to elucidate the pros and cons of different modeling approaches for predicting signal attenuation through vegetation. Novel site-specific models with consistently better performance than existing models are developed. They are fully automatic, easy to implement, and feasibly applicable to machine learning frameworks.

4.2 Measurement Setup

The measurement system in our previous work [44] was utilized. The receiver (RX), which had a chip rate of 399.95 megachips per second, was installed in a backpack and powered by a lithium-ion polymer battery for portability purposes. As illustrated in Figure 4.1, the transmitter (TX) was set up at the edge of the forest, while the RX was moved in the coniferous forest to continuously record the signal along with the GPS location information. Boulder is a semi-arid environment with low humidity and minimal rainfall. Measurements were performed on a warm spring day under mostly sunny conditions. The TX antenna was adjusted before each signal recording activity to point to the middle area of the track to be covered. Beam alignment was achieved at the RX side using a compass. One basic transmission loss result was computed for each second of the recorded signal to match the GPS data. We also obtained satellite images from Google Maps and LiDAR data from the United States Geological Survey (USGS). Tree locations were manually labeled accordingly. Foliage regions were automatically extracted by comparing the LiDAR data with USGS terrain elevation data. These site-specific geographic features of the forest are illustrated in Figure 4.1b. We have zoomed in on the dotted-square area in Figure 4.1a to better illustrate

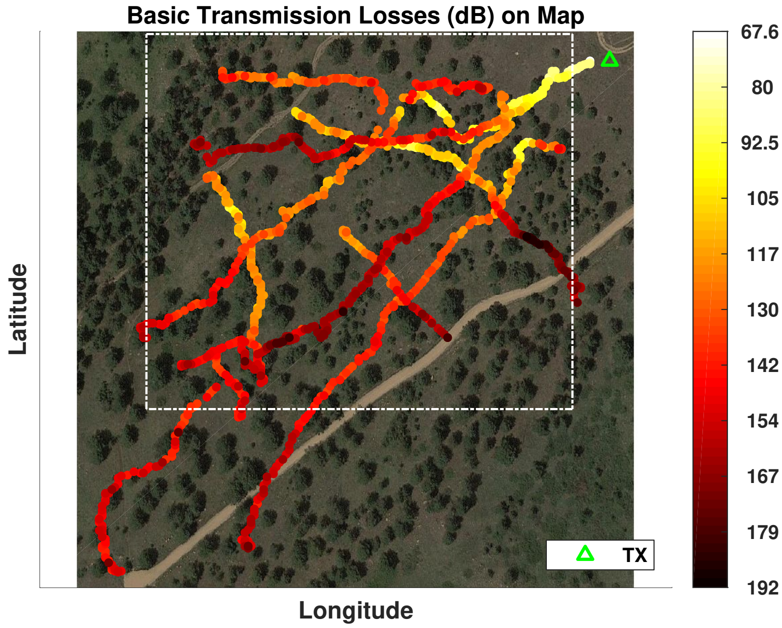

(a) RX tracks illustrated with basic transmission loss results

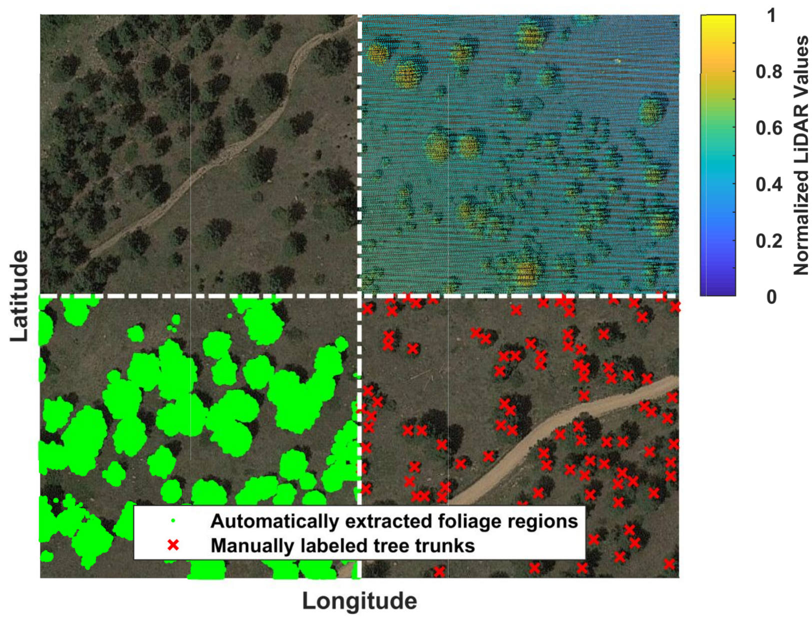

(b) Site-specific information available for the measurement site

Figure 4.1. Measurement results and the site-specific features for the measurement campaign.

the site-specific features. Satellite images from Google Maps are used here as background. Overlaid on top are LiDAR data, foliage regions, and trunk locations, respectively.

4.3 Foliage Analysis for the Coniferous Forest

We compared three empirical foliage analysis models: the partition-dependent attenuation factor (AF) model [74], the ITU-R obstruction by woodland model [75], and Weissberger's model [76]. To tune these models, four parameters were computed for each measurement location: the distance between the TX and the RX, the number of tree trunks within the first Fresnel zone, the foliage depth along the line-of-sight (LoS) path, and the foliage area within the first Fresnel zone. These computations were performed in a three-dimensional (3D) reference system using Universal Transverse Mercator coordinates (x, y) and altitude. Based on these results, site-specific models were introduced to improve path loss predictions.

All channel models considered here generate excess attenuation values on top of a site-general channel model. We use the free-space path loss (FSPL) model as the baseline generic model. The path loss PL in dB at the RX location s is then composed of two parts:

$$PL(s) = FSPL\,[d(s)] + EPL(s)\,,$$

where $FSPL\,[d(s)]$ is the FSPL in dB at a RX-to-TX distance of d at s, and $EPL(s)$ is the excess path loss in dB at s.

4.3.1 AF Propagation Model [74]

The partition-dependent AF propagation model takes advantage of site-specific information by assuming that each instance of one type of obstacle along the LoS path will incur a constant excess path loss. In our case, we counted the number of trees, $N(s)$, along the LoS path to s and added a constant excess path loss in dB, L_0, for each of the trees, as follows:

$$EPL(s) = N(s) \cdot L_0\,.$$

There are different methods for determining $N(s)$. Considering the forest size and the number of RX locations involved, it is extremely difficult and time-consuming to count N at each s on-site. In our work, we simplified the trees, making them vertical lines rather than estimating the cylinder of each tree. Then, the number of trees within the first Fresnel zone for each s was estimated based on manually labeled trunk locations and used as the number of obstacle trees.

Figure 4.2 shows the predictions obtained from the AF model. The unknown constant L_0 was fit according to the measurement data, resulting in a value of 6.47 dB per tree. As can be seen, the AF model closely follows the shape formed by the measurement results. However, it suffers in predicting the correct amount of excess path loss in general. This is expected because we have only considered the trunk locations for counting trees, but their physical sizes also play a critical role in attenuating the signal. The root mean squared error (RMSE) for the AF model compared with the measurements is 27.96 dB, achieving an 11.47 dB improvement over the FSPL model but still significantly worse than those for the other two empirical models discussed below. In a word, the predictions from the AF model fit the shape of the measurement results but have poor overall accuracy. We observe that it may be possible to improve the AF model by classifying trees into different size categories and assigning each category a loss value. However, in our case, trees grew in clusters, making it extremely challenging to distinguish individual canopies and to properly classify trees.

4.3.2 ITU-R Obstruction by Woodland Model [75]

The ITU-R obstruction by woodland model assumes one terminal (the TX or the RX) is located within woodland or similar extensive vegetation, which fits well our measurement scenario. Instead of the number of trees, the ITU model uses the length of the path within the woodland in meters, $d_w(s)$, which is the distance from the woodland edge to the terminal in the woodland, to estimate the excess path loss:

$$EPL(s) = A_m \left[1 - \exp(-d_w(s) \cdot \gamma / A_m)\right], \tag{4.1}$$

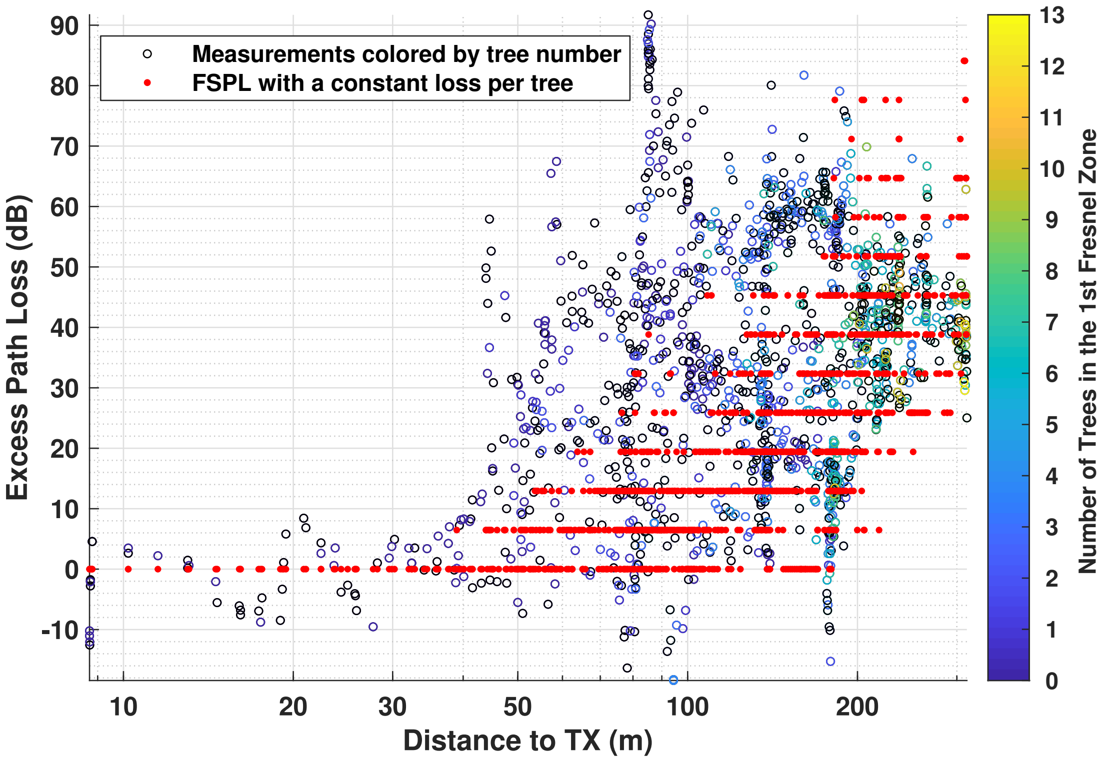

Figure 4.2. The AF propagation model simplifies to a constant-loss-per-tree model in our case.

where $\gamma \approx 6$ dB/m is the typical specific attenuation for very short vegetative paths at 28 GHz, and A_m is the maximum attenuation in dB. The most distinguishing feature of this model is the upper limit A_m imposed on the excess path loss.

Since the TX was installed approximately 15 m away from the forest, this offset has been taken away from the 3D RX-to-TX distance to estimate $d_w(s)$, with the negative values clipped to zero. Also, A_m is yet to be determined in [75] for 28-GHz signals, so we fitted it to our measurement results to obtain the best possible performance, which yielded $A_m \approx 34.5$ dB. The resulting predictions are plotted in Figure 4.3. The ITU model exhibits the best fit among the empirical models considered, with an overall RMSE of 20.08 dB. However, it clearly overestimates the path loss for locations with d_w smaller than 30 m. At those locations, the LoS path may be clear or blocked by only a couple of trees, differing from a typical woodland blockage scenario. On the other hand, the ITU model underestimates the path loss for large d_w. As a comparison, the predictions from one site-specific model, which

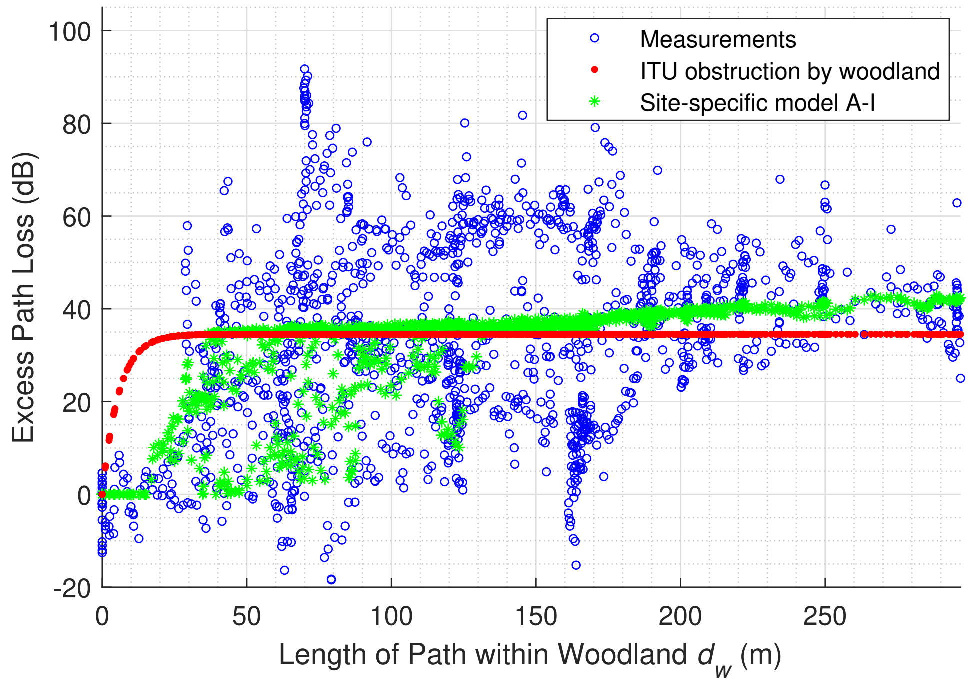

Figure 4.3. Predictions from the ITU obstruction by woodland model.

is covered in Section 4.3.4, are also shown. The site-specific model follows the measurements better than the ITU model at the lower and higher ends of d_w.

4.3.3 Weissberger's Model [76]

Weissberger's model, or Weissberger's modified exponential decay (WMED) model, can be formulated as follows:

$$EPL(s) = \begin{cases} 0.45\, f_c^{0.284}\, d_f(s) & \text{, if } 0 < d_f(s) \leqslant 14 \\ 1.33\, f_c^{0.284}\, d_f^{0.588}(s) & \text{, if } 14 < d_f(s) \leqslant 400 \end{cases}$$

where f_c is the carrier frequency, and $d_f(s)$ is the foliage depth in meters along the LoS path for the RX location s. The model treats locations with $d_f(s)$ >14 differently from those with less foliage blockage.

We have taken an image processing approach to automatically obtain the site-specific foliage depth, $d_f(s)$, which is the accumulated distance for the intersections of the direct path and the foliage regions. Both the LiDAR data and the terrain elevation data from the USGS were rasterized onto the same set of reference location points. The foliage regions were then extracted by thresholding their difference, resulting in the foliage regions illustrated in Figure 4.1b. Along the LoS path, the ratio of the number of foliage region pixels over the total number of pixels was calculated and multiplied with the corresponding 3D RX-to-TX distance to get the foliage depth for each RX location.

Figure 4.4a compares the predictions from the WMED model with the measurement results. Overall, the WMED model gives a reasonably good RMSE value of 22.19 dB. As shown in Figure 4.4a, Weissberger's model slightly underestimates the loss of RX locations with shallow vegetation blockages and overestimates the loss of those with deep vegetation blockages. To better illustrate this, results from *site-specific model A-I* are shown as a reference.

4.3.4 Site-specific Models

Using high-precision publicly available geographic information, existing channel models can be tuned with well-estimated site-specific parameters. As a result, simple but powerful site-specific models can be constructed as alternatives. We refer to these as "site-specific" models because their performance depends heavily on the accuracy of the parameters evaluated for each site.

By combining the idea of evaluating the blockage condition individually for each s from the AF model and the two-slope modeling approach in the WMED model, we constructed *model A-I*:

$$EPL(s) = \begin{cases} d_f(s) \cdot L_1 \ , & \text{if } 0 \leqslant d_f(s) \leqslant D_f \\ D_f L_1 + [d_f(s) - D_f]\, L_2 \ , & \text{if } d_f(s) > D_f \end{cases}$$

where $d_f(s)$ is the foliage depth in meters at s, L_1 and L_2 are two constants for adjusting the extra loss in dB caused by each meter of foliage, and D_f is the boundary determining

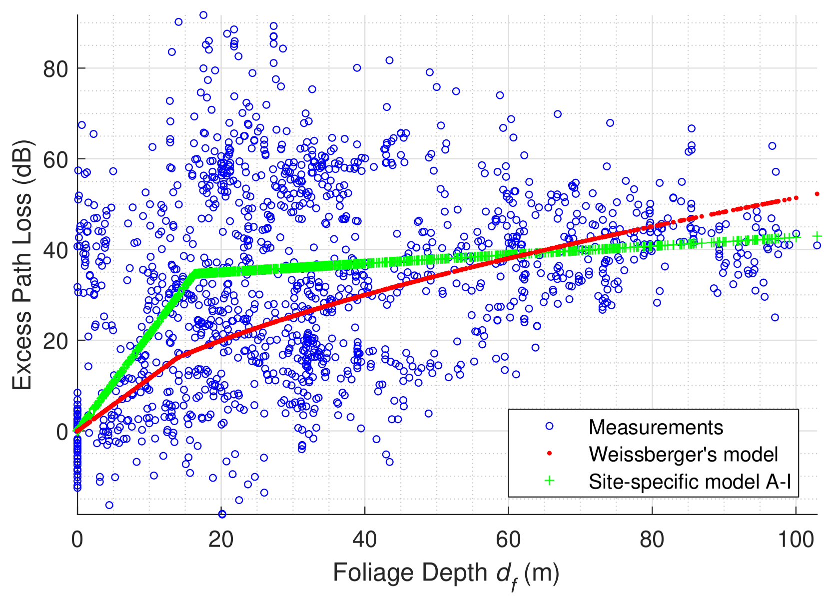

(a) Results from Weissberger's model

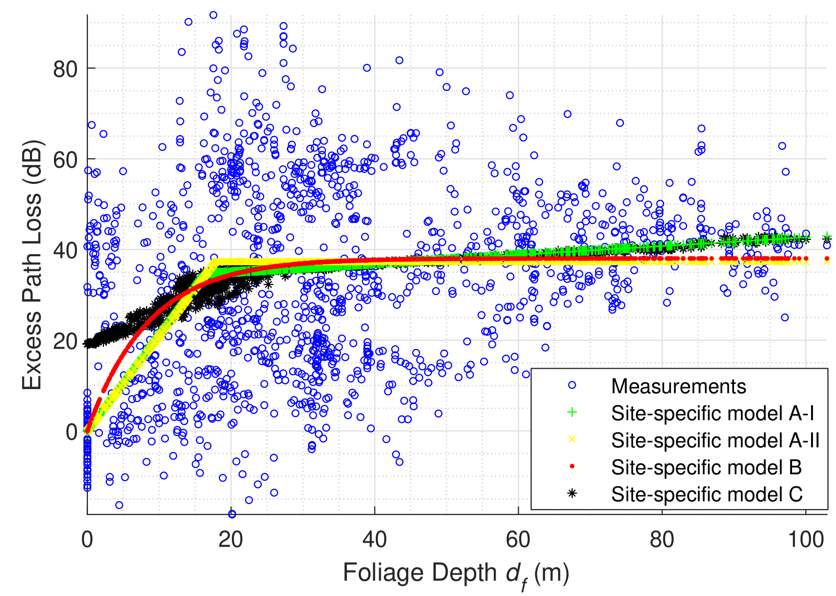

(b) Results from site-specific models

Figure 4.4. Predictions from foliage-depth-based models.

when L_2 will take effect. The upper bound from the ITU model can be imposed by setting $L_2 = 0$ to form *model A-II*:

$$EPL(s) = \begin{cases} d_f(s) \cdot L_1 \text{ , if } 0 \leqslant d_f(s) \leqslant D_f \\ D_f \cdot L_1 \quad \text{ , if } d_f(s) > D_f \end{cases}$$

We also reused the ITU model in Equation (4.1) with site-specific foliage depth to form *model B*. That is, $d_f(s)$ is used instead of $d_w(s)$, and parameters A_m and γ are set according to the measurements.

For a fair performance comparison for these three models, we used the WMED boundary $D_f = 14$ for *model A-I* to leave only two adjustable parameters. After fitting these models to our data, we found $L_1 \approx 2.39$ dB/m and $L_2 \approx 0.12$ dB/m for *model A-I*, $L_1 \approx 2.09$ dB/m and $D_f \approx 17.87$ m for *model A-II*, along with $A_m \approx 38.04$ dB and $\gamma \approx 4.47$ dB/m for *model B*. The resulting predictions are plotted in Figure 4.4b. The corresponding RMSE values are summarized in Table 4.1, together with those for the traditional models as references. Note that the site-specific models perform very similarly, and each unit of foliage depth tends to contribute less to the excess loss as foliage depth grows. *Model A-I* does not limit the excess loss as the other two site-specific models do, but it performs slightly better than *model A-II* in terms of RMSE. Overall, *model B* performs the best, but computationally, it is more demanding because of its exponential form.

We can further push the best RMSE performance to 19.18 dB with *Model C*:

$$EPL(s) = \begin{cases} 0 \text{ ,} & \text{if } a_f(s) = 0 \\ a_f(s) \cdot L_1 + L_0 \text{ ,} & \text{if } 0 < a_f(s) \leqslant A_f \\ A_f L_1 + [a_f(s) - A_f]\, L_2 \text{ ,} & \text{if } a_f(s) > A_f \end{cases}$$

where foliage area $a_f(s)$ is the sum total area for the intersections between the first Fresnel zone at RX location s and the foliage regions; L_0 (dB), L_1 (dB/m^2), and L_2 (dB/m^2) are constants adjusting the excess loss contribution; and A_f is the boundary determining when the foliage is deep enough for L_2 to take effect. According to our measurement results, we

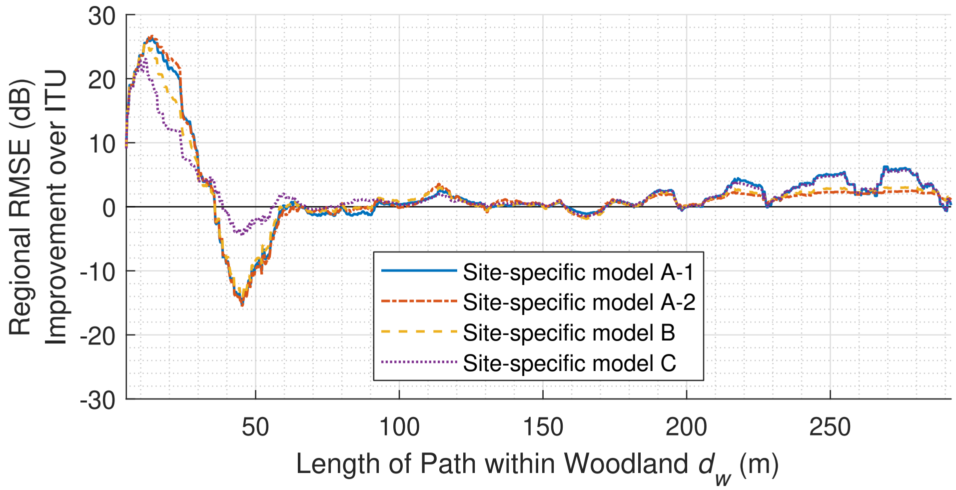

(a) Regional RMSE improvement over the ITU model

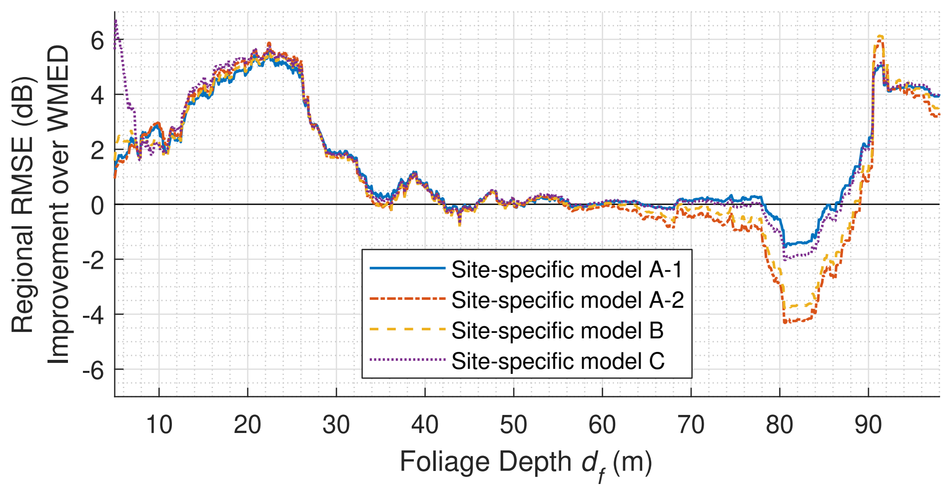

(b) Regional RMSE improvement over the WMED model

Figure 4.5. Regional performance improvement for site-specific models using a window size of 10 m.

have $L_0 \approx 19.14$ dB, $L_1 \approx 2.09$ dB/m^2, $L_2 \approx 0.06$ dB/m^2, and $A_f \approx 18.02$ m^2. This model has a sudden jump at the origin. Its prediction results are also shown in Figure 4.4b for reference.

The most important feature of these models is that they are fully automatic and thus can be applied in large-scale wireless communication networks. Site-specific information was fetched from Google and USGS servers. Foliage information was extracted, and channel modeling performed, by our automated algorithms. Another advantage of our site-specific models is their consistently good performance throughout the whole dataset. To demonstrate

Table 4.1. Overall Performance

	Baseline	**Traditional**			**Site-Specific**			
Model	FSPL	AF	ITU	WMED	*A-I*	*A-II*	*B*	*C*
RMSE (dB)	39.43	27.96	20.08	22.19	19.96	20.02	19.93	19.18

this, regional RMSE improvements over the ITU and WMED models are evaluated in terms of d_w and d_f, respectively, as summarized in Figure 4.5. For our dataset, the ITU model works very well, as shown in Table 4.1. However, according to Figure 4.5a, the ITU model suffers from an RMSE degradation of as much as 20 dB compared with the site-specific models in the low-vegetation-coverage region ($d_w < 30$ m). For large d_w, this value is observed to be as much as 6 dB. Compared with the ITU model, site-specific models work significantly better for locations close to the TX and reasonably better for those far away. However, models *A-I*, *A-II*, and *B* suffer a severe performance degradation for $d_w \in [35, 60]$ m, which is less of an issue for *model C*. A visual comparison for predictions from the ITU model and *model A-I* is provided in Figure 4.3, where *model A-I* clearly works better for extreme cases at the low and high ends of d_w. Similar comparisons have been carried out for the WMED model in Figure 4.4a and Figure 4.5b. The WMED model slightly underestimates the path loss at RX locations with a small d_f and overestimates it at large d_f. Compared with the WMED model, site-specific models again work reasonably better for extreme cases. A performance deterioration is observed at a foliage depth of around 80 m, where models *A-I* and *C* are less influenced.

4.4 Conclusion

A comprehensive channel model comparison for attenuation through vegetation was conducted using data from measurements in a coniferous forest near Boulder, Colorado. The partition-dependent AF model is intuitive and site-specific but hard to automate with satisfying performance. The ITU obstruction by woodland model and Weissberger's model work extremely well overall, but only for scenarios with a moderate amount of foliage blockage. Inspired by the results, we developed novel site-specific models for consistent improvement in prediction accuracy through shallow to deep vegetation blockages. They are fully automatic, easy to implement, and feasibly applicable to machine learning frameworks.

5. LARGE-SCALE CELLULAR COVERAGE ANALYSES FOR UAV DATA RELAY VIA CHANNEL MODELING

Reprinted, with permissions, from: Y. Zhang, T. Arakawa, J. V. Krogmeier, *et al.*, "Large-scale cellular coverage analyses for UAV data relay via channel modeling," in *ICC 2020 - 2020 IEEE International Conference on Communications (ICC)*, IEEE, Jun. 2020, pp. 1–6. DOI: 10.1109/icc40277.2020.9149403. © 2020 IEEE. Editorial changes have been made to meet Purdue's requirements on the dissertation.

5.1 Introduction

The rapid development of unmanned aerial vehicle (UAV) technologies has provided a vast array of new possibilities for wireless communications [98]. In particular, consumer-grade drones debuted around a decade ago and have become increasingly sophisticated for a lower cost. These drones have demonstrated the ability to dramatically alter several industries [99]. Boosted by advanced technologies, such as energy-efficient autonomous target tracking [100], the popularity of drones has made it possible and cost-effective to extend wireless communication coverage via UAV data relay (also called data ferrying), especially for rural areas where network coverage is sparse or nonexistent [101]. The flexibility of UAV-aided wireless communication has attracted research attention from a variety of areas, including the Internet of Things [102], intelligent transportation systems [103], and digital agriculture [104]. On-demand deployment of relay UAVs could play a key role in improving mobile service quality in many challenging scenarios faced by today's communication infrastructure. Most current research efforts, however, focus on modeling and theoretically optimizing data relay systems via UAV trajectories in simplified geographic environments [105]–[107], while deploying UAVs in practical wireless communication networks requires large-scale quantitative performance analysis results based on real-life environment information.

To fill this research gap, we propose algorithms for generating large-scale blockage and path loss maps via terrain-based channel modeling for cellular communication systems with fixed-height relay drones. Novel procedures for computing and visualizing the coverage ratio gain based on these maps are also set up to quantify system-level performance in an equipment-independent manner. Based on high-resolution LiDAR data, the blockage maps are used to locate regions with line-of-sight (LoS) obstruction and identify areas that may benefit from utilizing UAV data relay. Simultaneously, path loss maps generated from terrain elevation data enable us to identify regions with satisfactory coverage conditions and quantify the overall system performance. These algorithms were applied to Tippecanoe County, Indiana, with relay drones simulated at different heights to obtain the overall coverage gains of implementing UAV-aided cellular communication systems. Furthermore, we were able to extend the area of interest to include ten counties [108] in the Wabash Heartland Innovation Network (WHIN), Indiana, for carrying out similar cellular coverage analyses. A significant coverage ratio gain of over 40% can be achieved for both cases at a drone height of 100 m. Regions that would benefit the most were also revealed by the resulting maps. These site-specific analyses are important for quantifying the possible improvement from UAV data relay and guiding the implementation of such systems.

Our work makes the following contributions: (i) it provides quantitative analyses for UAV data relay at system level over a large geographic area based on real-life environment data, (ii) blockage detection is computed using publicly available LiDAR data as an effective alternative to full propagation simulation, and (iii) the coverage ratio gain over different path loss values is introduced to link the benefit of UAV data relay systems to quality-of-service metrics. The paper is organized as follows. In Section 5.2, we present our algorithms for generating blockage and path loss maps. Coverage analyses based on these maps are described in Section 5.3. Finally, in Section 5.5, we conclude the paper.

5.2 Terrain-Based Channel Modeling

5.2.1 Scenario Model

Consider the scenario illustrated in Figure 5.1. An agricultural end user is operating in a region with sparse coverage. A dedicated UAV follows the user at a constant height above ground h_D to act as a relay between the user and remote cell towers serving the area of interest. The communication between the UAV and the user is assumed to be reliably taken care of by wireless local area network (WLAN) technology. This is a possible application in digital agriculture where the relay UAV provides extended communication links in rural areas for the user via a cellular backhaul. The relay UAV's presence allows the cell tower to reach some areas blocked at the user level. We are interested in modeling this improvement quantitatively at a large geographic scale for different values of h_D using freely available geographic information such as LiDAR and terrain elevation data.

Such a data relay system can be implemented at low cost by attaching a custom-configured cell phone to a modern photography drone with autonomous target tracking functionality. Compared to enhancing coverage via a vast number of traditional repeaters or small cell systems, the data relay approach provides the flexibility to enable inexpensive on-demand deployment of wireless communication infrastructure. The relay UAVs can be dispatched from the mobile service providers or set up privately by users. When they are no longer needed, they can be dismissed. This flexibility is the key to satisfy the intermittent connectivity requirement over vast low-population areas in many digital agriculture applications. In particular, data relay would be most useful for scheduled sensor data collection or temporary data transmission during short-term activities such as planting and harvesting. Such systems could operate without the high cost of building out and maintaining traditional fixed infrastructure.

5.2.2 Simulation Scene Construction

The simulation was carried out primarily in the Universal Transverse Mercator (UTM) coordinate system. Conversions between UTM (x, y) and GPS $(latitude, longitude)$ were

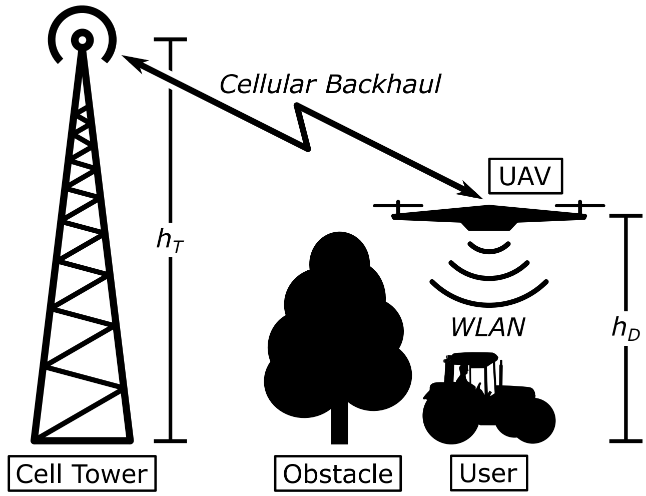

Figure 5.1. Illustration of a typical UAV data relay scenario.

performed when necessary with a fixed UTM zone label *16T*. To incorporate the height dimension over a large geographic area, the UTM system is extended with *altitude*, the sum of the ground *elevation*, and the object height. The information needed for constructing the simulation scene includes the cell tower antenna locations and the drone locations to inspect. Our simulator, together with the coverage analysis algorithms, were implemented[1] using MATLAB R2019b.

Locating Effective Cell Towers

Cell tower GPS locations were obtained from a randomized U.S. cellular laydown used in a National Telecommunications and Information Administration (NTIA) analysis for Advanced Wireless Services (AWS)-3 spectrum sharing. This dataset contains real-life cell tower locations with randomized errors of a scale of a few kilometers for security and privacy concerns. To reduce the number of cell towers considered in the simulation, we extended the area of interest by an estimated maximum cell tower coverage radius and only considered towers within that range, as illustrated in Figure 5.2. Cell towers out of the extended area were considered ineffective and ignored in the corresponding simulation. For simplicity, the

[1]↑Source code publicly available at https://github.com/YaguangZhang/CellCoverageMapperForDronesMatlabWorkspace.git

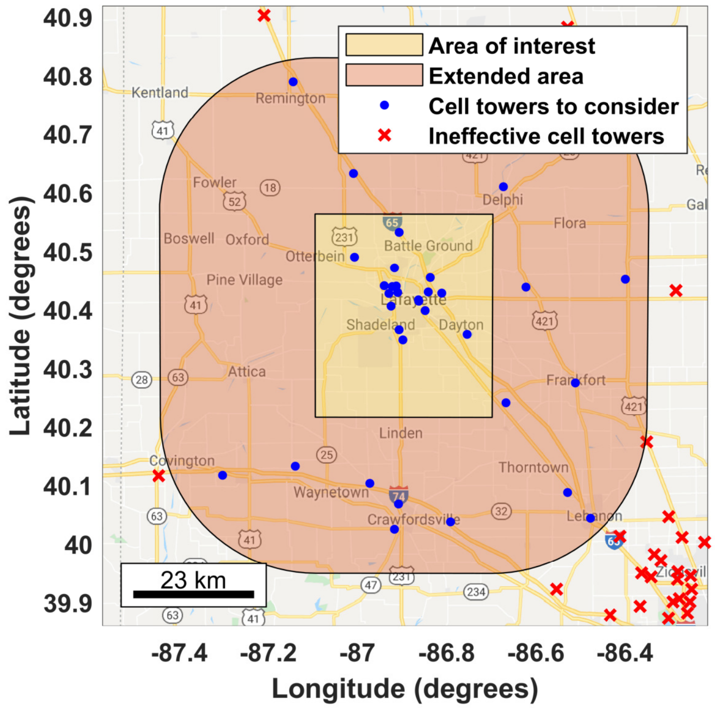

(a)

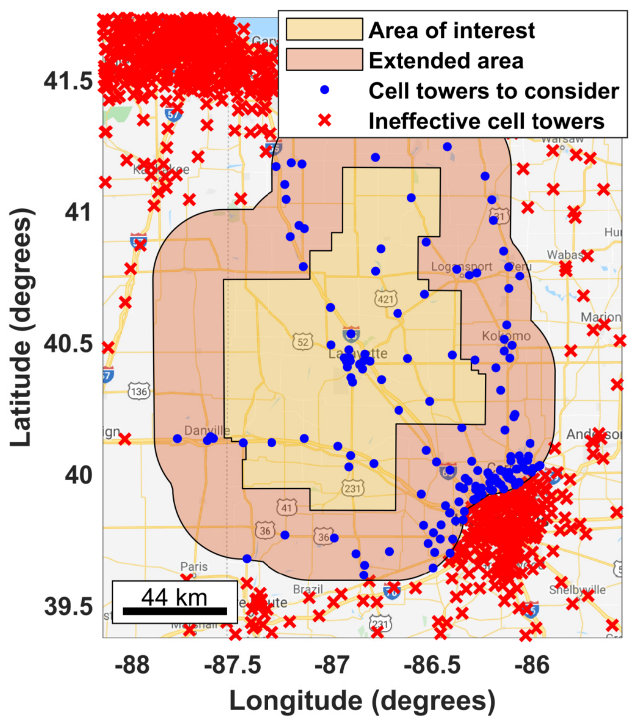

(b)

Figure 5.2. Area of interest and cell tower locations for (a) Tippecanoe County and (b) WHIN region.

maximum coverage radius R_{Max} in kilometer was estimated as the longest optical horizon distance from the cell tower antenna:

$$R_{Max} \approx 3.57 \times \left(\sqrt{h_T} + \sqrt{h_D} \right), \tag{5.1}$$

where h_T and h_D are the heights in meters for the cell tower antenna and the drone, respectively. The antenna heights for all cell towers were set to be a typical value of 50 m in the simulation. For R_{Max}, we set $h_D = 1.5$ m, the lowest drone height inspected, which gave us $R_{Max} \approx 29.6$ km.

UAV Location Grid Construction

A grid for the UAV locations covering the area of interest was built for each simulation, as shown in Figure 5.3. These locations are sampled evenly within the area of interest. Its spatial resolution is determined by the number of grid points N_{Samp} for the longer side (width or height) of the area of interest. We had $N_{Samp} = 100$ (over 38.5 km) for Tippecanoe County and, to compensate the extra cell towers to consider, $N_{Samp} = 50$ (over 144.8 km) for the WHIN area. This results in an 8700-point grid with a spatial resolution of around 0.4 km for Tippecanoe County and a 1249-point grid with a spatial resolution of around 2.9 km for the WHIN area.

5.2.3 Blockage Map Generation

Blockage maps visualize locations with no clear LoS connection to any cell tower. Figure 5.4 illustrates six examples. Examining the figures, we observe that the blocked region shrinks dramatically as we increase the drone height from 1.5 m to 100 m. Intuitively this makes sense, as higher altitude drones will more likely be operating above natural and man-made obstructions.

To determine blocked links, the Indiana 5-feet-resolution (approximately 1.52-meter-resolution) LiDAR dataset [109] was utilized in locating obstructions. At a given position, the LiDAR z value (relative to the sea level) was interpreted as the altitude of the top of the obstacle at that position. To improve accuracy, rather than determining blockage of

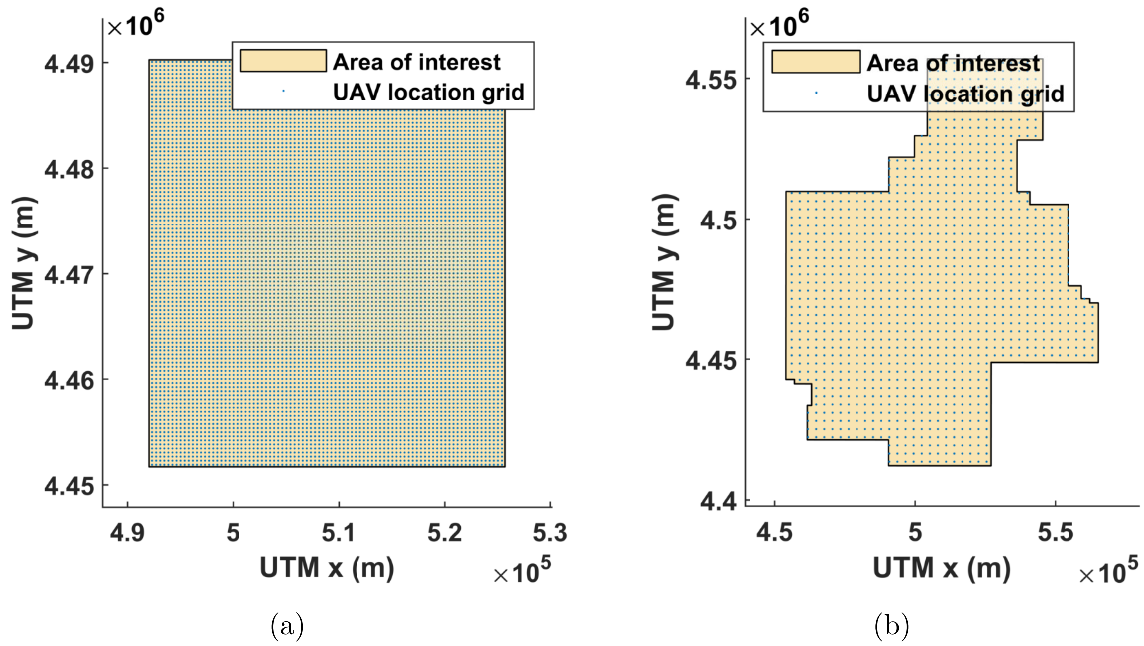

Figure 5.3. The UAV locations to be inspected for (a) Tippecanoe County and (b) WHIN region.

the direct path between a transmitter (TX) and a receiver (RX), we incorporated clearance tests for the first Fresnel zone. The first Fresnel zone provides a 3-dimensional (3D) ellipsoid surrounding the direct path; obstacles present in this zone will negatively influence the communication link. The radius of the first Fresnel zone $R_F(P)$ at any point P in between the endpoints of the link is given by [110]:

$$R_F(P) = \sqrt{\frac{\lambda d_1 d_2}{d_1 + d_2}}, \quad d_1, d_2 \gg \lambda, \tag{5.2}$$

where d_1 is the distance of P from one end, d_2 is the distance of P from the other end, and $\lambda = c/f_C$ is the wavelength of the transmitted signal (c is the speed of light). In the simulation, we set the signal carrier frequency $f_C = 1.9$ GHz to mimic a 4G Long-Term Evolution (LTE) system operating in the Personal Communications Service band. For computing blockage, a threshold of 60% clearance in the first Fresnel zone was set, as shown in Figure 5.5. That is, 60% of the first Fresnel zone radius, $R_F(P)$, around the direct path should be clear of any obstacles. This value is the minimum value required for reliable wireless communication links [111].

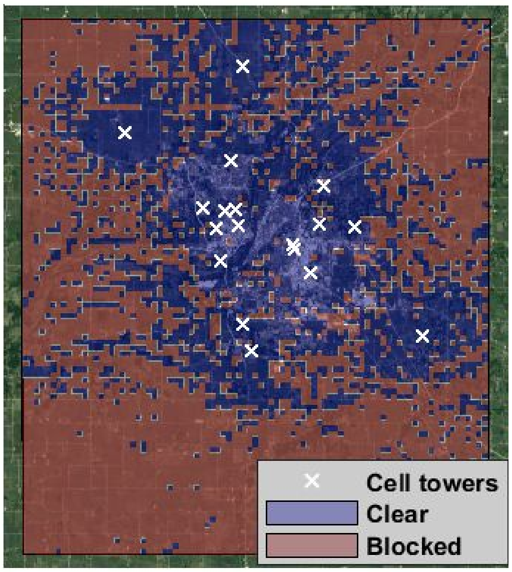

(a) Tippecanoe, $h_D = 1.5$ m

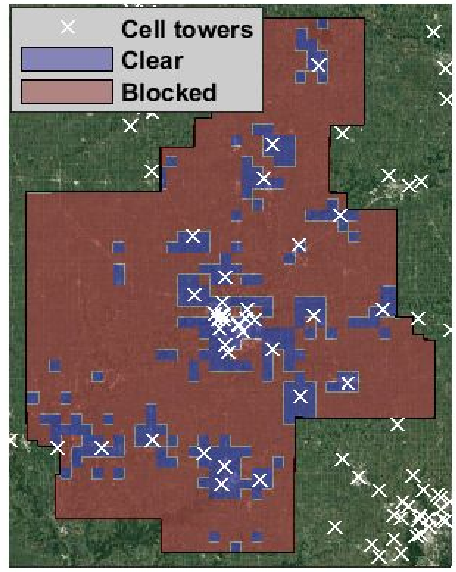

(b) WHIN, $h_D = 1.5$ m

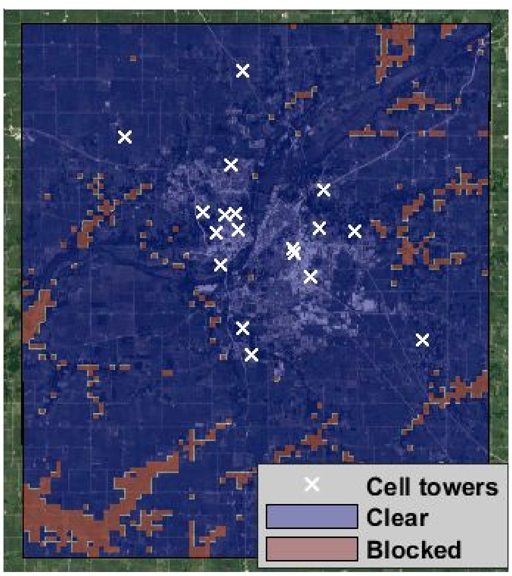

(c) Tippecanoe, $h_D = 10$ m

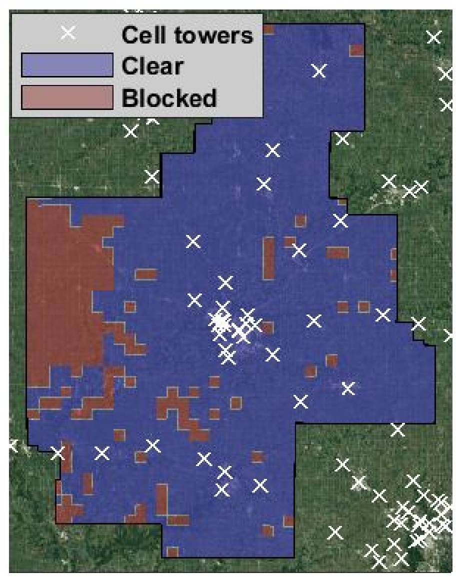

(d) WHIN, $h_D = 10$ m

Figure 5.4. Example blockage maps for Tippecanoe County and the WHIN area, with different drone heights (h_D).

Figure 5.4. Continued.

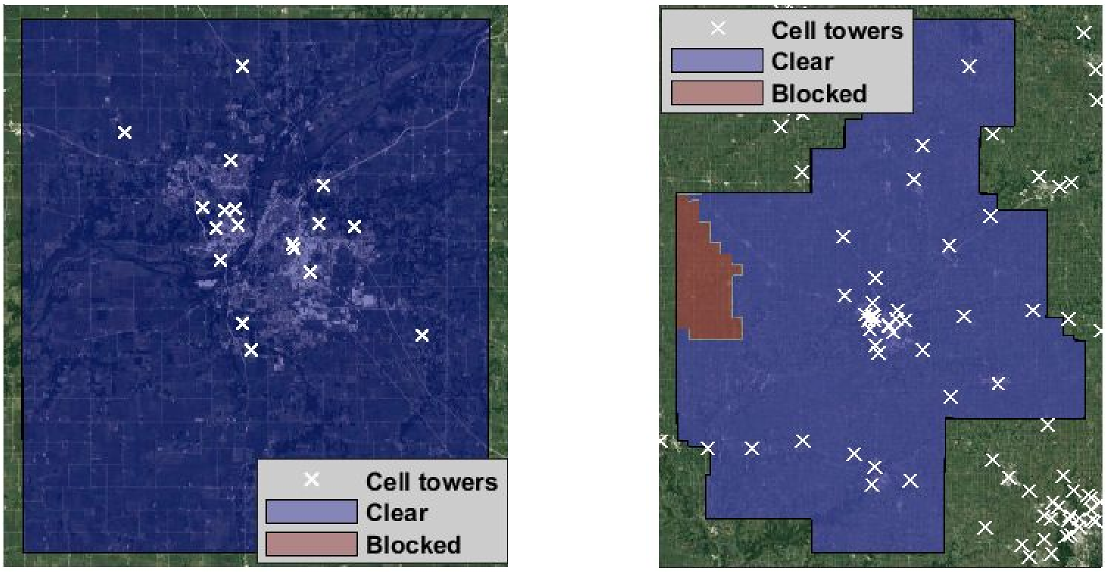

(e) Tippecanoe, $h_D = 100$ m

(f) WHIN, $h_D = 100$ m

To make large-scale analyses feasible, the clearance test was conducted in a 2-dimensional (2D) vertical plane that contained the path connecting the cell tower antenna and the drone. In this approach, the first Fresnel zone becomes an ellipse, as illustrated in Figure 5.5. An obstacle profile between the effective cell tower and the drone location is generated primarily from interpolating locally cached LiDAR and terrain elevation data for Indiana, as shown in the top view. Then, the 60% clearance test for the first Fresnel zone is carried out in the front view. In this example, the LiDAR sample for the rightmost tree indicates the LoS link is disrupted.

More specifically, to generate the blockage map, we constructed a 2D obstacle profile based on the LiDAR data for each effective cell tower antenna with each drone location in its R_{Max} range. For example, Figure 5.5 illustrates the link between an effective cell tower (indicated by the cross mark) in WHIN and a nearby drone location to inspect (indicated by the solid circle). The top view also shows in dark grey the LiDAR data tiles, covering the whole State of Indiana. The obstacle profile is generated by extracting a 2D vertical profile of LiDAR z values along with the link of interest via bilinear interpolation. When the effective cell tower is located out of Indiana, we fall back to the United States Geological

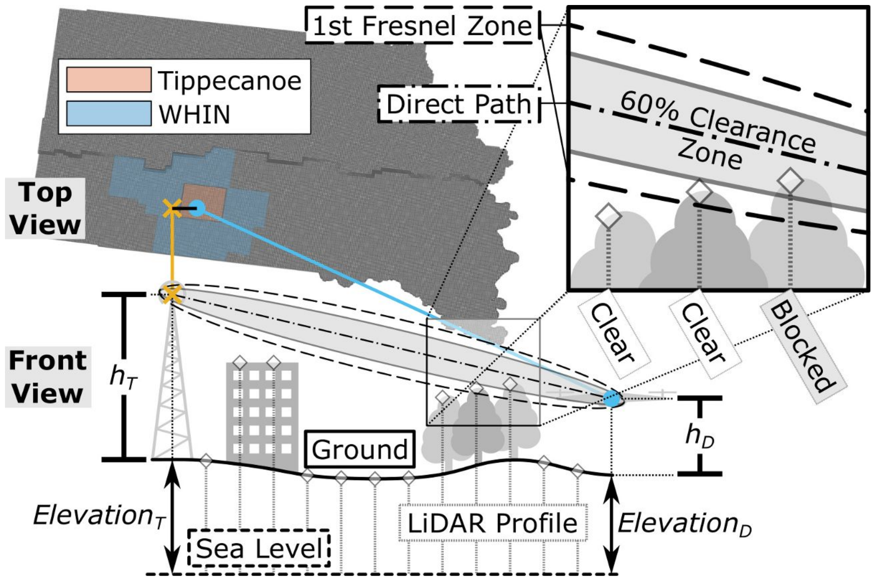

Figure 5.5. Illustration of the LoS path clearance test.

Survey (USGS) 1/3rd arc-second terrain elevation data for the vertical profile values. The number of profile samples is set to be the minimum integer bigger than or equal to 10 that guarantees a spatial resolution smaller than or equal to 50 m. An obstacle LiDAR profile with this relatively large resolution may miss small-scale obstructions such as single trees but is necessary to ensure a reasonable time to perform simulations over such large geographic areas. Both the LiDAR data and the elevation data were cached locally for the whole State of Indiana to further boost the simulation speed.

Once the profile has been extracted, the direct LoS path can be determined by the 3D coordinates UTM (x, y) and *altitude* of the cell tower antenna and the drone position. If any of the obstacle LiDAR profile values are on or higher than the direct path, the LoS link is considered blocked. Otherwise, we will carry out the 60% clearance test for the first Fresnel zone demonstrated in Figure 5.5. For each obstacle LiDAR profile point, we locate the corresponding P by intersecting the direct path with its perpendicular line which goes through that profile point. The LoS link is blocked if the distance from the profile point to the direct path is smaller than or equal to $0.6R_F(P)$. If the direct paths between the inspected drone location and all the effective cell towers are blocked, that location will be marked as "blocked" in the corresponding blockage map. This procedure helps improve the speed of the simulator by reducing the number of Fresnel zone calculations.

5.2.4 Path Loss Map Generation

The path loss maps are generated similarly to the blockage maps. However, instead of blockage indicators, they store at each drone location the best (minimum) available path loss for the links between all the effective cell towers and that drone location, as plotted in Figure 5.6. In these maps, we can observe a clear decreasing trend for the path loss values as h_D is increased from 1.5 m to 100 m, implying improved communication conditions with relay UAVs.

To estimate the median basic transmission loss using terrain elevation data, we utilized the NTIA C++ implementation [112] of the extended Hata (eHata) model [113]. The eHata model extends the applicability of the Hata empirical formula for the Okumura curves to $1500\,\text{MHz} \leq f_C \leq 3000\,\text{MHz}$ with a transmitter-to-receiver (TX-to-RX) distance d between 1 km and 100 km. For $d < 1\,\text{km}$, we computed the convex combination of the eHata result $PL_{\text{e}Hata}$ and the free-space path loss PL_{FSPL} via:

$$PL_{near} = \frac{d}{1\ \text{km}} \times PL_{\text{e}Hata} + (1 - \frac{d}{1\ \text{km}}) \times PL_{FSPL}, \tag{5.3}$$

where PL_{near} is the path loss for locations near the TX. The eHata model is designed for the case when the TX's altitude is larger than the RX's, so we assumed reciprocity and treated the higher one of the cell tower antenna and the drone to be the TX. The NTIA implementation also accounts for a set of link-specific adjustments based on terrain type, terrain elevation profiles, and endpoint clutter category. For simplicity, a fixed National Land Cover Database environment code of 82 (cultivated crops) was chosen in our simulator, representing a rural type environment. The elevation profiles were generated in the same manner as the obstacle LiDAR profiles.

One advantage of considering path loss via channel modeling for large-scale coverage analyses is that the results are independent of equipment or wireless standard. With the huge range of devices at both the cell tower and the user sides, it is practically difficult to

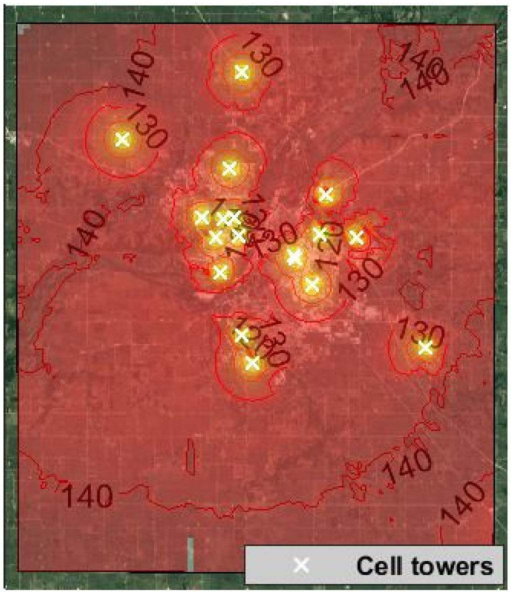

(a) Tippecanoe, $h_D = 1.5$ m

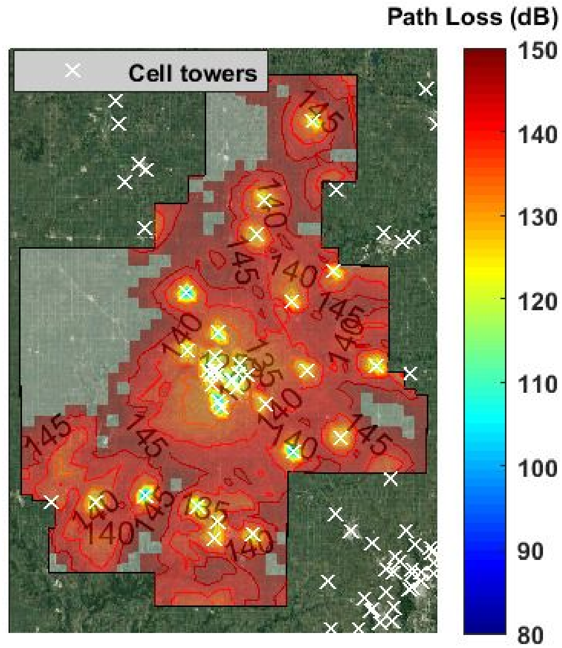

(b) WHIN, $h_D = 1.5$ m

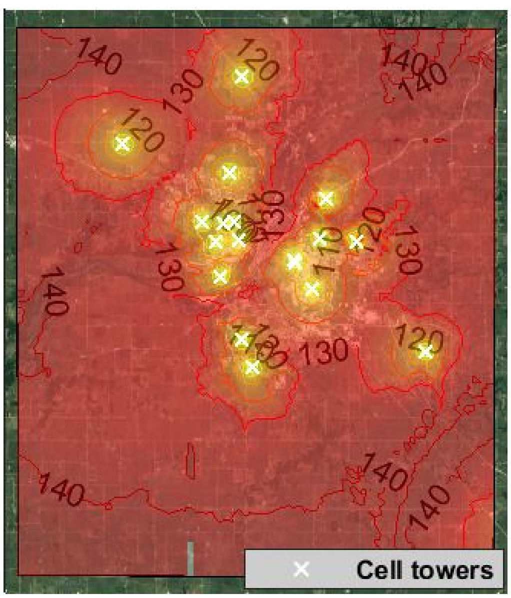

(c) Tippecanoe, $h_D = 10$ m

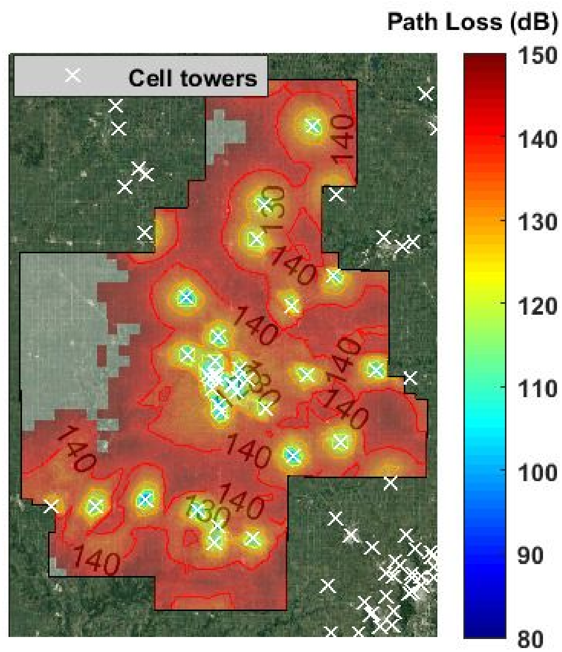

(d) WHIN, $h_D = 10$ m

Figure 5.6. Example path loss maps for Tippecanoe County and the WHIN area, with different drone heights (h_D).

Figure 5.6. Continued.

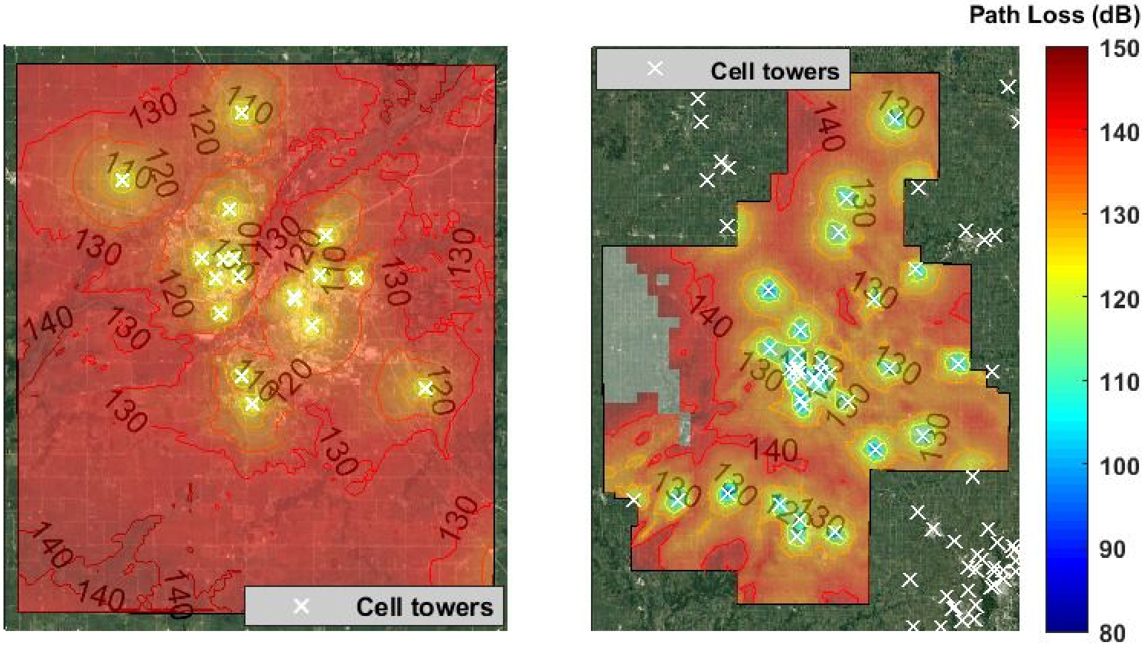

(e) Tippecanoe, $h_D = 100$ m

(f) WHIN, $h_D = 100$ m

collect the specifications for all installations involved over a large geographic area. Being the unavoidable major signal degradation contributor, path loss provides a fair coverage analysis without that information. However, the path loss values do not directly translate to a link quality indicator such as data rate; therefore it is necessary to compute link budgets with typical parameter values to form a connection between the path loss maps in the cellular coverage scenario and system-level key performance indicators. According to [114], for the downlink of a 4G LTE Frequency Division Duplex system, a user terminal typically has a noise figure of $NF_U = 9$ dB. With a bandwidth $B = 10$ MHz, the minimum detectable signal strength $MD_{DL} \approx -95$ dBm is given by:

$$MD_{DL} = 10 \log_{10} \left(\frac{kT}{1\text{mW}} \right) + NF_U + 10 \log_{10} B, \tag{5.4}$$

where k is the Boltzmann's constant and $T = 290$ K is the device temperature. Taking into account the typical cell tower antenna power $P_T = 64$ dBm, we have the maximum allowed path loss for the downlink $PL_{DL} \approx 177$ dB via:

$$PL_{DL} = P_T + G_T + G_U - MD_{DL}, \tag{5.5}$$

where $G_T = 18$ dBi and $G_U = 0$ dBi are the typical maximum antenna gains for the cell tower and the user terminal. Similarly, we can get the maximum allowed path loss for the uplink $PL_{UL} \approx 140$ dB, with the user terminal TX power $P_U = 23$ dBm and the noise figure for the cell tower $NF_T = 5$ dB. Note that the 140 dB PL_{UL} effectively sets the maximum coverage area for cellular communications. Thus, for the path loss maps, we set a threshold of $PL_{Max} = 150$ dB as the maximum allowed path loss value and discard any results above that. If the drone location does not have a lower or equal path loss value for any links originating from all the considered cell towers, the corresponding grid cell is considered out of service and will not be colored on the map, as shown in Figure 5.6. Examining the figure, we observe very poor coverage on the west side of WHIN because of a lack of cellular towers in that region. It is also worth noting that 140 dB of PL_{UL} is the typical worst uplink path loss for detecting the signal, which will not support high data rates or quality of service. One could leave a wriggle room of about 10 dB for acceptable service quality, yielding a desired path loss value of 130 dB as reference.

5.3 Coverage Analyses

Both the blockage and path loss maps in Figure 5.4 and Figure 5.6 visually demonstrate promising cellular coverage improvement via data relay UAVs. Furthermore, we can obtain quantified results in terms of coverage area improvement from these maps. Figure 5.7 presents the LoS coverage ratio, the ratio of the size for the clear region on the blockage map to the total size of the area of interest, at different UAV heights for Tippecanoe County and WHIN. For Tippecanoe County, a dramatic coverage gain over $90\% - 40\% = 50\%$ can be obtained by deploying UAV at $h_D = 10$ m, compared to a typical user terminal height of 1.5 m. For WHIN, that gain boosts to over 60%. Increasing the relay UAV beyond 10 m

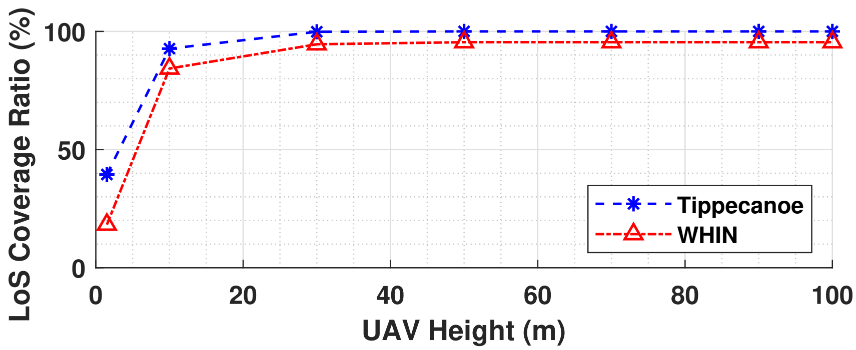

Figure 5.7. Clear LoS area percentage values based on blockage maps for the Tippecanoe County and the WHIN region.

will further improve the LoS coverage, but with only an extra gain of around 10% for both cases.

Figure 5.8 summarizes the path loss maps for all the UAV heights evaluated using the empirical cumulative distribution functions (CDFs) of the path loss values stored in these maps. With a given maximum allowed path loss value, we can find in these plots the corresponding coverage ratios for the UAV heights inspected. Because each path loss value represents a grid cell of a constant size on the corresponding map, the ratio of the path loss values smaller than or equal to a maximum allowed path loss PL_{Max} is the same as the coverage ratio for PL_{Max} in terms of area. That is, given PL_{Max}, we can directly use the empirical CDF values read from Figure 5.8 as coverage ratios. For example, with $PL_{Max} = PL_{UL} = 140$ dB, we can get the coverage ratio for Tippecanoe County is around 75% at $h_D = 1.5$ m and around 95% at $h_D = 100$ m, yielding an improvement of $(0.95 - 0.75)/0.75 \approx 27\%$. Similarly, with $PL_{Max} = 140$ dB, we have for WHIN a coverage ratio of around 28% at $h_D = 1.5$ m and around 80% at $h_D = 100$ m, yielding a remarkable 186% improvement. The general rising trend of the curves with increasing h_D supports the use of relay UAVs. To better demonstrate these improvements, the coverage ratio gains relative to the $h_D = 1.5$ m case are plotted in Figure 5.9. For Tippecanoe County, as we increase h_D from 10 m to 100 m, the coverage gain at $PL_{Max} = 140$ dB increases from 5% to 20%, while the whole region from 130 dB to 140 dB gets a significant boost with the highest gain of around 50% at 133.5 dB. This implies a moderate improvement for the worst acceptable coverage with

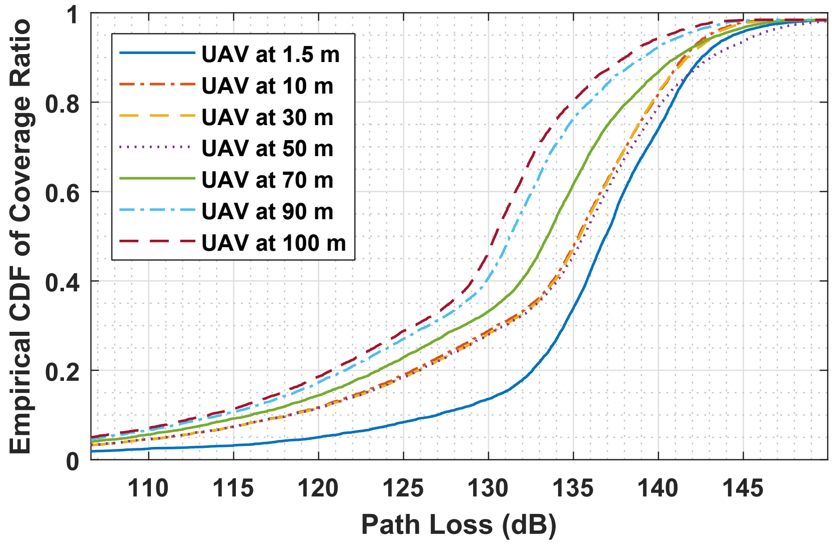

(a)

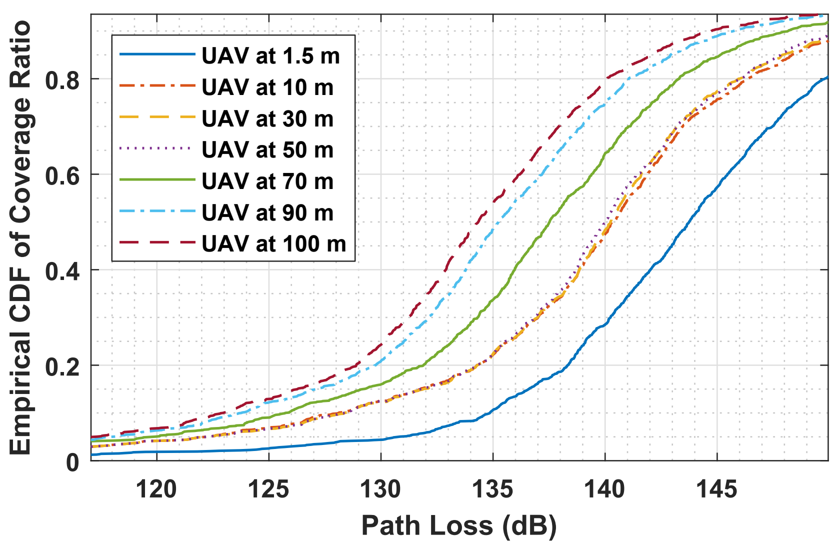

(b)

Figure 5.8. Empirical CDFs of the path loss maps for (a) the Tippecanoe County and (b) the WHIN region.

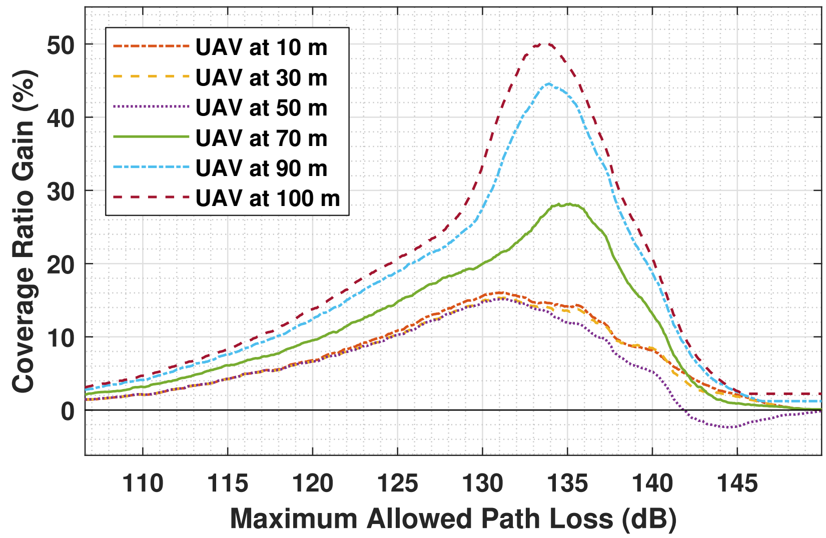

(a) Tippecanoe County

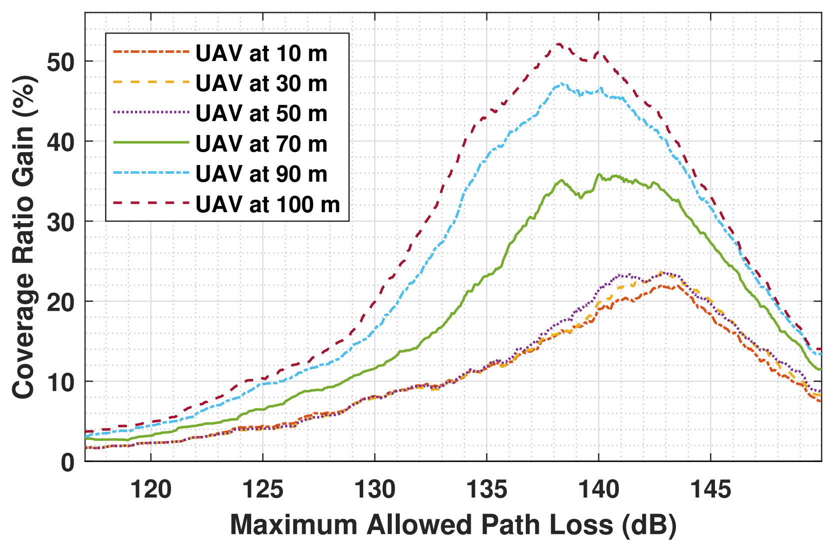

(b) WHIN

Figure 5.9. Coverage ratio gain relative to the $h_D = 1.5$ m case.

a dramatic larger area getting better service. On the other hand, the WHIN area enjoys a significant boost between 130 dB and 140 dB, particularly at the high end with a gain value from 19% to 51% as h_D increases, indicating a large area with no cellular service will get covered with relay UAVs.

5.4 Discussion

We have focused on extending LTE cellular coverage for digital agriculture applications. However, the same methodology can be applied to other systems such as future millimeter-wave systems, where the blockage maps will play a more important role because of the high sensitivity of millimeter waves to blockage [45]. With digital terrain data becoming more widely available, our coverage analysis tool will be able to quantify the benefit of utilizing relay UAVs for more areas of interest. The biggest challenge for such a tool is to speed up the computation to cope with the large geographic area considered. The bottleneck of our algorithms is the LiDAR/elevation terrain profile generation. Additionally, we applied the following techniques to speed up the simulation: reprocessed local data for indexes to enable faster search and data fetch; issued up to 100 concurrent HTTP requests for data not cached locally; reused terrain profiles for different drone heights; used parallel computing and preassigned tasks to workers to avoid frequent worker initialization. On a 36-core cluster with 216 GB RAM, the simulation for Tippecanoe County took two days, and that for WHIN took less than a week. In the future, we would like to optimize UAV deployment based on our simulations. We would also like to take real-life measurements to verify the simulation results and expand the simulation area in Indiana and to areas with more complex terrain conditions for comparison, Colorado for instance.

5.5 Conclusion

In this paper, we presented a simulator to generate blockage maps and path loss maps via channel modeling for large-scale cellular coverage analyses on UAV data relay. Both visual and quantitative results are provided for Tippecanoe County and the ten-county WHIN region. According to these results, a significant coverage gain of over 40% at a UAV height of 100 m is expected for both cases. These analyses are crucial in guiding the implementation of UAV data relay systems.

6. REVEALING DIGITAL GAP VIA STATEWIDE CELLULAR COVERAGE ANALYSES

In this chapter, we will expand the area of interest to the State of Indiana and present cellular coverage simulation results over a wide range of carrier frequencies, including the 4G Long-Term Evolution (LTE) 1.9 GHz, the 5G sub-6GHz band at 4.7 GHz, the fixed wireless 13 GHz, and 28-GHz millimeter wave (mmWave). This work is a natural extension of Chapter 5. Instead of the effects of the antenna heights on the user's side, this chapter investigates at a system level the implications of moving towards mmWave bands in wireless local area networks (WLANs).

6.1 Blockage Distance Map

With improvements in the large-scale cellular coverage simulator to reduce the computational cost, we are now able to carry out simulations at the state level. Here, a simulation is set up for the State of Indiana to obtain a map of the minimum available blockage distance between the location of interest and the cell towers. The same procedures for the blockage maps in Chapter 5 were used, but with an extra step to get the cumulative blockage distance along the direct paths. An overview of the area of interest is provided in Figure 6.1. It can be observed that the simulation area, denoted by the orange region, is smaller than the State of Indiana, bounded by the red dotted line. In a nutshell, the simulation area covers 52 348 km^2 out of the whole Indiana's land area, 94 321 km^2. That corresponds to a 55.5% coverage of the whole Indiana state. This simulation area was chosen so that, after it was expanded by the maximum coverage radius of a cell tower, the expanded area, denoted by the red region, would still be barely contained in the Indiana state. This way, all effective cell towers to consider in the simulation, represented by the blue dots, were all located in Indiana. As a result, we did not need to worry about getting the LiDAR information for locations out of Indiana.

We have in total 3975 grid points with a spatial resolution of 3.65 km covering the simulation area. The carrier frequency in this simulation was set to 1.9 GHz, a typical value

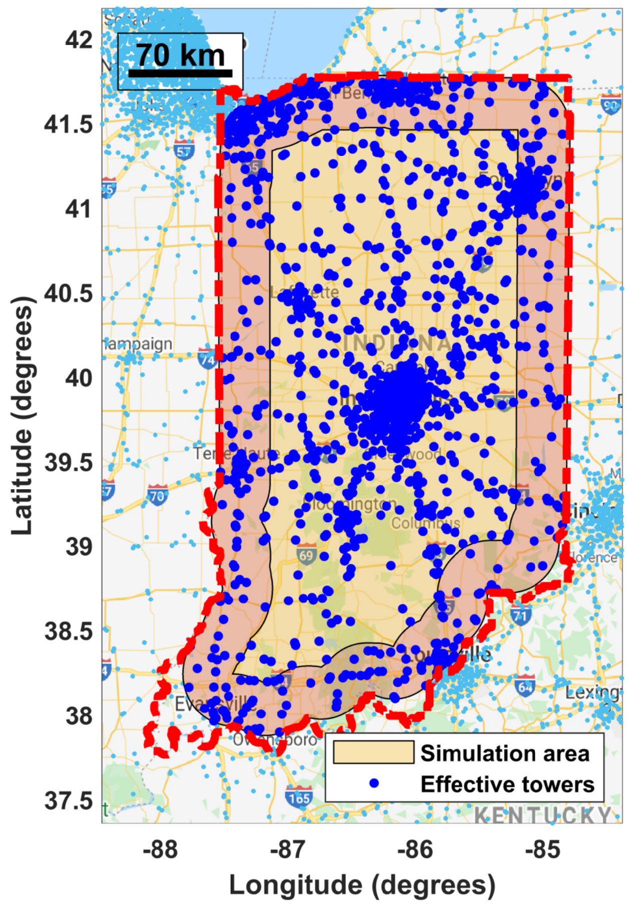

Figure 6.1. Simulation area of interest for Indiana.

for the LTE system. The Digital Surface Model from 2016–2020 Indiana statewide LiDAR data [115] was used to locate obstacles. The National Telecommunications and Information Administration (NTIA) one-carrier cell tower laydown was merged with the cellular tower location dataset from the Homeland Infrastructure Foundation-Level Data (HIFLD) Open Data program [116]. This way, the towers of small regional network operators, especially those in the rural regions, were also considered in the simulation. In other words, we assume that all the carriers share their towers for better coverage in rural areas.

Now, from the resultant blockage distance map shown in Figure 6.2, we can see that most of the locations do not have clear line-of-sight (LOS) links to any tower. The minimum cumulative blockage distance goes up to over 6000 m at some locations. In fact, as can be further observed in the empirical cumulative distribution function (CDF) plot in Figure 6.3,

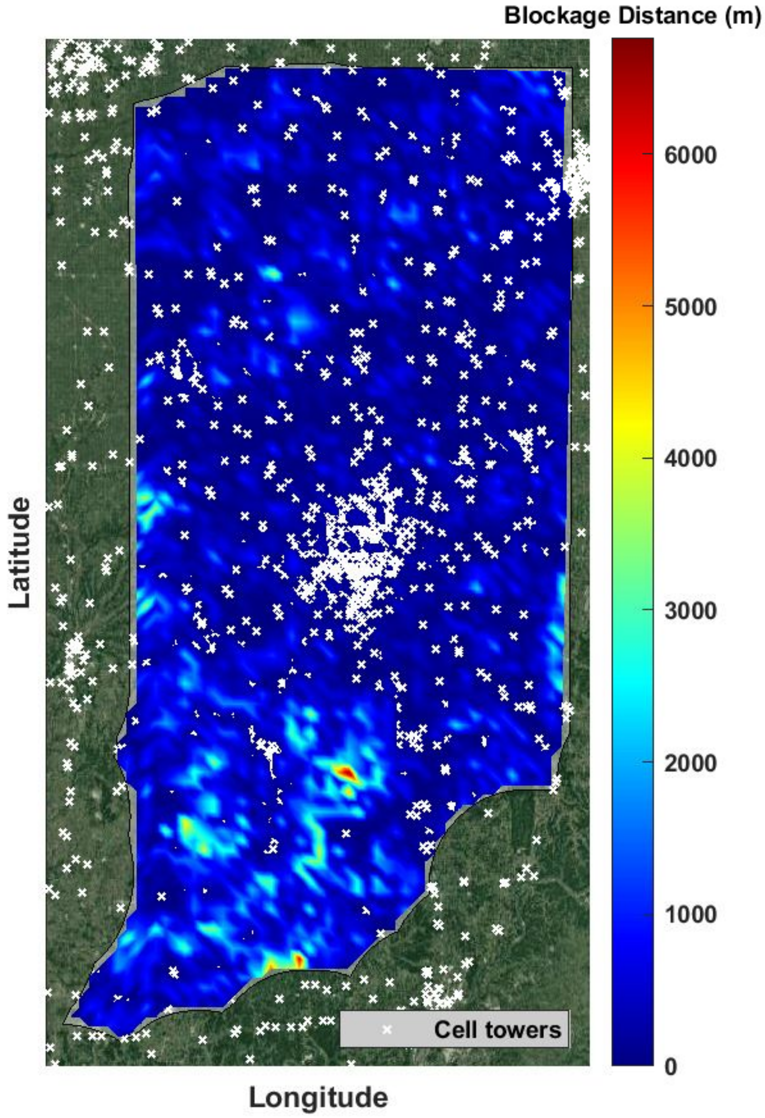

Figure 6.2. Map of the minimum available blockage distance for 1.9 GHz in Indiana.

over 80% of that region has a cumulative blockage distance over 10 meters, while around 60% of that region has a cumulative blockage distance over 100 meters. The majority of the area of interest experiences a minimum cumulative blockage distance of more than 170 m. For higher-frequency carriers, including mmWaves, this is bad news. In rural regions, there are very few buildings to cause strong reflection paths as alternative communication links to the LOS one. The blockages can easily attenuate the LOS signal to an unrecognizable state.

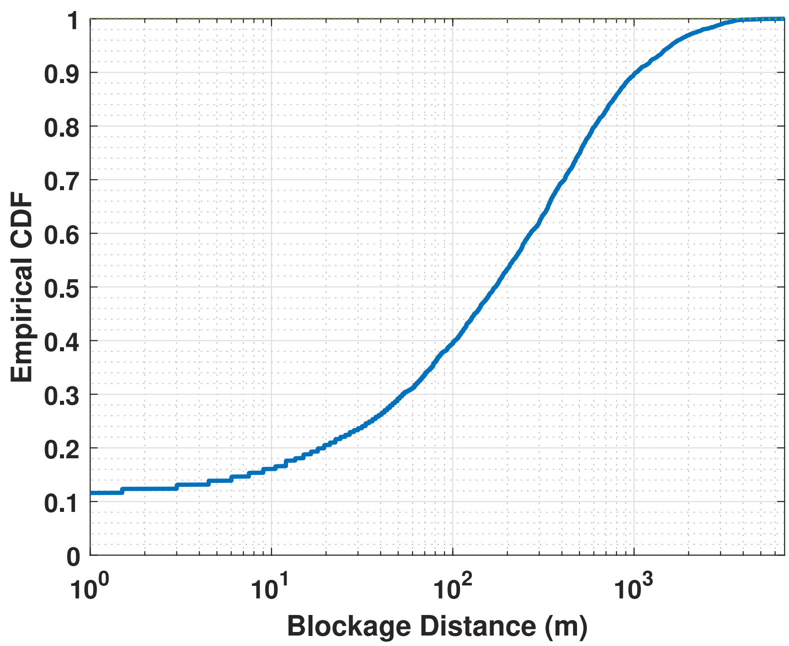

Figure 6.3. Empirical CDF of the minimum available blockage distance for 1.9 GHz in Indiana.

6.2 Path Loss Maps

We also have simulated the path loss for different frequencies, including 1900 MHz for LTE, 4700 MHz for one of the sub-6 GHz bands in the 5G cellular system, 13 GHz used in fixed wireless, and finally 28 GHz for mmWave. The path loss maps are plotted in Figure 6.4. A decreasing trend of the coverage can be clearly observed as we move closer to mmWave. So, with other conditions kept the same, moving towards higher frequency will significantly increase the difficulty of achieving ubiquitous coverage.

This is why network densification, or even ultra-densification, has been proposed. The idea is simple: if the coverage of one cell shrinks, we just need to add more cells to cover the same area. However, what people normally take for granted here is the expansion of the network. As we increase the carrier frequency to mmWave, an impractical number of new towers will be needed for ubiquitous coverage.

Table 6.1 estimates the number of new towers needed for different carrier frequencies to achieve ubiquitous coverage in the simulation area. As derived in Chapter 5, the typical maximum path loss an LTE system can endure is 140 dB. Here, we added an extra 10 dB

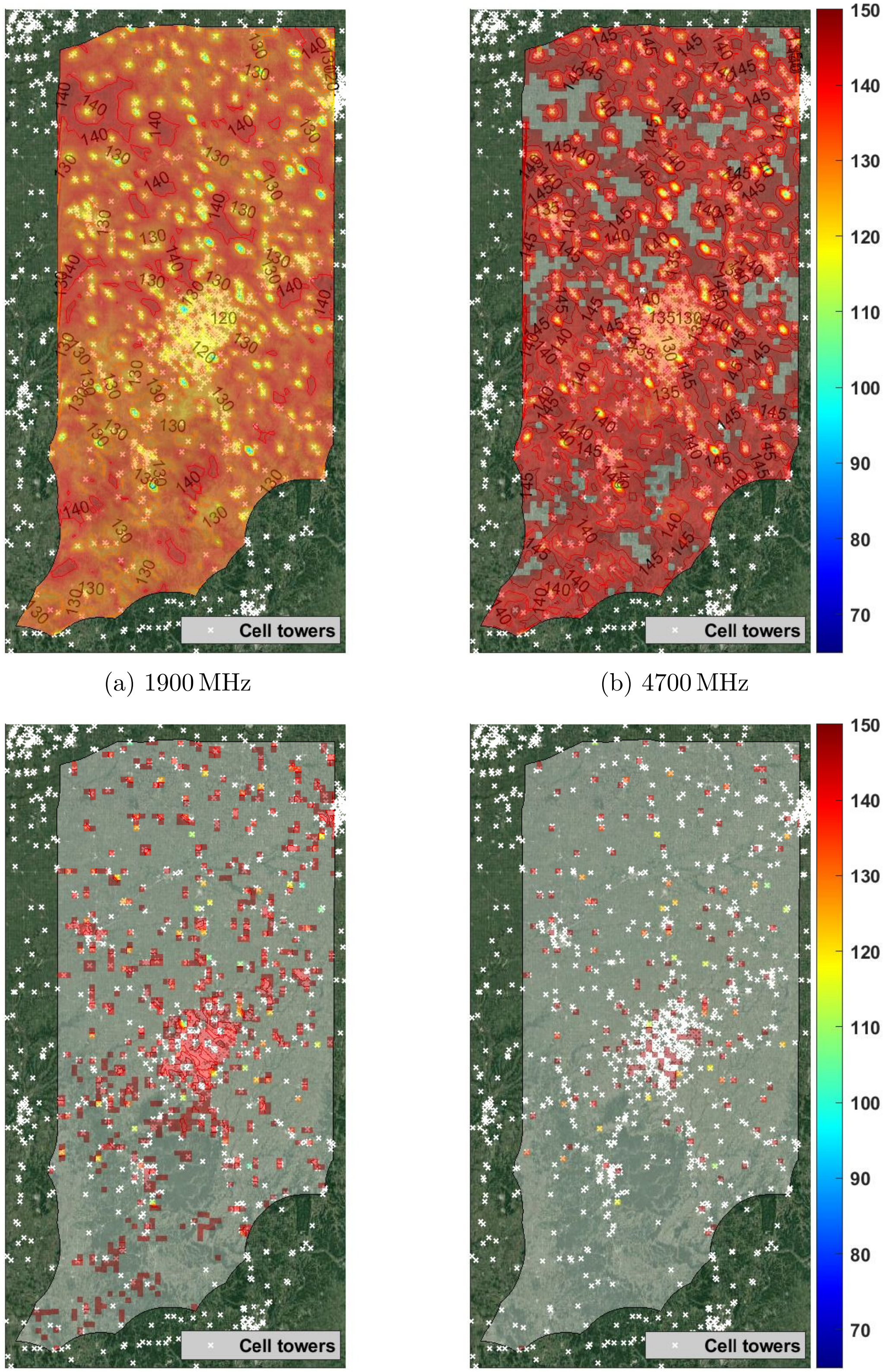

(a) 1900 MHz

(b) 4700 MHz

(c) 13 GHz

(d) 28 GHz

Figure 6.4. Path loss maps for different carrier frequencies.

Table 6.1. Estimated Numbers of New Towers Needed for Ubiquitous Coverage

Carrier Frequency (MHz)	Covered Area (km^2)	Maximum Cell Radius (km)	Maximum Cell Area (km^2)	Minimum # of New Towers Needed
1900	52,348	2.44	18.7	0
3700	51,044	1.49	7.0	187
4700	47,159	1.25	4.9	1064
7000	34,187	0.98	3.0	6029
13,000	10,312	0.86	2.3	18,062
28,000	2291	0.69	1.5	32,988

as a margin. Based on this new maximum allowed path loss value of 150 dB, the currently covered areas were simulated for the carrier frequencies of interest. Then, the maximum cell tower coverage radius was estimated in a flat terrain without any obstacles via the NTIA extended Hata (eHata) model (see Chapter 5). The maximum coverage area for one cell was computed from a circle with that radius. At last, the minimum number of new towers needed to completely cover the whole simulation area was evaluated.

As can be read from Table 6.1, with an increasing carrier frequency, the number of extra towers needed to achieve ubiquitous coverage in the simulation area increases dramatically, from none for 1.9-GHz LTE, all the way to 32 988 for 28-GHz mmWave. The average cost for constructing one conventional cellular site today is estimated to be 200,000–250,000 dollars [30]. Building another 32 thousand towers is simply impractical. After all, we only have in total 819 towers in the area of interest based on our cell tower location data. Apparently, densification alone is not a good enough solution for rural coverage, especially for mmWave.

It is worth noting that the estimated numbers of new towers here are in fact lower-bound estimates because we have loosened many simulation conditions. For example, as mentioned before, the towers in our systems are always shared among all the network operators and carriers, even the small regional ones, for the best possible coverage. That may not be the case in real life. Also, the 10-dB margin we applied beyond the maximum path loss a 4G LTE system can endure (140 dB), implies that the devices in our simulations are of a higher quality than typical off-the-shelf ones. What's more, the shape of a cell is usually a circle if we want to achieve the biggest coverage, but in our calculations, we assumed the cell shape for the new towers can be anything as necessary to cover the area of interest, without any punishment. In a word, more towers could be needed in real-life network deployments than the values we got from the simulations.

6.3 Discussion

In this chapter, we examined the results of the large-scale cellular coverage analyses for different carrier frequencies. Based on real-life cell tower locations and LiDAR data, the current condition of the digital divide was quantified via the cumulative blockage distance and the estimated number of new towers needed to achieve ubiquitous coverage. Although most research efforts on mmWaves are for urban environments, the difficulty in successfully applying mmWaves in a WLAN ubiquitously covering the vast rural areas is as great as, if not bigger than, that for urban-environment mmWave communications. Without proper interventions, the digital gap will be widened by the popularization of mmWave in urban regions. There is no simple solution to this challenge. Instead, an urgent need is there for researchers to work on achieving the ubiquitous coverage demanded by our future society.

7. CONCLUSIONS

In this dissertation, we have explored the possibility of taking advantage of site-specific geographic features in improving and developing channel models for millimeter waves (mmWaves). This approach takes into consideration one of the salient characteristics that the mmWave signal propagation has: the sensitivity to blockages. Based on measurement campaign results obtained for suburban and rural environments, we proposed site-specific models for one-building blockage and propagation through the foliage. They outperformed traditional channel models with improved accuracy. We also investigated large-scale channel simulation following the techniques used in the site-specific channel modeling. In the future, we would like to (i) expand the idea of site-specific channel modeling and (ii) apply machine learning, to construct scenario-generic channel models with high performance.

7.1 Scenario-Generic Site-Specific Channel Modeling

Figure 7.1 summarizes the difference between the traditional and the site-specific channel models. The input to the traditional models, i.e., the dominating parameters in Figure 7.1a, typically are not affected by the site-specific features. For instance, the ITU model for propagation over rooftops does not care about where exactly the buildings are, and the ITU model for propagation through foliage does not care about where exactly the trees are. For mmWaves, though, moving the RX by a very short distance could change the channel condition from line-of-sight (LOS) to non-line-of-sight (NLOS) because of obstacles, and vice versa. Without considering the locations and sizes of the obstacles, this phenomenon will not be accurately reflected in the channel models.

The site-specific models (Figure 7.1b), on the other hand, not only considers the TX and RX locations, but also the site-specific features in the area of interest. This makes it possible to evaluate site-specific parameters only applicable for a given pair of TX and RX locations. Thus, even local blockages could be captured properly. For example, in our one-building-blockage model and the site-specific models for propagation through the foliage, we essentially trace one ray between the TX and the RX to identify and compensate for these blockages.

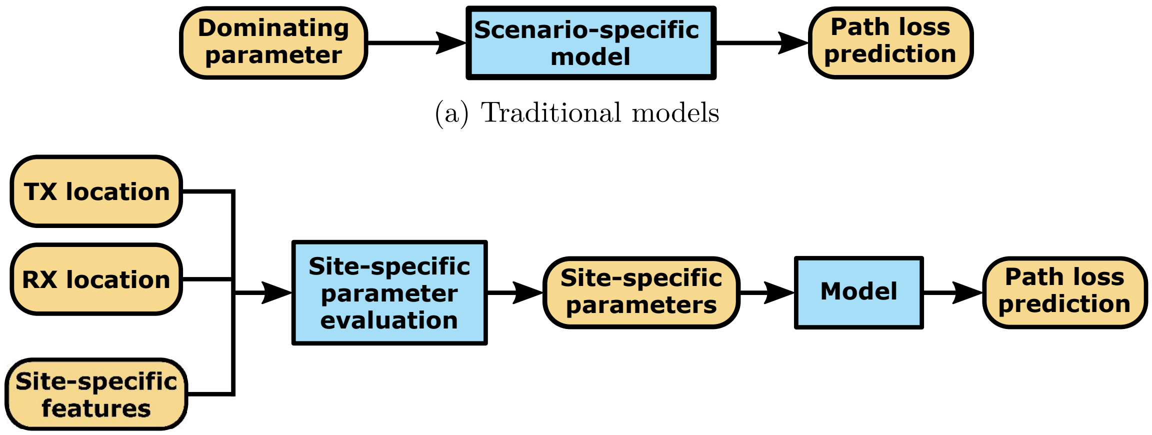

(a) Traditional models

(b) Site-specific models

Figure 7.1. Block diagrams for traditional and site-specific models.

Resultant site-specific models are still simple to understand, easy to use, and fully automatable. Figure 7.2 showcases the site-specific model C we developed in Chapter 4. The foliage coverage information was extracted from the United States Geographic Survey (USGS) LiDAR and elevation information for the area of interest. A debugger took in the foliage coverage and overlaid it on Google satellite imaginary for user-friendly visualizations. This is helpful for human operators to verify the results. Together with the TX and RX locations, the foliage coverage information enables site-specific evaluation of the parameter foliage area, A_f, which is needed in the model to make a path loss prediction. This full automation is a huge advantage, especially for large-scale network planning and performance evaluation.

More generally, our approach has the potential to embed the manual environment determination procedure into fully automated channel models. Traditional models are scenario-specific, as illustrated in Figure 7.1a. Each model was developed for and is expected to be used in, one type of environment, e.g., urban canyon, suburban rooftops, and rural forest. Users have to determine, normally manually, which environment best describes the area of interest. This dramatically limits the usability of the traditional models, especially in large-scale network planning because multiple environments may be involved. In that case, operators have to manually divide and categorize the area of interest into smaller regions with different propagation scenarios, choose for each scenario a good model, and then evaluate the dominating parameter(s) defined in each chosen model to calculate the prediction

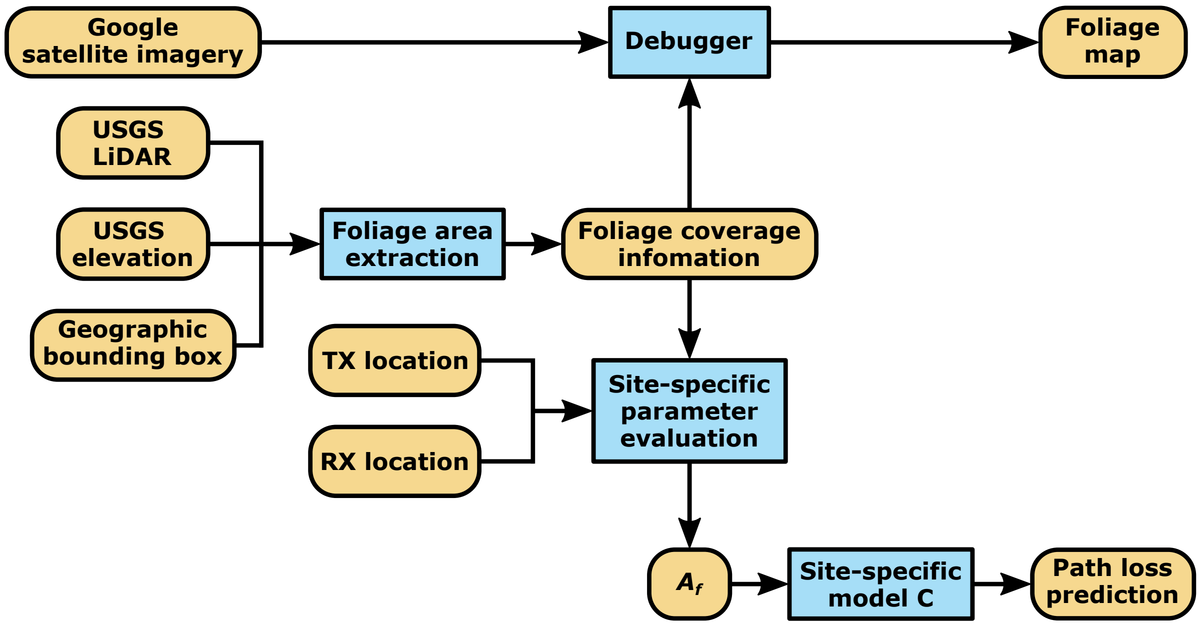

Figure 7.2. Fully automated site-specific model C.

values. This procedure takes a huge amount of human labor and is very challenging to automate.

On the contrary, our site-specific channel modeling approach, as plotted in Figure 7.3, can hide the scenario determination from the users in the site-specific parameter evaluation procedure. This is possible because the site-specific features implicitly contain the required information for making the decision. For example, whenever one-building or foliage blockage happens, path loss adjustments can be evaluated via our site-specific channel models, regardless of which scenario or environment the location of interest is located in. Then, the final path loss prediction is obtained via aggregating (normally by summing up the path loss values in dB) these adjustments to a baseline model, e.g., the alpha-beta-gamma model. This approach is very flexible because different modules could be added for different obstacles, following the concepts introduced in the partition-dependent attenuation factor model [74].

7.2 Large-Scale Channel Simulation

As we have seen in Chapters 3 and 4, the site-specific models perform better than traditional ones thanks to the site-specific features. They are easy to implement and fully

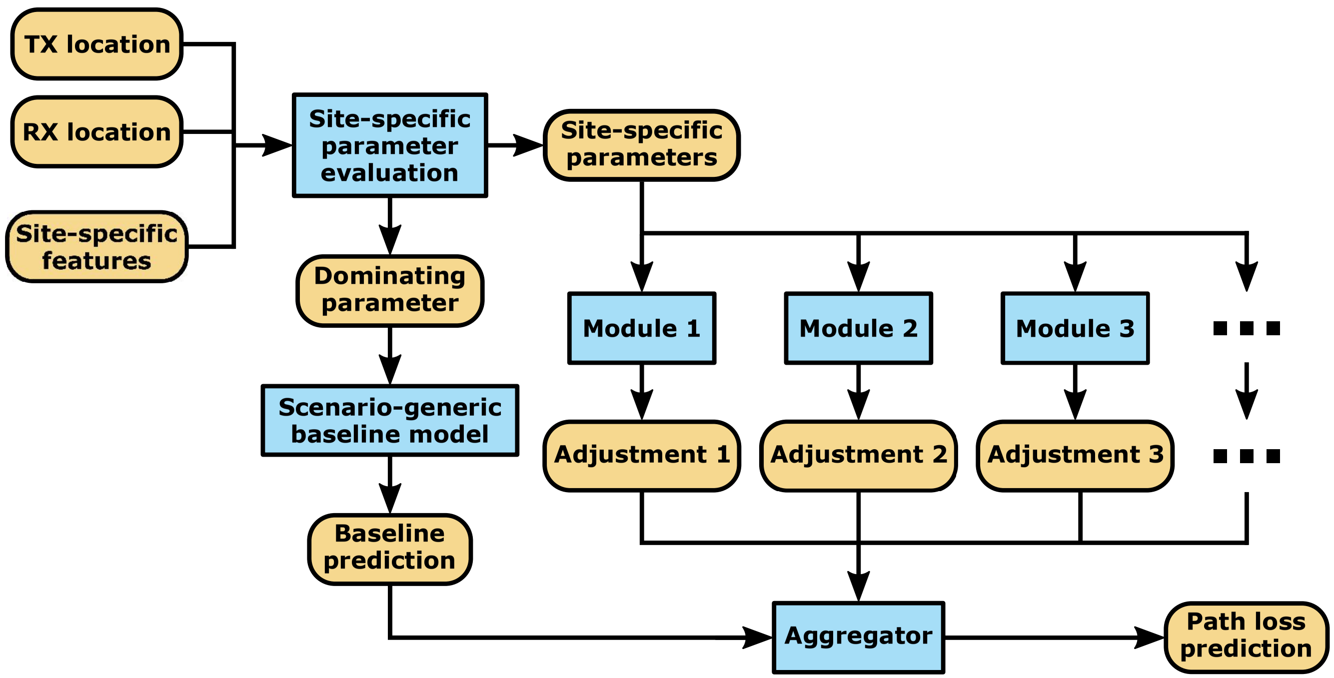

Figure 7.3. Site-specific features can enable scenario-generic channel modeling.

automatable. And the computational cost is very low due to their simple structures. Furthermore, these features fit the requirements for large-scale channel simulations.

In fact, our simulator used in Chapters 5 and 6 essentially follows the same structure of the site-specific model C implementation, as illustrated in the block diagram Figure 7.4. We have (i) the core, a parallel computing pool, to carry out the simulation, (ii) the preprocessors, which prepare the data for the simulation, and (iii) postprocessors to analyze and visualize the results. As one of the preprocessors, the location sampler chooses the locations to inspect according to the area of interest. These are where the users will show up. The tower range manager determines which towers to consider. We also have the geographic data preprocessor to index LiDAR and elevation data for faster data retrieval. Then, the workload scheduler distributes workload among the workers and oversees the simulation. It also generates recovery points for resuming the simulation in case of interruptions. The parallel computing pool calculates the blockage status, based on our LoS blockage model, and the path loss values, based on the National Telecommunications and Information Administration (NTIA) extended Hata (eHata) model. The blockage maps and the path loss maps are generated accordingly by the postprocessor visualizer.

In a nutshell, we would not have been able to build the large-scale simulator without the techniques in the site-specific channel modeling. Comparing Figure 7.4 with Figure 7.3, we can see that the preprocessors in the cellular coverage simulator complete the procedure *site-specific parameter evaluation*. The core carries out the simulation based on the *module* of the LoS blockage model and the *module* of the NTIA eHata model. Although it is not clear in Figure 7.4, we have the free-space propagation loss (FSPL) model as the *scenario-generic baseline model* for sanity checks. Last but not least, the visualizer takes charge of the *aggregator*'s job.

7.3 Applying Machine Learning in Channel Modeling

The feature of full automation and consideration of local geographic information in site-specific channel modeling also builds the foundation of applying data-driven machine-learning techniques. This needs to be done with caution, though, because channel modeling

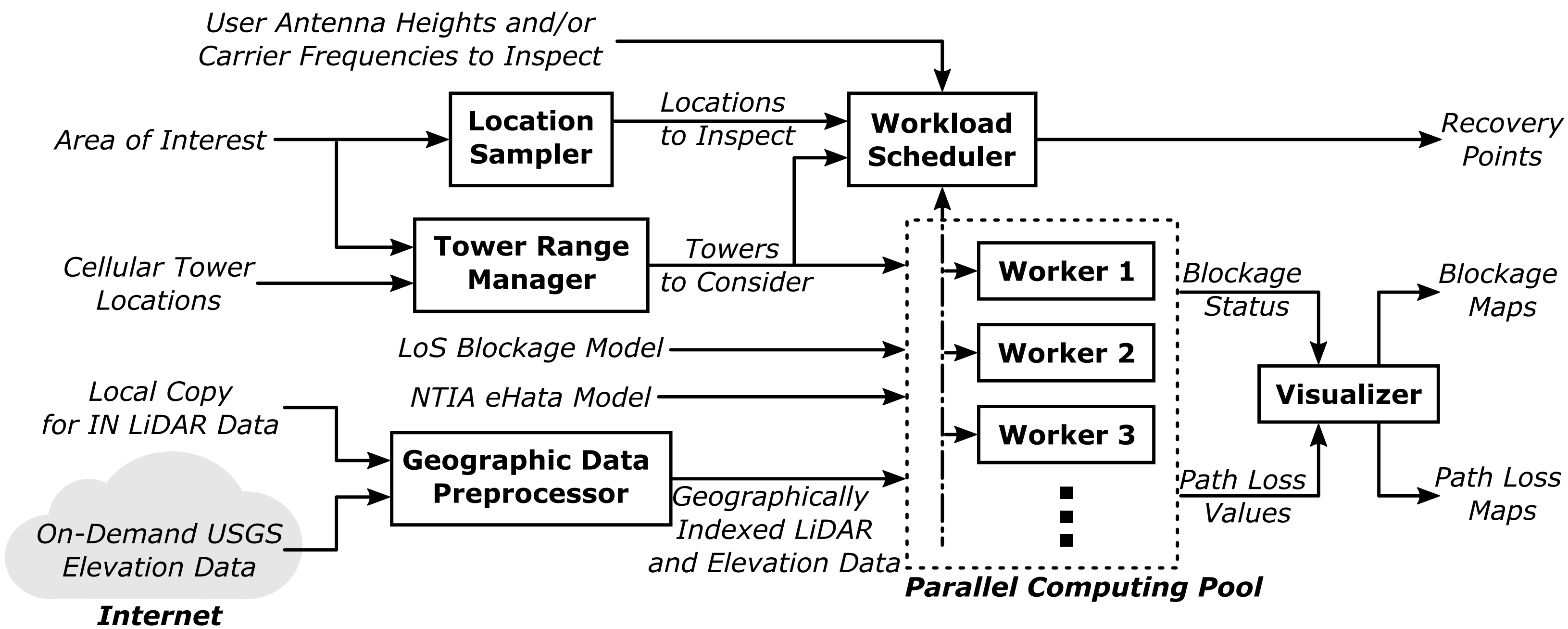

Figure 7.4. Block diagram of the cellular coverage simulator.

and machine learning have been developing independently for a long time and they follow very different philosophies.

More specifically, these two areas have adopted very different procedures in model validation. In traditional channel modeling, researchers are often inspired by physics to propose models with new structures. The validity of these models, in some sense, is guaranteed by the physics behind them. Also, measurement results are typically expensive to obtain, and thus, quite limited. As a result, it is common to use the same set of measurements to both adjust (or train) and validate (or test) the models of interest to compare their potentially best performances. There are so many factors that could influence the channel. The challenge in channel modeling is not to name some that may be relevant, but to identify the important ones that are essential/the true causes and quantify their influences. The traditional channel modeling process helps tackle this challenge with limited measurement results.

In machine learning, data are normally cheap to obtain. One would rely on a large amount of data to reveal the true structure behind the scene, without caring much about how things should work theoretically, typically until we find something that works and we want to understand why. With this approach, the data sets play a key role. That is why it is normally required to use different data sets to train and test the models separately, to prove that the model should also work for unseen data/scenarios.

When these two areas are combined, it may seem intriguing to take the "easy" paths in both of them: following the traditions in channel modeling, use only one data set for both training and testing, and following the traditions in machine learning, discard physics/analyses on how things should work. However, these two choices simply should not be taken at the same time. The generalizability in traditional channel models is from physics, while in machine learning, it is from testing with unseen data sets. Without both, we will lose our ability to back up the generalizability of the new model. One extreme example would be, by using a simple nearest-neighbor fitting as the machine learning component, we can expect zero root mean square error (RMSE) (i.e., the perfect performance) because the same data set is used for training and testing. But in theory, this new model will not generalize at all beyond the measurement data set.

What is more, pure data-driven channel models backed by machine learning could have limited application, because the results may not be explainable. This is undesirable in many cases. A network operator would need to understand why the model output is high/low to lay out actionable strategies to improve the network performance. A regulator would need to provide clear explanations on their decisions if they are based on a channel model. In this sense, the site-specific channel modeling framework illustrated in Figure 7.3 provides a better solution. The baseline model and the site-specific channel model modules can be predefined and be fully understood, with only the parameter evaluation procedures and the result aggregator being improved by the machine learning techniques.

7.4 Summary

This dissertation confirmed the extreme sensitivity of mmWave signals to blockages in suburban and rural environments via two intensive channel measurement campaigns. With the consideration of geographic information, site-specific channel models were developed for future wireless networks to better face this challenge. Also, a framework for site-specific channel modeling was proposed to enable scenario-generic channel models. The same techniques were applied to large-scale channel simulations to locate poorly covered spots and quantify network performance in real life. The severity of the digital divide was revealed via state-level cellular coverage simulations. The site-specific channel models with improved accuracy can facilitate the deployment of mmWave systems, while the channel simulations with improved scalability can give us a deeper understanding of the system-level performance of real-life wireless networks.

REFERENCES

[1] Y. Zhang, D. J. Love, J. V. Krogmeier, C. R. Anderson, R. W. Heath, and D. R. Buckmaster, “Challenges and opportunities of future rural wireless communications,” *IEEE Communications Magazine*, Dec. 2021, to be published.

[2] Cisco, “Cisco visual networking index: Global mobile data traffic forecast update, 2017–
2022,” Tech. Rep. C11-738429-01, Feb. 2019. [Online]. Available: https://s3.amazonaws.com/media.mediapost.com/uploads/CiscoForecast.pdf.

[3] T. S. Rappaport, S. Sun, R. Mayzus, H. Zhao, Y. Azar, K. Wang, G. N. Wong, J. K. Schulz, M. Samimi, and F. Gutierrez, “Millimeter wave mobile communications for 5G cellular: It will work!” *IEEE Access*, vol. 1, pp. 335–349, 2013. DOI: 10.1109/access.2013.2260813.

[4] S. Rangan, T. S. Rappaport, and E. Erkip, “Millimeter-wave cellular wireless networks: Potentials and challenges,” *Proceedings of the IEEE*, vol. 102, no. 3, pp. 366–385, Mar. 2014. DOI: 10.1109/jproc.2014.2299397. eprint: 1401.2560.

[5] Y. Niu, Y. Li, D. Jin, L. Su, and A. V. Vasilakos, “A survey of millimeter wave communications (mmWave) for 5G: Opportunities and challenges,” *Wireless Networks*, vol. 21, no. 8, pp. 2657–2676, Apr. 2015. DOI: 10.1007/s11276-015-0942-z.

[6] J. Du, E. Onaran, D. Chizhik, S. Venkatesan, and R. A. Valenzuela, “Gbps user rates using mmWave relayed backhaul with high-gain antennas,” *IEEE Journal on Selected Areas in Communications*, vol. 35, no. 6, pp. 1363–1372, Jun. 2017. DOI: 10.1109/jsac.2017.2686578.

[7] B. Yang, Z. Yu, J. Lan, R. Zhang, J. Zhou, and W. Hong, “Digital beamforming-based massive MIMO transceiver for 5G millimeter-wave communications,” *IEEE Transactions on Microwave Theory and Techniques*, vol. 66, no. 7, pp. 3403–3418, Jul. 2018. DOI: 10.1109/tmtt.2018.2829702.

[8] T. K. Vu, M. Bennis, M. Debbah, M. Latva-aho, and C. S. Hong, “Ultra-reliable communication in 5G mmWave networks: A risk-sensitive approach,” *IEEE Communications Letters*, vol. 22, no. 4, pp. 708–711, Apr. 2018. DOI: 10.1109/lcomm.2018.2802902.

[9] M. K. Samimi and T. S. Rappaport, “3-D millimeter-wave statistical channel model for 5G wireless system design,” *IEEE Transactions on Microwave Theory and Techniques*, vol. 64, no. 7, pp. 2207–2225, Jul. 2016. DOI: 10.1109/tmtt.2016.2574851.

[10] J. Gozalvez, M. Sepulcre, and R. Bauza, "IEEE 802.11p vehicle to infrastructure communications in urban environments," *IEEE Communications Magazine*, vol. 50, no. 5, pp. 176–183, May 2012. DOI: 10.1109/mcom.2012.6194400.

[11] T. S. Rappaport, F. Gutierrez, E. Ben-Dor, J. N. Murdock, Y. Qiao, and J. I. Tamir, "Broadband millimeter-wave propagation measurements and models using adaptive-beam antennas for outdoor urban cellular communications," *IEEE Transactions on Antennas and Propagation*, vol. 61, no. 4, pp. 1850–1859, Apr. 2013. DOI: 10.1109/tap.2012.2235056.

[12] G. R. MacCartney, J. Zhang, S. Nie, and T. S. Rappaport, "Path loss models for 5G millimeter wave propagation channels in urban microcells," in *2013 IEEE Global Communications Conference (GLOBECOM)*, IEEE, Dec. 2013. DOI: 10.1109/glocom.2013.6831690.

[13] S. Nie, G. R. MacCartney, S. Sun, and T. S. Rappaport, "72 GHz millimeter wave indoor measurements for wireless and backhaul communications," in *2013 IEEE 24th Annual International Symposium on Personal, Indoor, and Mobile Radio Communications (PIMRC)*, IEEE, Sep. 2013. DOI: 10.1109/pimrc.2013.6666553.

[14] G. R. MacCartney, M. K. Samimi, and T. S. Rappaport, "Omnidirectional path loss models in New York City at 28 GHz and 73 GHz," in *2014 IEEE 25th Annual International Symposium on Personal, Indoor, and Mobile Radio Communication (PIMRC)*, IEEE, Sep. 2014. DOI: 10.1109/pimrc.2014.7136165.

[15] S. Hur, Y.-J. Cho, J. Lee, N.-G. Kang, J. Park, and H. Benn, "Synchronous channel sounder using horn antenna and indoor measurements on 28 GHz," in *2014 IEEE International Black Sea Conference on Communications and Networking (BlackSeaCom)*, IEEE, May 2014. DOI: 10.1109/blackseacom.2014.6849010.

[16] O. H. Koymen, A. Partyka, S. Subramanian, and J. Li, "Indoor mm-wave channel measurements: Comparative study of 2.9 GHz and 29 GHz," in *2015 IEEE Global Communications Conference (GLOBECOM)*, IEEE, Dec. 2015. DOI: 10.1109/glocom.2015.7417720.

[17] S. Sun, T. A. Thomas, T. S. Rappaport, H. Nguyen, I. Z. Kovacs, and I. Rodriguez, "Path loss, shadow fading, and line-of-sight probability models for 5G urban macro-cellular scenarios," in *2015 IEEE Globecom Workshops (GC Wkshps)*, IEEE, Dec. 2015. DOI: 10.1109/glocomw.2015.7414036.

[18] G. R. Maccartney, T. S. Rappaport, S. Sun, and S. Deng, "Indoor office wideband millimeter-wave propagation measurements and channel models at 28 and 73 GHz for ultra-dense 5G wireless networks," *IEEE Access*, vol. 3, pp. 2388–2424, 2015. DOI: 10.1109/access.2015.2486778.

[19] T. A. Thomas, M. Rybakowski, S. Sun, T. S. Rappaport, H. Nguyen, I. Z. Kovacs, and I. Rodriguez, "A prediction study of path loss models from 2-73.5 GHz in an urban-macro environment," in *2016 IEEE 83rd Vehicular Technology Conference (VTC Spring)*, IEEE, May 2016. DOI: 10.1109/vtcspring.2016.7504094.

[20] S. Sun, T. S. Rappaport, S. Rangan, T. A. Thomas, A. Ghosh, I. Z. Kovacs, I. Rodriguez, O. Koymen, A. Partyka, and J. Jarvelainen, "Propagation path loss models for 5G urban micro- and macro-cellular scenarios," in *2016 IEEE 83rd Vehicular Technology Conference (VTC Spring)*, IEEE, May 2016. DOI: 10.1109/vtcspring.2016.7504435.

[21] K. Haneda, L. Tian, H. Asplund, J. Li, Y. Wang, D. Steer, C. Li, T. Balercia, S. Lee, Y. Kim, A. Ghosh, T. Thomas, T. Nakamurai, Y. Kakishima, T. Imai, H. Papadopoulas, T. S. Rappaport, G. R. MacCartney, M. K. Samimi, S. Sun, O. Koymen, S. Hur, J. Park, J. Zhang, E. Mellios, A. F. Molisch, S. S. Ghassamzadeh, and A. Ghosh, "Indoor 5G 3GPP-like channel models for office and shopping mall environments," May 2016. DOI: 10.1109/iccw.2016.7503868.

[22] S. Sun, G. R. MacCartney, and T. S. Rappaport, "Millimeter-wave distance-dependent large-scale propagation measurements and path loss models for outdoor and indoor 5G systems," in *2016 10th European Conference on Antennas and Propagation (EuCAP)*, IEEE, Apr. 2016. DOI: 10.1109/eucap.2016.7481506.

[23] S. Sun, H. Yan, G. R. MacCartney, and T. S. Rappaport, "Millimeter wave small-scale spatial statistics in an urban microcell scenario," in *2017 IEEE International Conference on Communications (ICC)*, IEEE, May 2017. DOI: 10.1109/icc.2017.7996408.

[24] J. Ryan, G. R. MacCartney, and T. S. Rappaport, "Indoor office wideband penetration loss measurements at 73 GHz," in *2017 IEEE International Conference on Communications Workshops (ICC Workshops)*, IEEE, May 2017. DOI: 10.1109/iccw.2017.7962662.

[25] I. Rodriguez, E. P. L. Almeida, R. Abreu, M. Lauridsen, A. Loureiro, and P. Mogensen, "Analysis and comparison of 24 GHz cmWave radio propagation in urban and suburban scenarios," in *2016 IEEE Wireless Communications and Networking Conference*, IEEE, Apr. 2016. DOI: 10.1109/wcnc.2016.7564893.

[26] G. R. MacCartney and T. S. Rappaport, "Rural macrocell path loss models for millimeter wave wireless communications," *IEEE Journal on Selected Areas in Communications*, vol. 35, no. 7, pp. 1663–1677, Jul. 2017. DOI: 10.1109/jsac.2017.2699359.

[27] "Working group 5 final report 1755–1850 MHz airborne operations," National Telecommunications and Information Administration, Commerce Spectrum Management Advisory Committee, Tech. Rep., Sep. 13, 2013. [Online]. Available: https://www.ntia.doc.gov/files/ntia/publications/wg5_1755-1850_final_reportl-09-16-2013.pdf.

[28] A. Scott, "Understanding the true state of connectivity in America," National Association of Counties, Tech. Rep., Mar. 2020. [Online]. Available: https://www.naco.org/resources/featured/understanding-true-state-connectivity-america.

[29] "New census data show differences between urban and rural populations," U.S. Census Bureau, Tech. Rep., Dec. 8, 2016. [Online]. Available: https://www.census.gov/newsroom/press-releases/2016/cb16-210.html.

[30] "The last-mile Internet connectivity solutions guide: Sustainable connectivity options for unconnected sites," International Telecommunication Union, ITU Publications, Geneva, Switzerland, Tech. Rep., 2020.

[31] Z. Zhang, Y. Xiao, Z. Ma, M. Xiao, Z. Ding, X. Lei, G. K. Karagiannidis, and P. Fan, "6G wireless networks: Vision, requirements, architecture, and key technologies," *IEEE Vehicular Technology Magazine*, vol. 14, no. 3, pp. 28–41, Sep. 2019. DOI: 10.1109/mvt.2019.2921208.

[32] Cisco, "Cisco annual internet report (2018–2023)," Tech. Rep. C11-741490-01, Mar. 2020. [Online]. Available: https://www.cisco.com/c/en/us/solutions/collateral/executive-perspectives/annual-internet-report/white-paper-c11-741490.pdf.

[33] American Broadband Initiative, "A case for rural broadband: Insights on rural broadband infrastructure and next generation precision agriculture technologies," U.S. Department of Agriculture, Tech. Rep., Apr. 2019. [Online]. Available: https://www.usda.gov/sites/default/files/documents/case-for-rural-broadband.pdf.

[34] "Intelligent transportation systems benefits for rural communities," U.S. Department of Transportation, ITS Professional Capacity Building Program, Tech. Rep., 2018. [Online]. Available: https://www.its.dot.gov/factsheets/pdf/Rural.pdf.

[35] T. S. El-Bawab, "Toward access equality: Bridging the digital divide," *IEEE Communications Magazine*, vol. 58, no. 12, pp. 6–7, Dec. 2020. DOI: 10.1109/mcom.2020.9311933.

[36] M. Jaber, M. A. Imran, R. Tafazolli, and A. Tukmanov, "5G backhaul challenges and emerging research directions: A survey," *IEEE Access*, vol. 4, pp. 1743–1766, 2016. DOI: 10.1109/access.2016.2556011.

[37] H. Jung and I.-H. Lee, "Outage analysis of millimeter-wave wireless backhaul in the presence of blockage," *IEEE Communications Letters*, vol. 20, no. 11, pp. 2268–2271, Nov. 2016. DOI: 10.1109/lcomm.2016.2598143.

[38] J. Shi, L. Lv, Q. Ni, H. Pervaiz, and C. Paoloni, "Modeling and analysis of point-to-multipoint millimeter wave backhaul networks," *IEEE Transactions on Wireless Communications*, vol. 18, no. 1, pp. 268–285, Jan. 2019. DOI: 10.1109/twc.2018.2879109.

[39] W. Lambrechts and S. Sinha, "Terrestrial and millimeter-wave mobile backhaul: A last mile solution," in *Last Mile Internet Access for Emerging Economies*, Springer International Publishing, 2019, pp. 143–183. DOI: 10.1007/978-3-030-20957-5_5.

[40] P. Choi, D. A. Antoniadis, and E. A. Fitzgerald, "Towards millimeter-wave phased array circuits and systems for small form factor and power efficient 5G mobile devices," in *2019 IEEE International Symposium on Phased Array System & Technology (PAST)*, IEEE, Oct. 2019. DOI: 10.1109/past43306.2019.9021005.

[41] A. F. Molisch, V. V. Ratnam, S. Han, Z. Li, S. L. H. Nguyen, L. Li, and K. Haneda, "Hybrid beamforming for massive MIMO: A survey," *IEEE Communications Magazine*, vol. 55, no. 9, pp. 134–141, 2017. DOI: 10.1109/mcom.2017.1600400.

[42] S. Sun, T. Rappaport, R. Heath, A. Nix, and S. Rangan, "MIMO for millimeter-wave wireless communications: Beamforming, spatial multiplexing, or both?" *IEEE Communications Magazine*, vol. 52, no. 12, pp. 110–121, Dec. 2014. DOI: 10.1109/mcom.2014.6979962.

[43] V. Degli-Esposti, F. Fuschini, E. M. Vitucci, M. Barbiroli, M. Zoli, L. Tian, X. Yin, D. A. Dupleich, R. Muller, C. Schneider, and R. S. Thoma, "Ray-tracing-based mm-wave beamforming assessment," *IEEE Access*, vol. 2, pp. 1314–1325, 2014. DOI: 10.1109/access.2014.2365991.

[44] Y. Zhang, S. Jyoti, C. R. Anderson, D. J. Love, N. Michelusi, A. Sprintson, and J. V. Krogmeier, "28-GHz channel measurements and modeling for suburban environments," in *2018 IEEE International Conference on Communications (ICC)*, IEEE, May 2018, pp. 1–6. DOI: 10.1109/icc.2018.8422820.

[45] Y. Zhang, D. J. Love, N. Michelusi, J. V. Krogmeier, S. Jyoti, A. Sprintson, and C. R. Anderson, "Improving millimeter-wave channel models for suburban environments with site-specific geometric features," in *2018 International Applied Computational Electromagnetics Society Symposium (ACES)*, IEEE, Mar. 2018, pp. 1–2. DOI: 10.23919/ropaces.2018.8364140.

[46] Y. Zhang, C. R. Anderson, N. Michelusi, D. J. Love, K. R. Baker, and J. V. Krogmeier, "Propagation modeling through foliage in a coniferous forest at 28 GHz," *IEEE Wireless Communications Letters*, vol. 8, no. 3, pp. 901–904, Jun. 2019. DOI: 10.1109/lwc.2019.2899299.

[47] V. M. Nguyen and M. Kountouris, "Performance limits of network densification," *IEEE Journal on Selected Areas in Communications*, vol. 35, no. 6, pp. 1294–1308, Jun. 2017. DOI: 10.1109/jsac.2017.2687638.

[48] J. Zhu, M. Zhao, and S. Zhou, "An optimization design of ultra dense networks balancing mobility and densification," *IEEE Access*, vol. 6, pp. 32 339–32 348, 2018. DOI: 10.1109/access.2018.2845690.

[49] J. Qiao, L. X. Cai, and X. Shen, "Multi-hop concurrent transmission in millimeter wave WPANs with directional antenna," May 2010. DOI: 10.1109/icc.2010.5502300.

[50] S. Sun, G. R. MacCartney, M. K. Samimi, and T. S. Rappaport, "Synthesizing omnidirectional antenna patterns, received power and path loss from directional antennas for 5G millimeter-wave communications," in *2015 IEEE Global Communications Conference (GLOBECOM)*, IEEE, Dec. 2015. DOI: 10.1109/glocom.2015.7417335.

[51] X. Yu, J. Zhang, M. Haenggi, and K. B. Letaief, "Coverage analysis for millimeter wave networks: The impact of directional antenna arrays," *IEEE Journal on Selected Areas in Communications*, vol. 35, no. 7, pp. 1498–1512, Jul. 2017. DOI: 10.1109/jsac.2017.2699098.

[52] J. Choi, J. Choi, and W. Hwang, "Miniature millimeter-wave 5G antenna fabricated using anodized aluminum oxide for mobile devices," *ACS Omega*, vol. 5, no. 40, pp. 26 206–26 210, Oct. 2020. DOI: 10.1021/acsomega.0c03795.

[53] W. Hong, Z. H. Jiang, C. Yu, J. Zhou, P. Chen, Z. Yu, H. Zhang, B. Yang, X. Pang, M. Jiang, Y. Cheng, M. K. T. Al-Nuaimi, Y. Zhang, J. Chen, and S. He, "Multibeam antenna technologies for 5G wireless communications," *IEEE Transactions on Antennas and Propagation*, vol. 65, no. 12, pp. 6231–6249, Dec. 2017. DOI: 10.1109/tap.2017.2712819.

[54] Y. Zeng and R. Zhang, "Millimeter wave MIMO with lens antenna array: A new path division multiplexing paradigm," *IEEE Transactions on Communications*, vol. 64, no. 4, pp. 1557–1571, Apr. 2016. DOI: 10.1109/tcomm.2016.2533490.

[55] P. Liu, M. D. Renzo, and A. Springer, "Line-of-sight spatial modulation for indoor mmWave communication at 60 GHz," *IEEE Transactions on Wireless Communications*, vol. 15, no. 11, pp. 7373–7389, Nov. 2016. DOI: 10.1109/twc.2016.2601616.

[56] M. N. Kulkarni, S. Singh, and J. G. Andrews, “Coverage and rate trends in dense urban mmWave cellular networks,” in *2014 IEEE Global Communications Conference*, IEEE, Dec. 2014. DOI: 10.1109/glocom.2014.7037401.

[57] J. G. Andrews, T. Bai, M. Kulkarni, A. Alkhateeb, A. Gupta, and R. W. Heath, “Modeling and analyzing millimeter wave cellular systems,” *IEEE Transactions on Communications*, pp. 1–1, 2016. DOI: 10.1109/tcomm.2016.2618794.

[58] V. Petrov, D. Solomitckii, A. Samuylov, M. A. Lema, M. Gapeyenko, D. Moltchanov, S. Andreev, V. Naumov, K. Samouylov, M. Dohler, and Y. Koucheryavy, “Dynamic multi-connectivity performance in ultra-dense urban mmWave deployments,” *IEEE Journal on Selected Areas in Communications*, vol. 35, no. 9, pp. 2038–2055, Sep. 2017. DOI: 10.1109/jsac.2017.2720482.

[59] C. Perfecto, J. D. Ser, and M. Bennis, “Millimeter-wave V2V communications: Distributed association and beam alignment,” *IEEE Journal on Selected Areas in Communications*, vol. 35, no. 9, pp. 2148–2162, Sep. 2017. DOI: 10.1109/jsac.2017.2719998.

[60] Z. Li, L. Xiang, X. Ge, G. Mao, and H.-C. Chao, “Latency and reliability of mmWave multi-hop V2V communications under relay selections,” *IEEE Transactions on Vehicular Technology*, vol. 69, no. 9, pp. 9807–9821, Sep. 2020. DOI: 10.1109/tvt.2020.3002903.

[61] M. Ozpolat, K. Bhargava, E. Kampert, and M. D. Higgins, “Multi-lane urban mmWave V2V networks: A path loss behaviour dependent coverage analysis,” *Vehicular Communications*, vol. 30, p. 100 348, Aug. 2021. DOI: 10.1016/j.vehcom.2021.100348.

[62] H. Jung and I.-H. Lee, “Performance analysis of millimeter-wave UAV swarm networks under blockage effects,” *Sensors*, vol. 20, no. 16, p. 4593, Aug. 2020. DOI: 10.3390/s20164593.

[63] L. Cheng, Q. Zhu, C.-X. Wang, W. Zhong, B. Hua, and S. Jiang, “Modeling and simulation for UAV air-to-ground mmWave channels,” in *2020 14th European Conference on Antennas and Propagation (EuCAP)*, IEEE, Mar. 2020. DOI: 10.23919/eucap48036.2020.9136077.

[64] H. Ding, H. Dai, I. Guvenc, and A. Bhuyan, “Outage analysis for cooperative mmWave UAV communications with beam training overhead,” *IEEE Wireless Communications Letters*, pp. 1–1, 2021. DOI: 10.1109/LWC.2021.3098424.

[65] R. J. Pirkl and G. D. Durgin, “Optimal sliding correlator channel sounder design,” *IEEE Transactions on Wireless Communications*, vol. 7, no. 9, pp. 3488–3497, Sep. 2008. DOI: 10.1109/twc.2008.070278.

[66] International Telecommunication Union, “Propagation data and prediction methods for the planning of short-range outdoor radiocommunication systems and radio local area networks in the frequency range 300MHz and 100GHz,” Tech. Rep., Jun. 2017. [Online]. Available: https://www.itu.int/rec/R-REC-P.1411-9-201706-I/en.

[67] Y. Zhang, D. J. Love, N. Michelusi, J. V. Krogmeier, C. R. Anderson, S. Jyoti, and A. Sprintson, “28-GHz channel measurements and modeling for suburban environments,” Department of Electrical and Computer Engineering, Purdue University, West Lafayette, Indiana, Tech. Rep. TR-ECE-17-07, Nov. 2017. [Online]. Available: https://docs.lib.purdue.edu/ecetr/483/.

[68] L. Tian, V. Degli-Esposti, E. M. Vitucci, and X. Yin, “Semi-deterministic radio channel modeling based on graph theory and ray-tracing,” *IEEE Transactions on Antennas and Propagation*, vol. 64, no. 6, pp. 2475–2486, Jun. 2016. DOI: 10.1109/tap.2016.2546950.

[69] N. R. Leonor, T. R. Fernandes, M. G. Sanchez, and R. F. S. Caldeirinha, “A 3-D model for millimeter-wave propagation through vegetation media using ray-tracing,” *IEEE Transactions on Antennas and Propagation*, vol. 67, no. 6, pp. 4313–4318, Jun. 2019. DOI: 10.1109/tap.2019.2905957.

[70] F. Fuschini, M. Zoli, E. M. Vitucci, M. Barbiroli, and V. Degli-Esposti, “A study on millimeter-wave multiuser directional beamforming based on measurements and ray tracing simulations,” *IEEE Transactions on Antennas and Propagation*, vol. 67, no. 4, pp. 2633–2644, Apr. 2019. DOI: 10.1109/tap.2019.2894271.

[71] M. Z. Aslam, Y. Corre, J. Belschner, G. S. Arockiaraj, and M. Jager, “Analysis of 60-GHz in-street backhaul channel measurements and LiDAR ray-based simulations,” in *2020 14th European Conference on Antennas and Propagation (EuCAP)*, IEEE, Mar. 2020. DOI: 10.23919/eucap48036.2020.9135946.

[72] K. Guan, B. Peng, D. He, J. M. Eckhardt, H. Yi, S. Rey, B. Ai, Z. Zhong, and T. Kurner, “Channel sounding and ray tracing for intrawagon scenario at mmWave and sub-mmWave bands,” *IEEE Transactions on Antennas and Propagation*, vol. 69, no. 2, pp. 1007–1019, Feb. 2021. DOI: 10.1109/tap.2020.3016399.

[73] T. S. Rappaport, G. R. MacCartney, S. Sun, H. Yan, and S. Deng, “Small-scale, local area, and transitional millimeter wave propagation for 5G communications,” *IEEE Transactions on Antennas and Propagation*, vol. 65, no. 12, pp. 6474–6490, Dec. 2017. DOI: 10.1109/tap.2017.2734159.

[74] G. Durgin, T. S. Rappaport, and H. Xu, “Measurements and models for radio path loss and penetration loss in and around homes and trees at 5.85 GHz,” *IEEE Transactions on Communications*, vol. 46, no. 11, pp. 1484–1496, 1998. DOI: 10.1109/26.729393.

[75] International Telecommunication Union, “Recommendation ITU-R P.833-9 attenuation in vegetation,” Tech. Rep., Sep. 2016, Accessed: Apr. 12, 2020. [Online]. Available: https://www.itu.int/rec/R-REC-P.833-9-201609-I/en.

[76] M. A. Weissberger, “An initial critical summary of models for predicting the attenuation of radio waves by trees,” Electromagnetic Compatibility Analysis Center, Building 120 North Severn Naval Station Annapolis, MD 21402, Tech. Rep., 1982.

[77] Ericsson, “Ericsson mobility report,” Ericsson, SE-164 80 Stockholm, Sweden, Tech. Rep. EAB-17:005964 Uen, Revision A, Jun. 2017. [Online]. Available: https://www.ericsson.com/assets/local/mobility-report/documents/2017/ericsson-mobility-report-june-2017.pdf.

[78] T. S. Rappaport, R. W. Heath Jr, R. C. Daniels, and J. N. Murdock, *Millimeter wave wireless communications*. Pearson Education, 2014.

[79] K. Okada, K. Kondou, M. Miyahara, M. Shinagawa, H. Asada, R. Minami, T. Yamaguchi, A. Musa, Y. Tsukui, Y. Asakura, S. Tamonoki, H. Yamagishi, Y. Hino, T. Sato, H. Sakaguchi, N. Shimasaki, T. Ito, Y. Takeuchi, N. Li, Q. Bu, R. Murakami, K. Bunsen, K. Matsushita, M. Noda, and A. Matsuzawa, “Full four-channel 6.3-Gb/s 60-GHz CMOS transceiver with low-power analog and digital baseband circuitry,” *IEEE Journal of Solid-State Circuits*, vol. 48, no. 1, pp. 46–65, Jan. 2013. DOI: 10.1109/jssc.2012.2218066.

[80] N. Saito, T. Tsukizawa, N. Shirakata, T. Morita, K. Tanaka, J. Sato, Y. Morishita, M. Kanemaru, R. Kitamura, T. Shima, T. Nakatani, K. Miyanaga, T. Urushihara, H. Yoshikawa, T. Sakamoto, H. Motozuka, Y. Shirakawa, N. Yosoku, A. Yamamoto, R. Shiozaki, and K. Takinami, “A fully integrated 60-GHz CMOS transceiver chipset based on WiGig/IEEE 802.11ad with built-in self calibration for mobile usage,” *IEEE Journal of Solid-State Circuits*, vol. 48, no. 12, pp. 3146–3159, Dec. 2013. DOI: 10.1109/jssc.2013.2279573.

[81] D. Fritsche, G. Tretter, C. Carta, and F. Ellinger, “Millimeter-wave low-noise amplifier design in 28-nm low-power digital CMOS,” *IEEE Transactions on Microwave Theory and Techniques*, vol. 63, no. 6, pp. 1910–1922, Jun. 2015. DOI: 10.1109/tmtt.2015.2427794.

[82] Z. Pi and F. Khan, “An introduction to millimeter-wave mobile broadband systems,” *IEEE Communications Magazine*, vol. 49, no. 6, pp. 101–107, Jun. 2011. DOI: 10.1109/mcom.2011.5783993.

[83] W. Roh, J.-Y. Seol, J. Park, B. Lee, J. Lee, Y. Kim, J. Cho, K. Cheun, and F. Aryanfar, "Millimeter-wave beamforming as an enabling technology for 5G cellular communications: Theoretical feasibility and prototype results," *IEEE Communications Magazine*, vol. 52, no. 2, pp. 106–113, Feb. 2014. DOI: 10.1109/mcom.2014.6736750.

[84] G. R. MacCartney and T. S. Rappaport, "73 GHz millimeter wave propagation measurements for outdoor urban mobile and backhaul communications in new york city," in *2014 IEEE International Conference on Communications (ICC)*, IEEE, IEEE, Jun. 2014, pp. 4862–4867. DOI: 10.1109/icc.2014.6884090.

[85] A. I. Sulyman, A. T. Nassar, M. K. Samimi, G. R. Maccartney, T. S. Rappaport, and A. Alsanie, "Radio propagation path loss models for 5G cellular networks in the 28 GHZ and 38 GHZ millimeter-wave bands," *IEEE Communications Magazine*, vol. 52, no. 9, pp. 78–86, Sep. 2014. DOI: 10.1109/mcom.2014.6894456.

[86] S. Deng, M. K. Samimi, and T. S. Rappaport, "28 GHz and 73 GHz millimeter-wave indoor propagation measurements and path loss models," in *2015 IEEE International Conference on Communication Workshop (ICCW)*, IEEE, IEEE, Jun. 2015, pp. 1244–1250. DOI: 10.1109/iccw.2015.7247348. eprint: 1509.00395.

[87] T. S. Rappaport *et al.*, *Wireless communications: principles and practice*. New Jersey: Prentice Hall PTR, 1996, vol. 2.

[88] C. D. Rowe, "Channel propagation model for train to vehicle alert system at 5.9 GHz using dedicated short range communication," PhD thesis, Blacksburg, VA, 2016. [Online]. Available: http://hdl.handle.net/10919/73178.

[89] H. Yilmaz, T. Tugcu, F. Alagöz, and S. Bayhan, "Radio environment map as enabler for practical cognitive radio networks," *IEEE Communications Magazine*, vol. 51, no. 12, pp. 162–169, Dec. 2013. DOI: 10.1109/mcom.2013.6685772.

[90] T. A. Thomas, H. C. Nguyen, G. R. MacCartney, and T. S. Rappaport, "3D mmWave channel model proposal," in *2014 IEEE 80th Vehicular Technology Conference (VTC 2014-Fall)*, IEEE, IEEE, Sep. 2014, pp. 1–6. DOI: 10.1109/vtcfall.2014.6965800.

[91] H. M. Rahim, C. Y. Leow, and T. A. Rahman, "Millimeter wave propagation through foliage: Comparison of models," in *2015 IEEE 12th Malaysia International Conference on Communications (MICC)*, IEEE, Nov. 2015, pp. 236–240. DOI: 10.1109/micc.2015.7725440.

[92] S. A. Busari, S. Mumtaz, S. Al-Rubaye, and J. Rodriguez, "5G millimeter-wave mobile broadband: Performance and challenges," *IEEE Communications Magazine*, vol. 56, no. 6, pp. 137–143, Jun. 2018, ISSN: 0163-6804. DOI: 10.1109/mcom.2018.1700878.

[93] H. Wu, L. Zhang, and Y. Miao, "The propagation characteristics of radio frequency signals for wireless sensor networks in large-scale farmland," *Wireless Personal Communications*, vol. 95, no. 4, pp. 3653–3670, Feb. 2017. DOI: 10.1007/s11277-017-4018-5.

[94] P. B. Papazian, D. L. Jones, and R. H. Espeland, "Wideband propagation measurements at 30.3 GHz through a pecan orchard in texas," National Telecommunications and Information Administration (NTIA), Boulder, CO, Tech. Rep. 92-287, Sep. 1992.

[95] T. S. Rappaport and S. Deng, "73 GHz wideband millimeter-wave foliage and ground reflection measurements and models," in *2015 IEEE International Conference on Communication Workshop (ICCW)*, IEEE, IEEE, Jun. 2015, pp. 1238–1243. DOI: 10.1109/iccw.2015.7247347.

[96] M. Shaik, A. Kabanni, and N. Nazeema, "Millimeter wave propagation measurments in forest for 5G wireless sensor communications," in *2016 16th Mediterranean Microwave Symposium (MMS)*, IEEE, IEEE, Nov. 2016, pp. 1–4. DOI: 10.1109/mms.2016.7803785.

[97] Y. Zhang, T. Arakawa, J. V. Krogmeier, C. R. Anderson, D. J. Love, and D. R. Buckmaster, "Large-scale cellular coverage analyses for UAV data relay via channel modeling," in *ICC 2020 - 2020 IEEE International Conference on Communications (ICC)*, IEEE, Jun. 2020, pp. 1–6. DOI: 10.1109/icc40277.2020.9149403.

[98] S. Sekander, H. Tabassum, and E. Hossain, "Multi-tier drone architecture for 5G/B5G cellular networks: Challenges, trends, and prospects," *IEEE Communications Magazine*, vol. 56, no. 3, pp. 96–103, Mar. 2018. DOI: 10.1109/mcom.2018.1700666.

[99] B. Rao, A. G. Gopi, and R. Maione, "The societal impact of commercial drones," *Technology in Society*, vol. 45, pp. 83–90, May 2016, doi: 10.1016/j.techsoc.2016.02.009, ISSN: 0160-791X. DOI: 10.1016/j.techsoc.2016.02.009.

[100] D. Zorbas, T. Razafindralambo, D. P. P. Luigi, and F. Guerriero, "Energy efficient mobile target tracking using flying drones," *Procedia Computer Science*, vol. 19, pp. 80–87, 2013, doi: 10.1016/j.procs.2013.06.016, ISSN: 1877-0509. DOI: 10.1016/j.procs.2013.06.016.

[101] M. Mozaffari, W. Saad, M. Bennis, Y.-H. Nam, and M. Debbah, "A tutorial on UAVs for wireless networks: Applications, challenges, and open problems," *IEEE Communications Surveys Tutorials*, vol. 21, no. 3, pp. 2334–2360, 2019. DOI: 10.1109/comst.2019.2902862.

[102] N. H. Motlagh, T. Taleb, and O. Arouk, "Low-altitude unmanned aerial vehicles-based internet of things services: Comprehensive survey and future perspectives," *IEEE Internet of Things Journal*, vol. 3, no. 6, pp. 899–922, Dec. 2016. DOI: 10.1109/jiot.2016.2612119.

[103] H. Menouar, I. Guvenc, K. Akkaya, A. S. Uluagac, A. Kadri, and A. Tuncer, "UAV-enabled intelligent transportation systems for the smart city: Applications and challenges," *IEEE Communications Magazine*, vol. 55, no. 3, pp. 22–28, Mar. 2017. DOI: 10.1109/mcom.2017.1600238cm.

[104] D. Murugan, A. Garg, and D. Singh, "Development of an adaptive approach for precision agriculture monitoring with drone and satellite data," *IEEE Journal of Selected Topics in Applied Earth Observations and Remote Sensing*, vol. 10, no. 12, pp. 5322–5328, Dec. 2017. DOI: 10.1109/jstars.2017.2746185.

[105] M. Mozaffari, W. Saad, M. Bennis, and M. Debbah, "Efficient deployment of multiple unmanned aerial vehicles for optimal wireless coverage," *IEEE Communications Letters*, vol. 20, no. 8, pp. 1647–1650, Aug. 2016. DOI: 10.1109/lcomm.2016.2578312.

[106] Y. Chen, W. Feng, and G. Zheng, "Optimum placement of UAV as relays," *IEEE Communications Letters*, vol. 22, no. 2, pp. 248–251, Feb. 2018. DOI: 10.1109/lcomm.2017.2776215.

[107] S. Zhang, Y. Zeng, and R. Zhang, "Cellular-enabled UAV communication: Trajectory optimization under connectivity constraint," in *2018 IEEE International Conference on Communications (ICC)*, IEEE, May 2018, pp. 1–6. DOI: 10.1109/icc.2018.8422584.

[108] The Wabash Heartland Innovation Network consortium. About WHIN. Accessed: Oct. 28, 2019, [Online]. Available: https://whin.org/about/.

[109] OpenTopography, *2011 - 2013 Indiana statewide LiDAR*, Oct. 2012. DOI: 10.5069/G9959FHZ.

[110] J. Joo, D. S. Han, and H.-J. Jeong, "First Fresnel zone analysis in vehicle-to-vehicle communications," in *2015 International Conference on Connected Vehicles and Expo (ICCVE)*, IEEE, Oct. 2015. DOI: 10.1109/iccve.2015.18.

[111] D. D. Coleman and D. A. Westcott, *CWNA: certified wireless network administrator official study guide: exam PW0-105*. John Wiley & Sons, 2012.

[112] National Telecommunications and Information Administration. The extended Hata (eHata) urban propagation model. Accessed: Oct. 24, 2019, [Online]. Available: https://github.com/NTIA/ehata.git.

[113] E. F. Drocella, J. Richards, R. Sole, F. Najmy, A. Lundy, and P. McKenna, *3.5 GHz exclusion zone analyses and methodology*. US Department of Commerce, National Telecommunications and Information Administration, 2016.

[114] National Telecommunications and Information Administration. LTE (FDD) transmitter characteristics. Accessed: Oct. 24, 2019, [Online]. Available: https://www.ntia.doc.gov/files/ntia/meetings/lte_technical_characteristics.pdf.

[115] J. Jung, *2016 - 2020 Indiana statewide LiDAR*, 2020. [Online]. Available: https://lidar.jinha.org/.

[116] GeoPlatform ArcGIS Online, *Cellular towers*, Apr. 2020. [Online]. Available: https://hifld-geoplatform.opendata.arcgis.com/datasets/geoplatform::cellular-towers/.

VITA

Yaguang Zhang received the M.Sc. degree in Electrical and Computer Engineering from Purdue University, USA, in 2015, and the B.Eng. degree in Communication Engineering from Tianjin University, China, in 2013. He is currently pursuing a Ph.D. degree in electrical and computer engineering at Purdue University, West Lafayette, IN, USA. His research interests lie in the areas of UAV-aided wireless communication systems, 5G millimeter-wave channel measurement and modeling, intelligent transportation system applications in digital agriculture, and engineering education.